Tuning surface stoichiometry and morphology by atmospheric pressure plasma jet generated reactive oxygen species and short pulsed laser irradiation

Dissertation

zur Erlangung des Grades
"eines Doktors der Naturwissenschaften"

an der Fakultät für Physik und Astronomie
der Ruhr-Universität Bochum

von

Sascha Frederik Chur

aus Hattingen

Bochum 2025

1. Gutachter: Prof. Judith Golda

2. Gutachter: Prof. Achim von Keudell

Datum der Disputation: ____________________

This thesis was supported by the German Research Foundation (DFG) as part of the Collaborative Research Center (CRC) 1316, "Transient Atmospheric Plasmas: From Plasmas to Liquids to Solids", within subproject B2, "Self-organisation of sub-μm surface structures stimulated by microplasma generated reactive species and short-pulsed laser irradiation".

Contents

1 Introduction

Catalysts play a central role in the modern chemical industry, enhancing reaction rates, selectivity, and energy efficiency. They enable more sustainable processes by reducing energy demands and minimizing waste production [1]. Traditionally, catalytic reactions occur at high temperatures and pressures, but with the transition to renewable energy sources, there is an increasing interest in milder conditions and more specialized catalysts. This drives the need for a deeper understanding of catalytic mechanisms and the development of novel synthesis techniques.

Plasma-assisted catalyst synthesis is a promising alternative to conventional catalyst synthesis. Plasmas enable rapid material processing with controlled properties and can synthesize otherwise challenging-to-form compounds, such as carbons, nitrides, and fluorides. According to A. Bogaerts *et al.* [2], plasma applications in catalysis include: (1) synthesis of ultrafine catalyst particles, (2) plasma-assisted deposition of active phases, and (3) plasma-enhanced catalyst preparation and treatment. Key advantages include reduced energy input, precise control over material properties, generation of highly reactive species, short processing times, and enhanced catalytic performance in terms of selectivity, activation, stability, and regeneration.

A highly relevant is the electrochemical CO_2 reduction reaction (CO_2-RR), which offers a pathway to convert CO_2 into value-added products and close the carbon cycle [3–5]. Due to CO_2's chemical stability, effective catalysts are essential, ideally operable under mild conditions powered by renewables [6]. Copper (Cu) is a promising candidate, as it is abundant, cost-effective, and the only known metal to yield significant amounts of C_{2+} products like ethylene and ethanol [7–9]. However, Cu suffers from limited selectivity and stability under CO_2-RR conditions [10, 11].

Micro atmospheric pressure plasma jets (µ-APPJs) [12–17] are known to produce various reactive oxygen species and offer multiple advantages: they operate without vacuum systems, are suitable for temperature- and vacuum-sensitive materials, and allow direct application of reactive effluents to various substrates. Their effectiveness stems from their non-equilibrium discharges, where electrons are selectively heated, while ions and neutrals remain comparatively cool.

µ-APPJs generate reactive species primarily through electron impact dissociation [18], especially when reactive gases like N_2 [19, 20] or O_2 [21–23] are introduced. Plasma chemistry is complex, involving excitation, ionization, dissociation, and quenching mechanisms. The "COST Reference Microplasma Jet" [24] provides a well-characterized reference source and has been benchmarked in simulations with reasonable accuracy [25–27], though further species validation is needed to deepen mechanistic understanding. This necessitates measurements of reactive species densities. Due to the complexity of the plasma chemistry and the difficulty in experimentally measuring many species densities, especially temporally or spatially resolved, modeling plays a key role.

Plasmas can generate reactive species such as atomic oxygen, which oxidize copper surfaces and promote the formation of Cu(II) species [28]. Additionally, plasma activation has been shown to enhance catalytic performance in CO_2-RR [29–31]. Therefore, studying the behavior and influence of reactive oxygen species is key to tuning catalyst surface chemistry for improved catalytic performance.

Gusakov *et al.* [28] showed that the oxidation of copper, especially higher oxidative states like CuO, is influenced by the presence of both atomic and molecular oxygen [28]. While atomic oxygen is the main reactant, it also triggers back-reactions at high concentrations, limiting CuO formation. However, Gusakov *et al.* identified the presence of molecular oxygen as essential to quench these back reactions. Molecular oxygen's ground state is too inert, though. Instead, electronically excited states, like $O_2(a^1\Delta_g)$ and $O_2(b^1\Sigma_g^+)$, are likely responsible. Their densities are closely linked to ozone density due to its strong quenching. $O_2(b^1\Sigma_g^+)$ can be detected in the plasma region via emission spectroscopy [32], whereas $O_2(a^1\Delta_g)$ is more difficult to measure, due to its weak emission at 1270 nm [33]. Its detection is further hindered by the high thermal background in the plasma zone. Consequently, measurements are typically performed in the effluent, using gas flow cells to enhance the signal [34, 35].

Copper oxides, especially Cu_2O (Cu(I)) and CuO (Cu(II)), have demonstrated improved selectivity and durability [36–40]. These oxides differ structurally and electronically, influencing their interaction with CO_2 and intermediates. CuO, in particular, shows promising selectivity towards ethylene [4, 41], with some studies reporting over 50% C_{2+} selectivity [42, 43]. Thus, understanding and controlling surface composition is crucial for optimizing catalyst performance.

Another approach to enhance catalytic performance is surface structuring, particularly through the use of nano-scale structures, which can improve selectivity and boost the formation of C_{2+} products [44–46]. Techniques such as laser-induced periodic surface structures (LIPSS) [47] and pulsed laser-induced dewetting (PLID) [48] are effective in creating such structures. Within this study, PLID and PLIDS are both used abbreviations. PLID refers to the formation mechanism, while PLIDS (pulsed laser-induced dewetting structures) describe the resulting nanoparticles.

PLID leverages capillary-driven reorganization of molten metal films to form nanoparticles, minimizing surface-to-volume ratio [48, 49]. Despite its simplicity in terms of input parameters, PLID enables the reliable formation of intricate nanoscale patterns [50, 51]. The PLID formation requires composite materials that feature a thin metal layer on a typically silicon substrate, for example, deposited by magnetron sputtering. This results in defined surface conditions for the fabricated samples, which lend themselves well to surface characterization. However, their application is often limited under real-world conditions, and their production is often costly. An aim of the study is, therefore, to investigate the transition to bulk materials such as simple copper foils, as they find widespread use in industry.

To structure bulk materials, LIPSS [47] have to be used. LIPSS leverage the self-enhancing energy absorption of a rough surface by the interference of the incoming laser light with their refracted waves on the surface. This ultimately leads to periodically modulated surface structures in the range of the laser wavelength. Nano-scale structures have shown potential to enhance catalytic activity [6, 52]. When combining laser and plasma treatment, however, the effects of the laser on surface oxidation and chemical composition remain unclear, and vice versa.

The final goal of this study is to investigate a new approach to catalyst fabrication. By combining the reactive species produced by a micro-scaled atmospheric plasma jet and the irradiation and energy input of a pulsed laser on copper surfaces, the chemical composition and surface morphology can be controlled independently. This approach has not been thoroughly investigated before. The “COST Reference Microplasma Jet” [53] is employed as a well understood plasma source. It therefore lends itself very well to the investigation of the reactive oxygen species.

There were already multiple studies [54, 55] centered around atomic oxygen, leading to a good understanding of its production and destruction mechanisms, as well as densities in and outside the plasma. However, excited molecular oxygen species densities are not known or benchmarked against current models. This study will therefore focus on these reactive species to investigate their impact on the proposed reactions by Gusakov *et al.*.

Moreover, the interaction between laser and plasma exposure on surface morphology and composition has not yet been investigated, particularly for simultaneous application. The combined use of plasma treatment and laser irradiation may offer a synergistic and more tunable strategy for catalytic surface functionalization, potentially surpassing conventional methods. To optimize the process, it is critical to investigate laser parameters such as pulse energy and power, as well as the reactive species flux to the treated sample.

These investigations are made on copper samples to study the oxide formation and surface structuring under the combined treatment. Copper thin films offer reliable surface conditions for analysis. However, to test the transferability to more industrially applicable materials, a transition of the findings to bulk materials is investigated.

1.1 Research Questions

The following questions provide a guideline for the successful synthesis of a copper-based CO_2-RR catalyst material using a combined treatment of a laser for surface structuring and a plasma for changing the surface stoichiometry:

1. Does the COST jet produce reactive molecular oxygen species in sufficient densities to facilitate the formation process of Cu(II) copper oxides as proposed by Gusakov *et al.*?

2. What are the reaction dynamics of the different species inside the jet and its effluent, and how are they transported to the surface? What is the flux that reaches a sample?

3. What are the optimal plasma parameters?

4. Which laser parameters are able to successfully induce nanoscale surface structures on copper, and which structures can be utilized best for specific applications?

5. What influence does the simultaneous plasma treatment have on the formation of laser-induced surface structures?

6. Do the laser-induced structures influence the chemical composition of the surface?

7. Which copper oxides can be produced by the combined laser and plasma treatment, and can their concentration be controlled?

8. Can the findings be transferred to bulk materials?

1.2 Thesis Outline

The study is structured in four parts. Following the Introduction, the Fundamentals outline the basic physics. Provided is an overview of non-equilibrium atmospheric plasma jets, and optical spectroscopy methods for their analysis. Regarding the available species, likely candidates for the formation of copper oxides are discussed. Of special interest are the generation and destruction reactions of atomic oxygen, as well as the physical properties of the molecular excited states $O_2(a^1\Delta_g)$ and $O_2(b^1\Sigma_g^+)$.

After that, the fundamentals of laser systems are provided. They introduce the concept of transverse modes, which are necessary to describe the beam shape and quality, as well as the difference in surface interaction between laser pulses of varying lengths. Following that, a mathematical description of the most commonly induced laser surface structures, LIPSS and PLIDS is given. Lastly, for the Fundamentals chapter, the two employed surface analysis techniques, SEM and XPS, are explained.

After the Fundamentals, the experimental setups are introduced. First, the spectroscopy setup for investigating the reactive plasma species is covered. Here, the setup for the absorption spectroscopy of ozone and the emission spectroscopy of $O_2(a^1\Delta_g)$ and $O_2(b^1\Sigma_g^+)$ are explained. Next, the surface modification setup is described, which combines plasma jet and laser irradiation on copper samples to induce morphological and stoichiometric changes. Lastly, the critical components of the XPS device are covered.

The Results chapter begins with the investigation of reactive oxygen species. Here, the experimental data will be compared to two simulations to validate the absolute species densities. As ozone is required for calculating the $O_2(a^1\Delta_g)$ density, its density is investigated first in terms of power, flux, and admixture variation. The same variation measurements are then performed for $O_2(a^1\Delta_g)$ and $O_2(b^1\Sigma_g^+)$ as they are important for the formation of copper oxides. In the summary section, knowledge about the optimal plasma parameters will be utilized to optimize the laser-plasma setup.

The ns-laser surface structuring chapter provides an overview of the different laser-induced surface structures on copper thin films and foils. Laser energy and irradiation time are varied to determine successful laser parameters for surface structuring, as observed using SEM images. Furthermore, the influence of the gas flow on their formation is studied. The optimal laser parameters are then utilized in the combined laser-plasma treatment.

The previously studied plasma and laser parameters culminate in the chemical surface analysis section, which investigates whether the described setup can achieve the initial assumption of a controlled stoichiometry. Firstly, the XPS analysis method is described, which is used to measure the concentration of the copper oxides. The initial surface composition is then compared with a laser-irradiated sample and with samples after 5-10 s of laser-plasma treatment to determine which copper oxides are generated and quantify their concentration.

The fs-laser structuring section investigates morphology and stoichiometric changes on bulk materials, rather than thin films, using a fs-laser. It repeats the laser parameter investigation for successful surface structuring as performed for the ns-laser. Likewise, the stoichiometry changes are investigated using XPS in regard to the copper oxide concentration for untreated, laser-irradiated, and laser-plasma treated samples.

The Conclusion and Outlook chapter answers the research questions, using the collected insights of the conducted studies. Additionally, it gives an overview of measurements that could be performed in the future to elaborate on or optimize the performed measurements. Furthermore, it provides a look into further application cases for the laser-plasma process.

2 Fundamentals

This chapter provides a brief introduction to the key theories underlying the employed diagnostics and experimental setups. As plasmas play a central role within the analysis and application of this study, their basics are covered first:

2.1 Non-equilibrium Atmospheric Pressure Plasmas

Low temperature plasmas garnered considerable interest due to their wide-ranging applications, including surface treatment [56, 57], etching [58], and deposition [17, 59]. The properties and ignition mechanisms of plasmas strongly depend on the pressure under which they operate. The operating pressure is therefore a useful tool for categorization. Plasmas are distinguished between low-pressure, atmospheric-pressure, and high-pressure. Applications for low-pressure plasmas include plasma etching and the deposition of thin films on metals or plastics [60]. Natural low-pressure plasmas include auroras and the Earth's ionosphere. High-pressure plasmas are, for example, used in gas discharge lamps.

For technical applications, atmospheric pressure plasmas are particularly attractive, as they do not require complex vacuum systems and can be brought directly into contact with substrates via the effluent. These plasmas can be further divided into two subclasses. Thermal plasmas are, for example, used in plasma welding [61], while non-thermal plasmas are employed to treat heat-sensitive substrates such as plastics [62], for example. This also makes them particularly attractive for applications in medicine by treating organic materials [63, 64].

A plasma is commonly defined as a quasineutral gas of charged and neutral particles that exhibits collective behavior. It is generated when sufficient energy is deposited into a neutral gas to cause ionization, producing free electrons and ions. Collective behavior describes the interdependency of electron and ion movement, as both particles are connected due to Coulomb forces. Not all ionized gases qualify as plasmas, though.

Plasmas are considered quasineutral because, on macroscopic scales, the electron and ion densities are nearly equal ($n_e \approx n_i$), resulting in an overall neutral charge distribution. On smaller scales, however, this neutrality can be locally violated due to charge separation effects. The spatial length scale over which electrostatic potentials are shielded is described by the Debye length λ_D,

$$\lambda_D = \left(\frac{\varepsilon_0 k_B T_e}{n_e e^2}\right)^{1/2}, \tag{2.1}$$

where ε_0 is the vacuum permittivity, k_B the Boltzmann constant, T_e the electron temperature, n_e the electron density, and e the elementary charge. For a plasma to exist its characteristic dimensions L must be much larger than λ_D,

$$L \gg \lambda_D. \tag{2.2}$$

In addition, the number of charged particles within a Debye sphere N_D must be sufficiently large to ensure that collective effects dominate over binary collisions. This number is given by

$$N_D = \frac{4}{3}\pi\lambda_D^3 n_e \gg 1. \tag{2.3}$$

The collective behavior of a plasma is expressed through its ability to sustain plasma oscillations. When electrons are displaced relative to the heavier ions, Coulomb forces act to restore quasineutrality, resulting in oscillatory motion characterized by the plasma frequency ω_p

$$\omega_p = \left(\frac{n_e e^2}{\varepsilon_0 m_e}\right)^{1/2}, \tag{2.4}$$

where m_e is the electron mass. A corresponding ion plasma frequency $\omega_{p,i}$ exists but is much lower due to the higher ion mass. The plasma frequency determines the response of charged particles to external electromagnetic fields. Electrons, due to their lower mass, can respond to higher frequencies than ions.

For collective plasma effects to dominate over neutral gas dynamics, the product of plasma frequency ω_p and the mean time between particle collisions τ must satisfy:

$$\omega_p \tau \gg 1. \tag{2.5}$$

This condition is typically fulfilled in low-pressure plasmas, where collisions are rare and long-range Coulomb interactions govern particle behavior. In atmospheric-pressure plasmas, however, the collision frequency is considerably higher, and their dynamics are strongly collisional. Consequently, atmospheric plasmas are often described as collisional discharges rather than ideal plasmas [65].

Non-equilibrium plasmas exhibit a disparity between the electron temperature T_e and the gas temperature T_g ($T_e \gg T_g$). This allows the generation of chemically active species and efficient excitation or ionization processes without heating the bulk gas.

In non-equilibrium plasmas, energy is primarily coupled into the electrons through an external electric field. Due to their low mass, the electrons are rapidly accelerated and can reach energies corresponding to several electronvolts, while the heavy particles remain close to ambient temperature due to their much slower energy exchange rates. The energy distribution of electrons can be described by the electron energy distribution function (EEDF), often deviating from a Maxwellian form in these non-equilibrium conditions. The mean electron energy $\langle \varepsilon \rangle$ is related to the electron temperature by:

$$\langle \varepsilon \rangle = \frac{3}{2} k_B T_e. \tag{2.6}$$

For non-equilibrium atmospheric pressure plasmas, $\omega_p \tau$ often approaches or falls below unity, indicating that collisions play a crucial role in determining particle dynamics, energy transfer, and chemical reactivity. The reduced electric field E/N (electric field strength E normalized to the neutral number density N) is an important control parameter, influencing ionization, excitation, and dissociation rates in the plasma chemistry.

For helium plasmas at atmospheric pressure like the one employed in this study, typical parameters are an electron density of $n_e \approx 10^{11}$ cm^{-3} [66], an electron temperature of $T_e \approx 2$ eV [24, 67], a Debye length of $\lambda_D \approx 100$ μm, and an electron plasma frequency of $\omega_{p,e} \approx 7 \cdot 10^7$ Hz.

2.1.1 Plasma Ignition

Plasma ignition occurs when electron production exceeds losses from collisions and recombination. At the breakdown voltage, free electrons gain sufficient energy between collisions to ionize neutral gas atoms, initiating an electron avalanche described by Townsend breakdown theory. The first Townsend coefficient α characterizes electron multiplication along the applied electric field lines. For a given neutral gas density n_0, the electron density can be calculated:

$$n_e(x) = n_0 \exp\left(\alpha x\right). \tag{2.7}$$

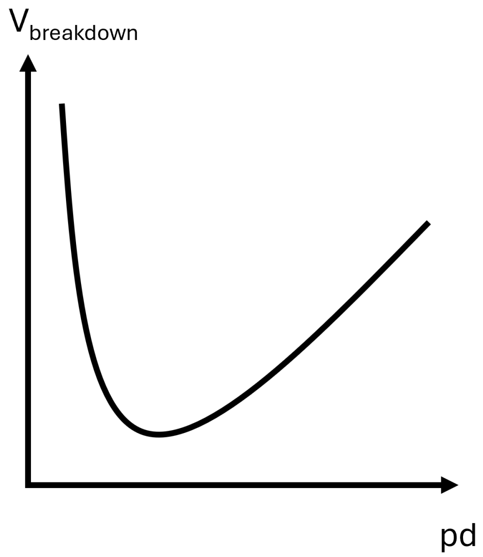

Figure 2.1: Example Paschen curve showing the breakdown voltage as a function of the product $p \cdot d$, where p is the gas pressure and d the electrode spacing.

The breakdown voltage depends on the gas type, pressure p, and electrode distance d. According to Paschen's law, V_{br} varies with the product $p \cdot d$, exhibiting a minimum (see Fig. 2.1). At low $p \cdot d$, electrons only rarely collide with neutrals before reaching an electrode, reducing ionization probability. At high $p \cdot d$, frequent collisions prevent electrons from gaining sufficient kinetic energy for ionization in between collisions. Therefore, both regimes require higher breakdown voltages.

At atmospheric pressure, p is fixed; thus, only d can be adjusted. For a helium discharge at 1 bar, the minimum breakdown voltage is achieved with electrode gaps of several hundred micrometers to a few millimeters. Consequently, atmospheric-pressure plasmas are often referred to as microplasmas [68]. Atmospheric pressure plasmas are also often ignited using RF-frequency.

In case of a radio-frequency (RF) excitation of the plasma, the ignition is no longer dependent on the DC current of electrons reaching the electrodes, but on the displacement current. When considering an alternating electric field, the time-averaged dissipated power is given by:

$$\langle P \rangle_t = \frac{ne^2 E_0^2}{2m(\omega^2 + \nu_m^2)} \tag{2.8}$$

with the E_0 electric field amplitude, ω the frequency of the electric field and ν_m the elastic collision frequency. The electrons accumulate energy by being displaced out of phase with the electric field E through collisions.

To calculate the discharge ignition requirements, an energy balance is considered:

$$\frac{ne^2 \nu_m E_0^2}{2m_e(\omega^2 + \nu_m^2)} = n\nu_{\mathrm{ion}} E_{\mathrm{ion}} + \frac{m_e}{m_g} n\nu_m \langle E \rangle + n\langle E \rangle \frac{1}{\tau_{\mathrm{diff}}} \tag{2.9}$$

The energy gain of a system is the dissipated ohmic current given by the left side of the equation. The energy loss is given by the right side, which consists of the ionization rate ν_{ion} and energy E_{ion}, the energy loss from elastic collisions ν_m, and the loss of particles through diffusion given by the confinement time τ_{diff} with the average energy of $\langle E \rangle$.

The ignition requirement can then be derived from the balancing of charged particle production and their losses due to diffusion to:

$$\nu_{\text{ion}} = \frac{1}{\tau_{\text{diff}}} \tag{2.10}$$

For the case of atmospheric pressure ($\nu_m \gg \omega$), the pressure is high enough for most particles to reach an average energy $\langle E \rangle$ close to the ionization energy E_{ion}, because of the low diffusion losses. The ignition electric field strength results to:

$$E_0 = \left[\frac{m_e^2}{m_g e^2} E_{\text{ion}} (\nu_m^2 + \omega^2) \right] \tag{2.11}$$

With ($\nu_m \gg \omega$), it is obvious that the ignition requirement is only dependent on the density $\nu_m = n_g \langle v \sigma_m \rangle$ and, in particular, independent from the reactor geometry.

This simplified model, however, disregards secondary electron emission (SEE), which is another production mechanism for electrons. This results in a modified Paschen curve as shown in Fig. 2.2.

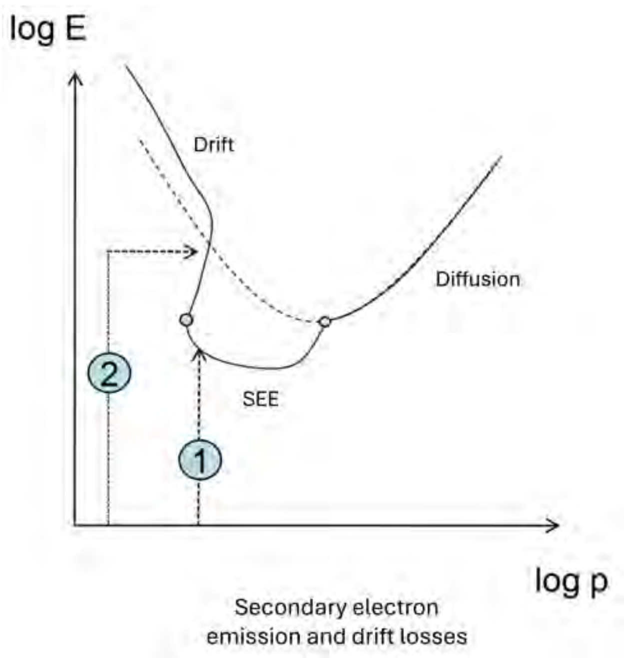

Figure 2.2: Example Paschen curve showing the breakdown voltage as a function of the pressure p including SEE effects (taken from [69]).

At low pressure and for certain frequency ranges, the oscillation amplitude of the electron motion can approach the electrode spacing. Under these conditions, charge carrier losses substantially increase, which in turn leads to an increase in the breakdown field strength. The transition to this regime is not gradual but occurs abruptly once the oscillation amplitude exceeds a critical value at a given frequency.

At high frequencies, the breakdown field strength remains nearly constant. As the frequency decreases, the oscillation amplitude increases, and a fraction of the electrons begins to reach the electrodes, giving rise to slightly enhanced losses. This results in a modest increase in the breakdown field. Once the amplitude matches the electrode gap, however, the losses rise sharply, necessitating a pronounced increase in the breakdown field to sustain the discharge.

With further reduction of the frequency, the energy of particles impacting the electrodes increases, thereby enhancing the efficiency of secondary electron emission. This process introduces an additional electron source, which partially offsets the loss mechanisms and lowers the breakdown field once again.

If the frequency and electrode spacing are favorable, these secondary processes can amplify through feedback, leading to multipactor discharges. Such discharges are of particular relevance as parasitic effects in evacuated waveguides used for microwave transmission in large-scale fusion devices.

Traditional models assume ignition occurs solely through externally applied fields accelerating carriers, which leave the field unaffected by the plasma itself. At higher pressures, however, electron avalanches can locally modify the field to the point that they independently trigger ignition. This process is called streamer mechanism.

Ignition at atmospheric pressure commonly proceeds via a streamer mechanism. A strong electric field initiates an avalanche that amplifies the local space charge, generating a field comparable to the external one. This self-enhanced field enables streamer propagation, forming a quasi-neutral conductive channel. Once the streamer bridges the electrodes, a short circuit forms, and a backward ionization wave propagates through the channel. High currents can flow, potentially transitioning the discharge into an arc (thermal plasma) [70, 71].

For non-thermal plasmas, avoiding arc formation is essential due to the associated heat and electrode damage. This can be accomplished by several methods. One method is to prevent the streamer from contacting the opposing electrode by using dielectric layers, thereby extinguishing the discharge before an arc develops. Other methods are shaping inhomogeneous fields that inhibit full bridging, as in corona discharges, limiting the discharge current, or employing an alternating current operation that extinguishes the plasma before an arc is formed.

2.1.2 Atmospheric Pressure Plasma Jets

This is the approach employed by APPJs, which utilize high AC frequency in the RF-region, keeping the neutral gas and ion temperatures low. This can be explained by considering the plasma frequency of electrons and ions, which describes the oscillation frequency of a charge carrier displaced from its equilibrium position in the plasma.

$$\omega_{p_{e,i}} = \sqrt{\frac{n_{e,i}e^2}{\epsilon_0 m_{e,i}}} \tag{2.12}$$

Here, n represents the charge carrier density, e the elementary charge, ϵ_0 the permittivity of free space, and m the mass. To calculate the plasma frequencies, a typical charge carrier density of 10^{17} m^{-3} was assumed. For electrons, this results in a plasma frequency of $\omega_e =$ 6 GHz, while for ions, it is $\omega_p = 70$ MHz. Comparing the two plasma frequencies $\omega_{p_{e,i}}$ of electrons (e) and ions (i) with an RF voltage frequency clarifies that ions cannot or can only barely follow the rapid RF oscillations. Thus, only the electrons are energized.

The large mass difference between electrons and ions, as well as neutral gas particles, further prevents the electrons from transferring their thermal energy to the heavier particles by collisions. This creates a non-equilibrium plasma in which electrons, on average, attain an energy of approximately 2.5 eV [72], corresponding to a temperature of about 29 000 K. In contrast, the ions and the neutral gas remain cold, at approximately room temperature [53, 67]. This makes plasma jets particularly suitable for treating heat-sensitive substrates, such as plastics and organic tissues, including skin.

Following Paschen's law, which states that the breakdown voltage of a plasma depends on the pressure and the electrode spacing [73, 74], it is advantageous for atmospheric-pressure plasma jets to keep their dimensions small, within the mm- or μm-range, to achieve a low breakdown voltage that is technically easier to implement. Therefore, the name μ-APPJs is often used.

The plasma source used in this experiment is a capacitively coupled microplasma jet known as the "COST Reference Microplasma Jet". It is a so-called cross-field jet. Cross-field refers to the electrode arrangement, where the applied electric field is oriented perpendicular to the direction of the gas flow [53]. The perpendicular alignment of the electric field and gas flow decouples the discharge generation from the convective transport of reactive species. This allows for efficient electron heating and ionization within the confined discharge region while minimizing the afterglow density and the thermal impact on the effluent. In the context of plasma jets, the effluent refers to a directed gas flow outside the jet containing various reactive species generated in the plasma. Furthermore, the orthogonal field-flow arrangement contributes to a well-defined discharge structure, making cross-field APPJs attractive for both fundamental studies and standardized plasma–surface interaction experiments. The resulting species mix can be directed onto substrates for applications such as surface modification, thin-film deposition, or biomedical treatments [12, 13, 16, 17].

2.2 Plasma Spectroscopy

Determining plasma parameters at atmospheric pressure is challenging because conventional diagnostic methods, such as probe insertion, are unsuitable due to the small spatial dimensions and possible disturbances they induce in the discharge. Optical spectroscopy methods enable non-intrusive diagnostics, making them a preferred technique for microplasmas. Their experimental implementation is relatively straightforward, yet it still provides valuable insights into plasma properties.

2.2.1 Optical Emission Spectroscopy

Optical emission spectroscopy (OES) measures the spectral emission of excited species within the plasma. Each emission line results from a radiative transition between an excited energy state and a lower energy level, with the emitted photon carrying the corresponding energy difference ΔE. The wavelength associated with each transition identifies the emitting species [75]. Analysis of the line intensities and their relative ratios provides information about excitation temperatures, excited-state populations, and species densities. However, as OES detects only excited states, additional modeling is required to infer ground-state densities. Further complexity in the analysis arises through the line-of-sight integration of the technique. For spatially inhomogeneous plasma volumes, further models such as Abel-inversion have to be used to accurately describe spatially resolved densities.

The statistical nature of energy level transitions is characterized by the lifetime τ of an excited state i, which describes the time after which the number of excited particles decreases to $\frac{1}{e}$ of its initial population. The lifetime is related to the Einstein coefficients A_{ik} describing spontaneous emission probabilities:

$$\tau_{i,\mathrm{nat}} = \left(\sum_k A_{ik} \right)^{-1}, \tag{2.13}$$

where i is the excited state and k the lower energy state to which the atom relaxes to. The radiated power P_{Photo} associated with an emission line is then:

$$P_{\mathrm{Photo}} = A_{ik} \cdot h\nu \cdot N_i, \tag{2.14}$$

where $h\nu$ is the photon energy and N_i is the excited-state population density. In addition to a radiative decay, excited states may undergo non-radiative de-excitation due to collisions with surrounding atoms, molecules, or electrons, processes collectively referred to as quenching [75]. Accurate determination of excited species densities from OES measurements requires accounting for these quenching effects.

Molecular spectra are broader than atomic spectra because molecules exhibit a greater variety of excitation modes, including rotational, vibrational, and electronic transitions. The resulting spectra consist of many energy level transitions, leading to broader spectral distributions [76]. Even simple homonuclear molecules, such as O_2, possess vibrational and rotational modes, though their spectra are less complex than those of larger polyatomic species. In complex molecules, overlapping transitions and chemical reaction pathways further complicate spectral analysis [75].

Quenching also affects the lifetime of excited molecular species. Their effective fluorescence time τ_g, the time of their fluorescence to reach $1/e$ of its initial intensity, is determined by both radiative decay and non-radiative relaxation:

$$\frac{1}{\tau_g} = \frac{1}{\tau_f} + \frac{1}{\tau_q}, \tag{2.15}$$

where τ_f is the intrinsic fluorescence lifetime and τ_q represents the non-radiative relaxation time. The Einstein coefficient for spontaneous emission is given by $A_{ik} = 1/\tau_f$. The photon yield Q, describing the ratio of radiative to total de-excitation processes, is then:

$$Q = \frac{\tau_g}{\tau_f}. \tag{2.16}$$

This can be expressed in terms of the quenching rate $q = 1/\tau_q$:

$$Q = \frac{A_{ik}}{A_{ik} + q}, \tag{2.17}$$

where $q = \sum_i k_i n_i$ is the sum over all collisional quenching contributions, with k_i denoting quenching rate coefficients and n_i the densities of the quenching species. By applying these relations, quenched excited-state densities can be extracted from emission spectra when the relevant rate constants, transitions, and densities are known.

2.2.2 Optical Absorption Spectroscopy

Another optical method for plasma analysis is absorption spectroscopy. Here, a light source of a specific wavelength is chosen that aligns with the excitation energy of an observed species. The light is then absorbed by the species, leading to a decrease in the measured intensity. The absorbance of the species depends on its density n, the absorption length d, and its absorption coefficient k. It can be calculated by the Lambert-Beer law under the assumption of an idealized gas:

$$\log\left(\frac{I_T}{I_0}\right) = -k \cdot n \frac{p}{k_B T} \cdot d \tag{2.18}$$

where p is the pressure, T the temperature, I_0 is the initial intensity and I_T is the transmitted intensity. The density of a species is then given by:

$$n = \frac{p}{k_B T} \cdot \frac{\log\left(\frac{I_T}{I_0}\right)}{k \cdot d} \tag{2.19}$$

Absorption spectroscopy provides access to the ground-state density as it actively excites the state of interest. However, as for OES, absorption spectroscopy suffers from line-of-sight integration, making its analysis especially challenging for spatially inhomogeneous plasma volumes.

2.3 Reactive Species

Multiple reactive species can be produced by atmospheric pressure plasma jets, making the plasma chemistry rather complex, even with simple admixtures of, for example, just helium and oxygen. Although atomic oxygen plays a crucial role in the oxidation of copper, it is not addressed in the results presented here. There have already been multiple studies for the COST jet [54, 55] centered around atomic oxygen, leading to a good understanding of its production and destruction mechanisms, as well as densities in and outside the plasma. A brief overview of its most important properties is provided below, which also introduces a few key concepts related to species transport in the COST jet.

2.3.1 Generation of Atomic Oxygen in the COST jet

The COST jet employed in this work serves as a source of atomic oxygen, a highly reactive species relevant for many surface treatment applications [23, 54]. Atomic oxygen is generated when oxygen molecules are dissociated within the plasma. Below are given the most dominant reactions for a jet using a helium–oxygen (He–O_2) mixture. Normally, the dissociation of molecular oxygen is the dominant production pathway. However, the overall formation and subsequent decay of atomic oxygen involves multiple reaction channels, and identifying the most important processes is essential. For atomic oxygen, they are given by [77]:

$$\mathrm{e^-} + \mathrm{O_2} \longleftrightarrow \mathrm{O} + \mathrm{O^*} + \mathrm{e^-} \tag{2.20}$$

$$\mathrm{e^-} + \mathrm{O_2} \longleftrightarrow 2\,\mathrm{O} + \mathrm{e^-} \tag{2.21}$$

$$\mathrm{O^*} + \mathrm{O_3} \longleftrightarrow \mathrm{O_2} + 2\,\mathrm{O} \tag{2.22}$$

$$\mathrm{O^*} + \mathrm{He} \longleftrightarrow \mathrm{O} + \mathrm{He} \tag{2.23}$$

The generation of atomic oxygen within the jet is primarily dominated by the electron collision reactions (2.20) and (2.21). In contrast, the loss channels are mainly due to heavy particle collisions:

$$O + O_2 + He \longleftrightarrow O_3 + He \tag{2.24}$$

$$2\,O + He \longleftrightarrow O_2 + He \tag{2.25}$$

$$O + O_3 \longleftrightarrow 2\,O_2 \tag{2.26}$$

To predict the behavior of oxygen within a helium-oxygen plasma, a global model was developed by G. Park *et al.* [78]. It shows that atomic oxygen is produced over a considerable length of an APPJ's plasma channel, meaning that the maximum density does not immediately occur upon ignition, as illustrated in Fig. 2.3. Instead, the oxygen density asymptotically increases and approaches a plateau towards the end of the jet's plasma region. At this point, the production is balanced by the destruction channels of atomic oxygen, which become more effective as the atomic oxygen density increases.

In the effluent, atomic oxygen production mostly ceases because no electrons are present. Although it can still be produced through ozone dissociation by metastable species, as shown in Eq. (2.24). However, these reactions do not contribute strongly to its density in the effluent. The loss channels are unaffected by the absence of the plasma, as they do not depend on electron collisions but rather collisions with stable or at least long-lived heavy particles. This causes the atomic oxygen density outside the plasma to decrease exponentially [79].

In the case of the COST jet, the time dependency of the oxygen density in the plasma also translates into a spatial dependency. As the gas travels through the jet, a position within the jet corresponds to the gas residence time in the plasma. Knowing the gas flow velocity allows the position within the jet to be converted into a time, enabling comparison with the Park model [78]. Determining the gas flow velocity requires knowledge of the cross-sectional area of the COST jet and its flow rate.

Outside the jet, the gas flow is no longer confined to the jet's dimensions, so the effluent velocity can only be estimated based on the exit velocity of the gas from the jet. The gas flow in the effluent is assumed to be laminar, meaning it is not considerably slowed down. This assumption is particularly valid over short distances.

Fig. 2.3 shows the evolution of atomic oxygen density along the gas flow direction in the center of the discharge channel for the COST jet [**SteuerMA1**]. Within the jet, the atomic oxygen density builds up along the length of the discharge and reaches a plateau. The rise can be described using an exponential function of the form:

$$n_O = -a\left(\exp\left\{-\frac{z}{l}\right\} - 1\right) \tag{2.27}$$

Here, a corresponds to the plateau atomic oxygen density, and l represents the rise length, which can be converted into a time using the gas flow velocity. The rise time and plateau

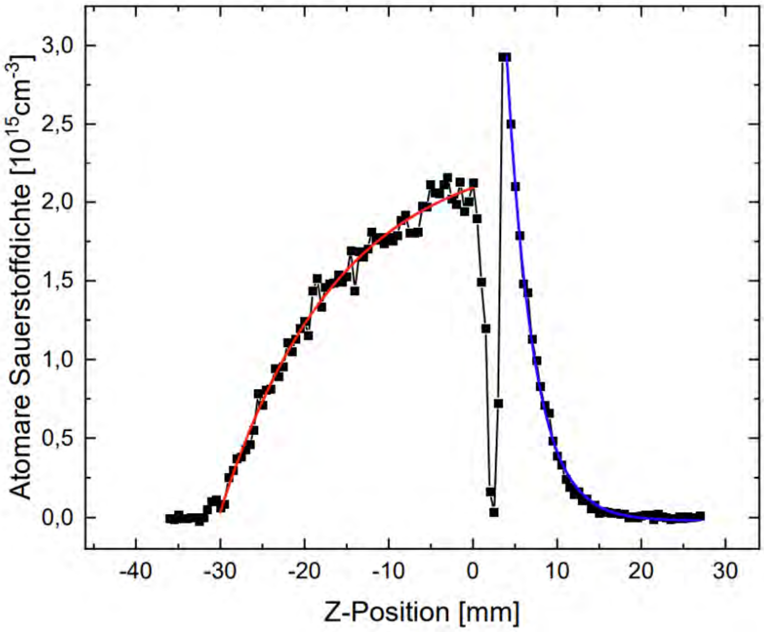

Figure 2.3: Profile of atomic oxygen density in the discharge center along the gas flow direction for the COST jet with a power of 1 W, flow of 1 slm He and an admixture of 0.5% O_2 (taken from [80]).

height depend on the power. A higher plasma power leads to a higher atomic oxygen production. Therefore the rise time is faster and the plateau higher.

After leaving the plasma, the atomic oxygen density decreases exponentially:

$$n_O = a \exp\left\{-\frac{z}{l}\right\} \tag{2.28}$$

Here, a corresponds to the initial density at the jet exit, and l represents the decay length. The rise and decay lengths can be converted into rise and decay times using the gas flow velocity.

2.3.2 Reactive Molecular Oxygen Species

As Gusakov *et al.* [28] have shown, atomic oxygen alone is not able to produce Cu(II) species and mainly forms Cu_2O in contact with a copper surface. Only when molecular oxygen is present, Cu(II) and, in particular, CuO is formed. Molecular oxygen is needed to prevent the "counter" oxidation reactions where atomic oxygen reacts with CuO to reduce it to Cu_2O. However, the slow reaction rate of ground state molecular oxygen makes it an unlikely candidate for this reaction. Here excited molecular oxygen species such as O_2(a $^1\Delta_g$) and O_2(b $^1\Sigma_g^+$) may be responsible. They have been shown to possess reaction rates several magnitudes higher than that of ground state molecular oxygen [81, 82].

The difficult-to-detect molecular species $O_2(a^1\Delta_g)$ and $O_2(b^1\Sigma_g^+)$, the first and second electronically excited states of molecular oxygen, possess an excitation energy of 0.98 eV and 1.63 eV, respectively. $O_2(a^1\Delta_g)$ is a metastable state due to its forbidden optical transition to ground state molecular oxygen $O_2(a^1\Delta_g) \rightarrow O_2(X^3\Sigma_g^-)$. It emits at a wavelength of 1270 nm and has a lifetime of up to 75 min [33]. $O_2(b^1\Sigma_g^+)$ lifetime is only 12.5 s, which is still relatively long-lived for an excited species. It emits at 762 nm. Because they are heavily quenched by ozone, knowledge of its density is critical in calculating the densities of the excited molecular oxygen species. While $O_2(b^1\Sigma_g^+)$ can be measured relatively easily by emission spectroscopy in the plasma region [32], but not in the effluent region, the determination of the $O_2(a^1\Delta_g)$ density is more complicated. Because of its long lifetime, its emission is therefore low. Additionally, the thermal background in the plasma region makes it almost impossible to measure the emission signal. Therefore, mostly effluent measurements are feasible [34, 35].

2.4 Copper Oxide Formation

The following equations provide the reaction scheme for the formation of the different Cu oxides attributed to different oxygen species [28] that can be provided by a COST jet, as shown in equations (2.29) to (2.31).

$$2\,\mathrm{Cu(s)} + \mathrm{O_2(g)} \longrightarrow \mathrm{Cu_2O(s)} \tag{2.29}$$

$$\mathrm{Cu(s)} + \mathrm{O(g)} \longrightarrow \mathrm{CuO(s)} \tag{2.30}$$

$$\mathrm{Cu_2O(s)} + \mathrm{O(g)} \longrightarrow 2\,\mathrm{CuO(s)} \tag{2.31}$$

Molecular and atomic oxygen oxidize metallic copper to Cu_2O, the first oxidation state Cu(I) of copper. CuO is the second oxidation state Cu(II) and is formed by further oxidizing Cu_2O through molecular or atomic oxygen. However, atomic oxygen is also able to reduce Cu(II) species CuO to Cu_2O as given by the “counter” oxidation reactions (2.29) to (2.31):

$$\mathrm{Cu_2O(s)} + \mathrm{O(g)} \longrightarrow 2\,\mathrm{Cu(s)} + \mathrm{O_2(g)} \tag{2.32}$$

$$\mathrm{CuO(s)} + \mathrm{O(g)} \longrightarrow \mathrm{Cu(s)} + \mathrm{O_2(g)} \tag{2.33}$$

$$2\,\mathrm{CuO(s)} + \mathrm{O(g)} \longrightarrow \mathrm{Cu_2O(s)} + \mathrm{O_2(g)} \tag{2.34}$$

With this overview of the plasma and surface chemistry related fundamentals covered, the next step is looking into the basics for surface structuring.

2.5 Laser

The other central piece of equipment for this study is a laser. This chapter gives an overview of its basic functionality as well as its effect on surfaces, especially considering laser surface structuring.

The acronym LASER stands for light amplification by stimulated emission of radiation. Lasers are classified by their long coherence length of the emitted light. The main components of lasers are:

Energy pump, an energy supply that is able to excite the atoms of the active medium, for example, through applying a current or optical pumping through flash lamps.

Active medium, where atoms or molecules are transitioned into an excited state and consequently emit the stored energy as a photon by stimulated emission within a very narrow wavelength range, with all photons being in phase.

Resonator consisting of two highly reflective mirrors, between which the amplified light travels back and forth multiple times through the active medium. Typically, one of the mirrors is partially transparent, allowing a small amount of light to be coupled out of the resonator, forming the laser beam.

2.5.1 Transverse Modes

The resonator also determines the beam shape of the laser. Induced by the resonator geometry, multiple modes can develop within a laser system, including both longitudinal and transverse modes. Longitudinal modes are generated by the light's standing wave patterns along the light path inside the resonator. They are of no particular interest to this study. However, certain electromagnetic field configurations can exist in which the amplitude and phase distributions are reproduced after reflection passes between the mirrors. These specific field patterns are known as the transverse electromagnetic modes (TEM) of a passive resonator.

Transverse modes in Cartesian coordinates are labeled TEM_{mn}, where the integers m and n indicate the number of intensity nodes, points of zero intensity, transverse to the beam axis in the horizontal and vertical directions, respectively. In cylindrical coordinates, the modes are denoted TEM_{pl}, where p and l correspond to the number of radial and angular nodes. As the values of m, n, p, or l increase, the mode order increases accordingly. The fundamental mode, TEM_{00}, has a Gaussian intensity distribution centered on the beam axis. Higher-order modes (with indices ≥ 1) exhibit additional off-axis intensity peaks arranged in a symmetrical pattern.

To accurately describe the positions and intensities of these peaks and nodes, higher-order mathematical solutions are required. These involve Hermite polynomials when using cartesian coordinates, and Laguerre polynomials in cylindrical systems. An analytical expression for the longitudinal modes can be derived from the electromagnetic wave function in vacuum:

$$\Delta E - \frac{1}{c^2}\frac{\partial^2 \vec{E}}{\partial t^2} = 0 \tag{2.35}$$

where $\vec{E}$ is the electric field of the wave. With the Helmholtz equation ($\omega = ck$) and the assumption of monochromatic waves for a plane wave in z-direction, the following differential expression can be calculated when considering the slow varying envelope approximation (SVEA) ($\frac{\partial^2 \Psi}{\partial z^2} \approx 0$):

$$\frac{\partial^2 \Psi}{\partial x^2} + \frac{\partial^2 \Psi}{\partial y^2} + 2ik\frac{\partial \Psi}{\partial z} = 0 \tag{2.36}$$

In cartesian coordinates a separation ansatz ($\Psi(x, y, z) = X(x, z)Y(y, z)$) results in the following solutions:

$$X_n(x,z) = \sqrt{\frac{\omega_0}{\omega(z)}} H_n\left(\frac{\sqrt{2}x}{\omega(z)}\right) \exp\left(-\frac{x^2}{\omega^2(z)} - i\frac{kx^2}{2R(z)} + i\frac{2n+1}{2}\zeta(z)\right) \tag{2.37}$$

$$Y_n(y,z) = \sqrt{\frac{\omega_0}{\omega(z)}} H_n\left(\frac{\sqrt{2}y}{\omega(z)}\right) \exp\left(-\frac{y^2}{\omega^2(z)} - i\frac{ky^2}{2R(z)} + i\frac{2n+1}{2}\zeta(z)\right) \tag{2.38}$$

where H_n is the n-th Hermitian polynom, $\omega_0 = \sqrt{\frac{\lambda z_0}{\pi}}$ the beam waist radius, $\omega(z) = \omega\sqrt{1 + \frac{z^2}{z_0^2}}$ the beam radius, $R(z) = z + \frac{z_0}{z}$ the curvature radius of the wave front and $\zeta(z) = \tan^{-1}\left(\frac{z}{z_0}\right)$ the Gouy-phaseshift. All depend on the Rayleigh length z_0, which is a freely selectable constant. The profile of a beam then results in the following equation:

$$I_{mn}(x,y,z) = I_0\left[H_m\left(\frac{\sqrt{x(2)}}{w(z)}\right)\exp\left(\frac{-x^2}{w^2(z)}\right)\right]^2 \times \left[H_n\left(\frac{\sqrt{y(2)}}{w(z)}\right)\exp\left(\frac{-y^2}{w^2(z)}\right)\right]^2 \tag{2.39}$$

here z is the propagation direction of the beam, $w(z)$ is the spot size where the intensity drops to $1/e^2$ of the TEM_{00} and H_i is the ith-order of the Hermite polynomial. For radially symmetric TEM the formula can be written as:

$$I_{pl}(\Phi, z) = I_0\rho^l\left[L_p^l(\rho)\right]^2\cos^2(l\Phi)\exp(-\rho) \tag{2.40}$$

where $\rho = 2r^2(z)/w^2(z)$, L_p^l is the Laguerre polynomial of order p and index l. As p increases, the modes exhibit more concentric rings, while as l increases, the modes increasingly resemble more "dumbbell" -shaped patterns as shown in Fig. 2.4. Both in cylindrical and Cartesian coordinates, the fundamental mode TEM_{00} is the same. It corresponds to a radially symmetric Gaussian distribution in intensity and is also called

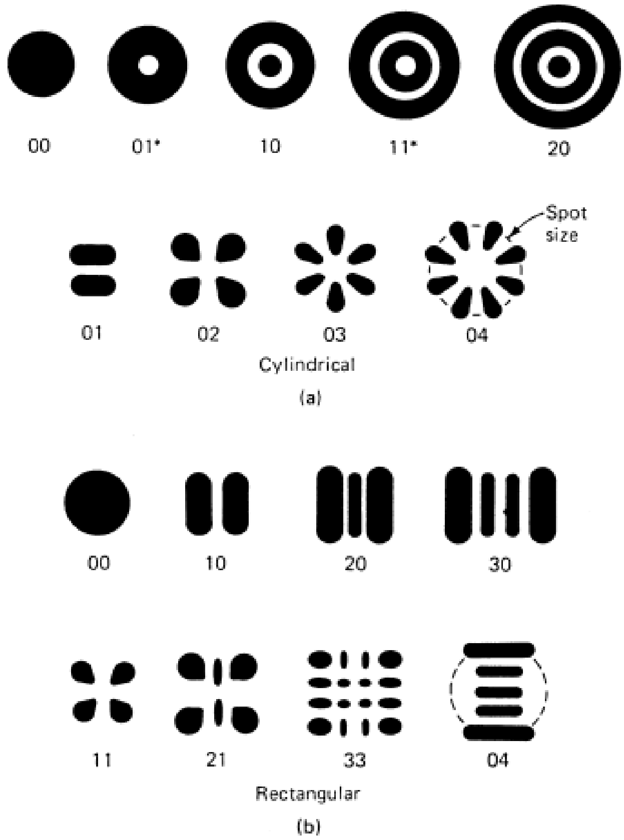

Figure 2.4: Exemplary cylindrical (a) and rectangular (b) transverse modes. The first subscript for cylindrical modes indicates the number of intensity rings. The second subscript gives the number of "dark bars" crossing the pattern. For the rectangular modes, both subscripts result in a number of bars, the first horizontal, the second vertical (taken from [83])

a Gaussian beam. All higher modes are spatially more complex.

Different transverse modes, therefore, result in distinct patterns of the intensity profile within a plane perpendicular to the laser's propagation direction. The superposition of these modes predominantly determines the beam profile of the laser.

2.5.2 Laser Beam Shape and Quality

The beam shape of a laser determines its behavior under focusing. Focusing a laser beam through a lens, for example, results in a Fourier transformation of the beam shape in its focal point. Depending on the preferred properties of the laser spot, different beam shapes can be chosen.

Gaussian Beam

A laser operating in the TEM_{00} mode possesses a Gaussian intensity profile. Its intensity distribution over the radius r is given by:

$$I(r) = I_0 \exp\left(\frac{-2r^2}{w^2}\right) \tag{2.41}$$

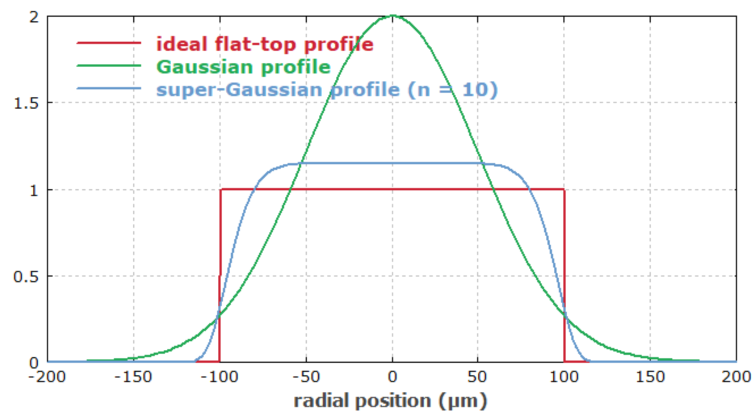

Figure 2.5: Comparison of a flat-top beam profile (red), a Gaussian (green), and a super-Gaussian (blue) intensity profile with the same optical power and the same effective mode area [84].

So the power of a Gaussian beam passing through an aperture of size $r = w$ is 86.5%. In reality, most lasers do not have a perfect Gaussian beam, but always exhibit (at least small) spatial inhomogeneities due to other modes or diffraction effects.

Flat-top Beam

Flat-top profiles, unlike Gaussian profiles, ideally have a constant intensity over a particular area and no intensity elsewhere, as shown in Fig. 2.5. To achieve this, infinitely steep intensity gradients would be required at the edges, which is why, in reality, only approximate flat-top profiles are achievable. These are also called super-Gaussian profiles, as their intensity can be described by a modified Gaussian function. In a radially symmetric plane, this would be:

$$I(r) = I_0 \exp\left(-\frac{r^2}{w^2}\right)^n \quad (28) \tag{2.42}$$

where I_0 is the peak intensity at the center, ω_0 the spot size, and n a number which gives the shape of the beam ($n = 2$ gaussian beam, $n \gg 2$ square beam). A Flat-top beam can be created through a linear combination of modes. However, this is extremely challenging. A simple and low-cost method involves blocking the outer edges of a Gaussian beam using an aperture. This process is highly inefficient, as a significant portion of the laser power is lost. Additionally, the resulting beam quality is not ideal, though it is theoretically feasible. In practice, more effective and higher-quality flat-top beam profiles are generated using various techniques.

A key distinction between flat-top beams and Gaussian beams lies in their behavior under Fourier transformation. For example, a Gaussian beam maintains its shape under a Fourier transform (e.g. focusing through a lens), whereas the Fourier transform of a flat-top profile produces an Airy disk. As a result, the flat-top profile changes over long propagation distances or when focused with lenses, a factor that must be considered during beam shaping.

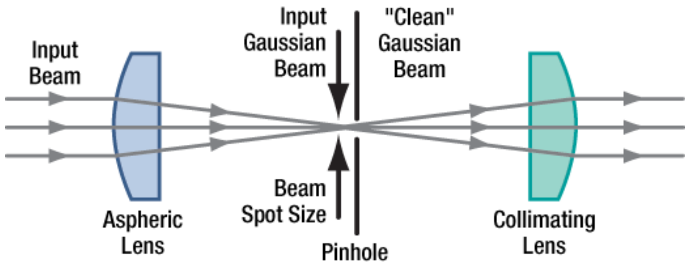

Figure 2.6: Example setup of spatial filtering by a pinhole.

Optical systems designed to generate flat-top profiles typically require a Gaussian beam as an input and utilize different optical phenomena, such as refraction or diffraction, depending on the system design. If a flat-top intensity distribution is required at the focal point, optics must first convert the Gaussian beam into an Airy disk. After passing through a lens, this Airy disk can then form the desired flat-top profile in the focus. Though a flat-top profile would be more desirable for most procedures, its challenging creation ultimately limits its use.

Pinholes as Spatial Mode Filters

Higher transverse modes can be filtered out by focusing the laser beam on a pinhole using a lens. The primary transverse mode TEM_{00} of the laser is transformed into a central Gaussian beam while noise or higher modes are transformed into side fringes. Although the Gaussian transverse modes are invariant under the Fourier transform when passing through a lens, they are focused on different spots. To achieve this, a pinhole has to be positioned precisely so that only the Gaussian TEM_{00} passes through. Thereby, the other modes are effectively filtered out as shown in Fig. 2.6, which is why pinholes in this application are referred to as spatial filters.

Especially when working with high intensities, the reflectivity, melting temperature, and general damage threshold of the material used are crucial factors. Since very high irradiation intensities are achieved by focusing, the appropriate choice of material ensures that the pinhole is not melted or torn. The size of the pinhole depends strongly on the lens used and the input beam. Edmund Optics suggests the following formula for calculating the pinhole size:

$$D_P = 1.5 D_S = 1.5 \cdot 1.27 \frac{\lambda f}{D} \tag{2.43}$$

(D_P: pinhole size, D_S: spot size of the laser at focus, f: focal length, D: input beam diameter). It should be noted that there is no single perfect pinhole size, as the diameter choice is always a trade-off between transmitted power and profile purity. Larger diameters result in a greater transmission of the original beam but may also filter out fewer higher modes. Generally, a compromise is sought.

2.5.3 Laser Pulse Length

A fundamental aspect of lasers in their interaction with materials is their pulse length. Ns-pulses are considered to have a long pulse length, while fs-pulses are at the forefront of short pulses. Ns-pluses are achieved through active Q-switching.

Active Q-switching

In the following the principle behind laser pulse duration control is explained by the example of active q-switching. To achieve controlled pulsing of the laser with pulse durations in the nanosecond to picosecond range, a quality switch (Q-Switch) is used. The Q-Switch is determined by the quality factor of the resonator:

$$Q = 2\pi \cdot \frac{\text{stored energy in the resonator}}{\text{dissipated energy per cycle}} \tag{2.44}$$

Q-switching the laser means rapidly increasing the Q-factor from a low value (low quality) to a high value (high quality) by abruptly reducing the energy losses per cycle. In practice, a distinction is made between passive and active Q-switching.

A passive Q-switch can be implemented using saturable absorbers placed within the resonator. These absorbers exhibit strong absorption (low quality) at low intensities and low absorption (high quality) at high intensities. The absorption's dependence on intensity is highly nonlinear. Depending on the crystal used, saturable absorbers can operate in transmission or reflection mode.

Passive Q-switching is challenging to control because the laser self-regulates. The pulse frequency can only be indirectly adjusted by changing the pump power or the amount of absorber material. However, due to its short switching times, passive Q-switching can produce pulses that are shorter than those produced by active Q-switching.

The quality switch used in the Nd:YAG laser is an example of an active Q-switch. In active Q-switching, the losses within the resonator are manually regulated. To achieve short pulse durations, a rapid transition from low quality to high quality is required. To this end, typically electro-optical or acousto-optical switches are used, which have switching times in the nanosecond range.

As shown in Fig. 2.7, after the resonator losses are switched from high to low absorbance, the photon flux increases due to growing stimulated emission, crossing the laser threshold, until the point where gain equals loss. The descending edge of the pulse is primarily determined by the dwell time of the photons remaining in the resonator. Due to the low gain, no further photons are generated through stimulated emission, leading to an exponential decay of intensity. The resulting laser pulse typically has a duration t_p in the nanosecond range. Active Q-switching is not suitable for generating pulses in the picosecond or femtosecond range.

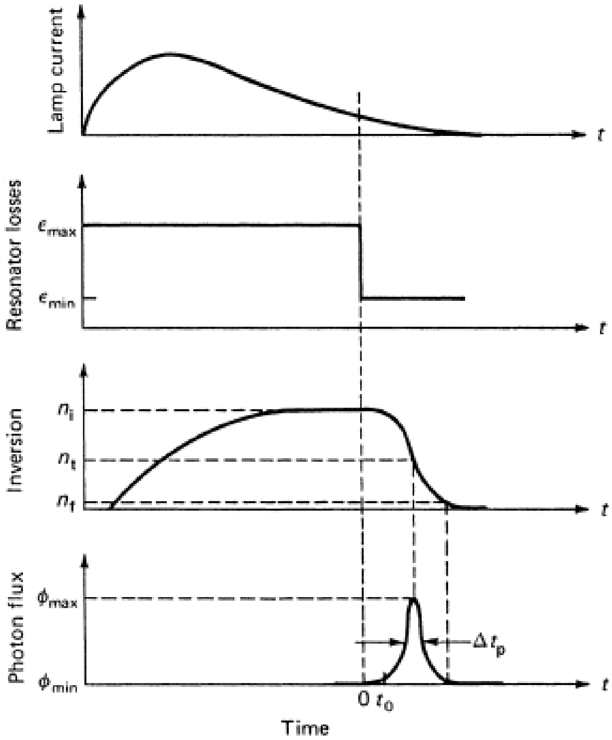

Figure 2.7: Q-switched laser pulse development. The time-dependent flash lamp current, resonator loss, population inversion, and photon flux are shown from top to bottom [83].

Ultrashort Pulse Generation

In contrast, femtosecond lasers rely on mode-locking to produce ultrashort pulses with durations on the order of 10^{-15} s. Mode-locking enforces a fixed phase relation among the longitudinal modes of the laser resonator. In multimode lasers, these modes oscillate independently, resulting in continuous-wave output with limited coherence. Mode-locking, on the other hand, forces constructive interference of resonant modes, leading to the formation of a periodic train of ultrashort pulses. The pulse duration is inversely proportional to the number of locked modes and the gain bandwidth of the active medium, making broad gain spectra essential for achieving femtosecond laser pulse timescales. Mode-locking can be realized through passive Q-switching, for example, using saturable absorbers that preferentially transmit high-intensity light. The ultrashort pulse durations achieved through mode-locking result in extremely high peak intensities, while the interaction time with the target material remains shorter than the timescales of thermal diffusion. This enables “cold ablation” with minimal collateral damage [85, 86]. Long pulses, such as ns-lasers, on the other hand, exhibit significant thermal diffusion into the surrounding material, often resulting in collateral heating and melting [87].

2.6 Laser-Induced Surface Structures

Through careful selection of laser parameters, lasers are able to induce nano-scale surface structures on a variety of materials. One aim of this study is the generation of laser-

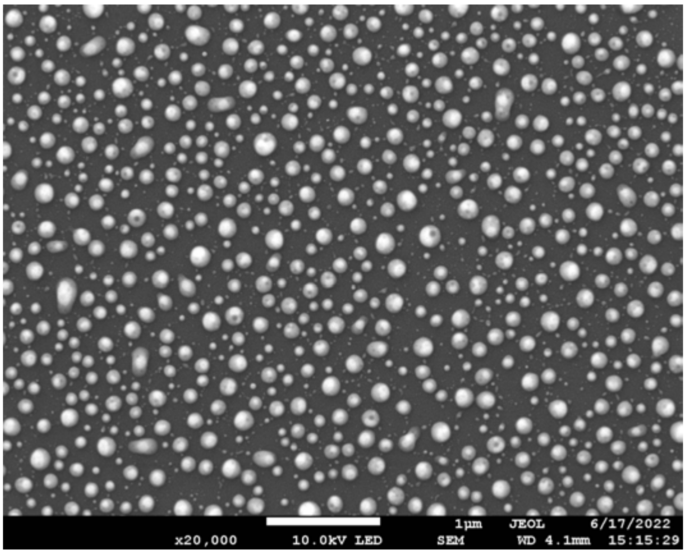

Figure 2.8: Example for PLIDS on a 5 nm copper layer on a silicon wafer after laser irradiation with a wavelength of 1024 nm.

induced surface structures to enhance catalytic properties. Surface structuring can be implemented via laser-based techniques such as pulsed laser-induced dewetting (PLID) on thin films [48] or laser-induced periodic surface structures (LIPSS) [47], that can also be induced on bulk materials.

2.6.1 Pulsed Laser-Induced Dewetting Structures (PLIDS)

The PLID mechanism generates nanoparticles by exploiting the capillary forces within a molten metal film, driving the film to minimize its high surface-to-volume ratio to the underlaying material [48, 49]. The resulting nanoparticle pattern is referred to as PLIDS (pulsed laser-induced dewetting structures) within this study, while PLID refers to the underlying formation mechanism. An example of the produced nanoparticles is shown in Fig. 2.8. While the control over input parameters is relatively simple, this method is capable of reliably producing intricate nano-patterns, making it a valuable technique for structuring surfaces [50, 51]. However, PLID generation is limited to layered materials, where a thin metallic layer is deposited on a planar substrate, such as a silicon wafer.

The leading theory in describing the formation of PLID nanoparticles was given by Trice *et al.* [48]. In their work, they describe that PLIDS are generated through the linear thin-film hydrodynamic dewetting theory (TFH). In previous works, it was discovered that the time and length scales of the dewetting process are dependent on the film thickness h. From this, it can be deduced that the PLID particle parameters, such as particle spacing R, diameter D, contact angle function $f(\theta)$, and particle density N, are also dependent on the film thickness h. Given below is a short overview of the most critical parameters that can be derived from the TFH by Trice *et al.*.

Laser irradiation melts a thin film, which causes the liquified metal to form droplets. The process is driven by the instability induced by the surface tension to the underlying material. The spinodial length or periodicity $\Lambda(h)$ of the droplet nucleation site is given by:

$$\Lambda(h) = \sqrt{\frac{16\pi^3\gamma}{A}}h^2 \tag{2.45}$$

where γ is the surface tension of the material and A the Hamaker constant, which describes the van-der-Waals force between two particles or a particle and a substrate. Λ can then be directly correlated to the nearest-neighbour particle spacing (NN-R).

When assuming the volume of the layer is conserved after PLID formation, a connection between the particle diameter D and the film thickness h can be derived via the particle spacing. If a circular section of the thin film, approximated as a cylinder with diameter R and thickness h, forms one spherical nanoparticle of diameter D, then volume conservation leads to the expression:

$$\pi R^2 h = \frac{4\pi}{3} f_\theta \left(\frac{D}{2}\right)^3 \tag{2.46}$$

where f_θ is a geometric factor depending on the particle's contact angle θ, describing the fraction of the sphere volume that lies above the substrate (for $\theta = 180°$, $f_\theta = 1$).

Using the characteristic length scale R from Eq. 2.46 and substituting into the equation above leads to a scaling law:

$$C = \left[\frac{24\pi^3\gamma}{Af(\theta)}\right]^{1/3} h^{5/3} \tag{2.47}$$

with C being a prefactor incorporating material and geometric constants, including f_θ.

The areal particle density N_A can be defined as:

$$N_A = \frac{1}{\pi R^2}, \tag{2.48}$$

where R is the nearest-neighbor spacing between particles. Using the expression for R Eq. (2.46), a thickness-dependent relation can be derived:

$$N(h) = \frac{A}{\pi^4}h^{-4}. \tag{2.49}$$

An essential aspect of the dewetting process by laser irradiation is the time scale. The dewetting process occurs on two time scales: the dewetting time scale τ_D and the liquid time scale τ_L, which describes the time the material remains molten (in a liquid state) before cooling and solidifying again. As the PLIDS formation happens over multiple laser shots, it is evident that $\tau_D >> \tau_L$. In fact, it is essential that two laser pulses remain

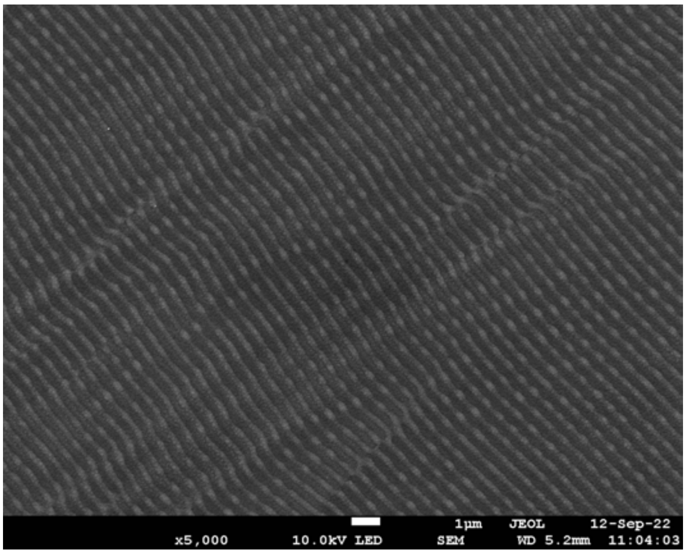

Figure 2.9: Example for LIPSS on a 5 nm copper layer on a silicon wafer after laser irradiation with a wavelength of 1024 nm.

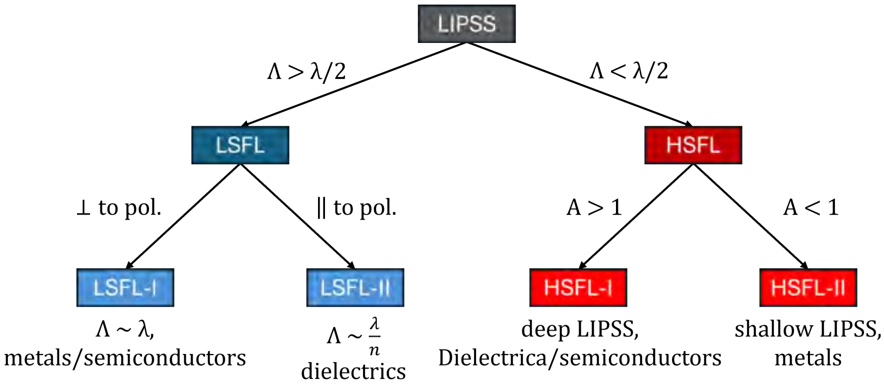

Figure 2.10: LIPSS type categorization (laser wavelength λ, LIPSS periodicity Λ, diffraction index n, depth to periodicity $A = \frac{d}{\Lambda}$) [88].

thermally independent of one another, allowing the material to cool down before the next pulse. It can therefore be assumed that the initial pulses initiate the instability, which subsequently leads to the formation of a stable dewetting pattern under subsequent pulses.

2.6.2 Laser-Induced Periodic Surface Structures (LIPSS)

Unlike PLIDS, LIPSS can be created on bulk materials, which makes them a more universally applicable surface structuring tool. One theory regarding the description of LIPSS produced by ns-lasers was provided by Sipe *et al.* [47]. The properties of the occurring LIPSS primarily depend on the laser parameters as well as the type of surface. An example of LIPSS is given in Fig. 2.9. Laser-induced structures can be observed with both continuous-wave (cw) and pulsed lasers, down to pulse durations in the femtosecond range. In fact, the formation of LIPSS is much easier to achieve with short pulses in the pico- or femtosecond range than with nanosecond lasers.

As shown in Fig. 2.10, LIPSS can be classified into Low Spatial Frequency LIPSS (LSFL)

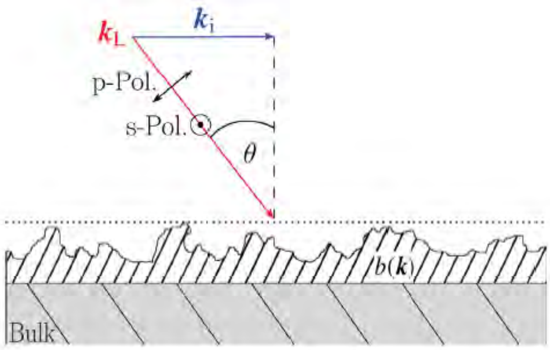

Figure 2.11: Rough surface irradiated by *s*- or *p*-polarized light (θ = incident angle)[90].

with periodicities in the range of the laser wavelength and High Spatial Frequency LIPSS (HSFL) with considerably smaller periodicities relative to the incident wavelength. The latter rely on ultrashort pulse lasers for generation and are not yet well understood. Recent investigations are therefore mainly employing fs-lasers for producing LIPSS [89].

Because HSFL are subject of recent research and the main results of this study use a ns-laser, the following description covers the physics of LSFL. LSFL can be distinguished between type-I, appearing on highly absorbing materials such as metals and semiconductors and type-II, which are formed on dielectrics. LSFL-I possess a perpendicular alignment to the laser polarization and a periodicity approximately equal to the laser wavelength. At the same time, LSFL-II align parallel to the polarization direction and scale with both the wavelength and the inverse of the refractive index of the surface.

Efficacy-Factor Theory

The most established theoretical framework for describing the formation of low spatial frequency LIPSS (LSFL) is the Efficacy Theory developed by Sipe *et al.* [47]. It explains LSFL as a consequence of the interference between the incident laser wave and surface-scattered waves generated by the initial surface roughness. The resulting spatially modulated absorption $A(\vec{k})$ determines where material modification occurs:

$$A(\vec{k}) \propto \eta(\vec{k})\,|b(\vec{k})|, \tag{2.50}$$

where $b(\vec{k})$ represents the Fourier components of the surface roughness, and $\eta(\vec{k})$ is the efficacy factor, which quantifies the efficiency of energy deposition for each spatial frequency $\vec{k}$.

As illustrated in Fig. 2.11, a laser beam with wave vector $\vec{k_L}$ and the surface projection $\vec{k_i}$ is scattered on the inhomogeneous surface of a material with a roughness $b(\vec{k})$. The surface roughness $b(\vec{k})$ varies only slowly in Fourier space, especially for uniformly rough surfaces. The efficacy factor η, on the other hand, is a more dynamic quantity. It can form distinct maxima and minima for specific wave vectors. The energy absorption of the surface, therefore, depends mainly on the efficacy factor. Consequently, LIPSS generally form at

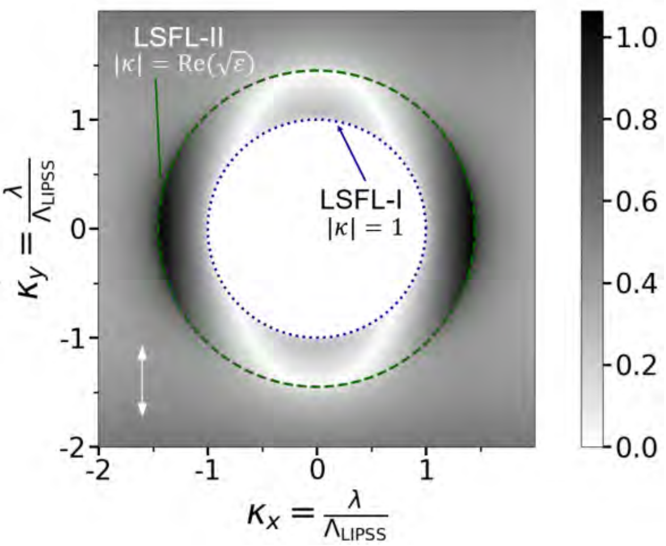

Figure 2.12: Efficacy factor map for quartz glass (26 °C, λ = 1014 nm, ϵ(1014 nm) = 2.1036, θ = 0°). The figure was taken from [91].

positions in Fourier space where the efficacy factor reaches a peak value or experiences a substantial variation. For the Sipe Theory to be applicable, the surface roughness amplitude l_s must be small compared to both the laser wavelength λ and the resulting LIPSS period Λ:

$$l_s < \lambda,\ l_s < \Lambda \tag{2.51}$$

To determine the efficacy factor η, various laser and material parameters must be known, such as the surface morphology (described by the shape factor s and filling factor F), the material's permittivity at the laser wavelength, the polarization direction (s or p), and the angle of incidence. Due to the complexity and impracticality of determining all these parameters for real-world applications, Bonse *et al.* [88] proposed a reformulation, allowing η to be computed analytically in Fourier space. For LIPSS formation, $\eta(\vec{k})$ must exhibit pronounced maxima in Fourier space. Therefore, LIPSS are produced with a spatial period Λ corresponding to those maxima:

$$\Lambda = \frac{2\pi}{|\vec{k}_{\mathrm{max}}|}. \tag{2.52}$$

By evaluating η across different positions in Fourier space, one obtains efficacy-factor maps, as illustrated in Fig. 2.12 for an example of quartz glass. These maps visualize the spatial distribution of η using grayscale intensity, with darker regions indicating higher values.

Maxima in $\eta(\vec{k})$ are directly related to the observed LIPSS orientation and periodicity.

LSFL type-I typically form perpendicular to the laser polarization, while LSFL type-II form parallel and exhibit periodicities scaled by the refractive index n:

$$\Lambda_{\mathrm{II}} \approx \frac{\lambda}{n}. \tag{2.53}$$

The rotation of the laser polarization vector results in a corresponding rotation of the LIPSS orientation without altering their period. Changes in the incidence angle θ modify $\eta(\vec{k})$, shifting its maxima in Fourier space, which leads to variations in LIPSS spacing and, in some cases, the appearance of additional structural modes.

Analysis of such maps can reveal likely locations for LIPSS formation. In Fig. 2.12, two distinct maxima are observed for quartz glass: one corresponding to the LSFL-I, which forms perpendicular to the polarization direction, and another to the LSFL-II, forming parallel to it. The LSFL-II structures are more likely to dominate due to their considerably higher efficacy factor of up to five times greater than LSFL-I.

2.7 Surface Analysis Methods

Laser and plasma treatment can induce various changes on substrate surfaces. To study their influence, a surface analysis has to be conducted. For this purpose, scanning electron microscopy (SEM) and X-ray photoelectron spectroscopy (XPS) were employed. With SEM, an investigation of the induced surface structures and morphological changes of the sample is possible, while XPS provides insights into the compositional changes or stochiometry of the sample. Their respective principle of operation is detailed below.

2.7.1 Scanning Electron Microscopy

Scanning electron microscopes (SEMs) operate by focusing a collimated beam of high-energy electrons onto a specimen surface. Via scanning it in a raster pattern, an image of the surface's morphology can be collected. The incident electrons interact with the atoms of the sample, producing a variety of signals such as secondary electrons, backscattered electrons, and characteristic X-rays. These signals carry information about the sample's surface topography, morphology, and composition. The resolution of SEM imaging is primarily determined by the wavelength of the accelerated electrons, which can be expressed by the de Broglie relation:

$$\lambda = \frac{h}{p} = \frac{h}{\sqrt{2 m_e e U}}, \tag{2.54}$$

where h is Planck's constant, m_e the electron mass, e the elementary charge, and U the accelerating voltage. Since the electron wavelength is much smaller than typical photon wavelengths and decreases with increasing acceleration voltage, SEMs can achieve a much higher spatial resolution compared to optical microscopes. The spatial resolution d can

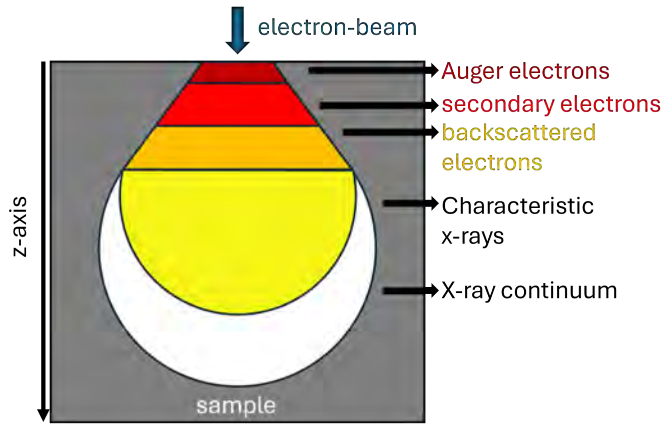

Figure 2.13: Possible electron-beam specimen interaction signals and their point of origin inspired by [92].

be approximated by Abbe's equation:

$$d \approx 0.612\frac{\lambda}{n}\sin\alpha, \tag{2.55}$$

where α is the half-angle of the aperture for the converging electron beam and n the refraction index of the medium between point source and lens. The product $n\sin\alpha$ is often called numerical aperture (NA). By combining high electron energies with precise electromagnetic lens systems, SEMs achieve resolutions in the nanometer range, enabling detailed imaging of material surfaces superior to that of conventional light microscopy.

Image formation in scanning electron microscopy relies on signals generated by the interaction of the incident electron beam with the sample material. Fig. 2.13 visualizes the point of origin of the different signals that are generated by the incident electron beam. The z-axis gives the depth withtin the sample for the various signals. These interactions can be broadly divided into elastic and inelastic processes as described by [92]. In elastic scattering, the incident electrons are deflected by the electrostatic field of atomic nuclei or by outer shell electrons of comparable energy. This process involves negligible energy loss but may lead to large-angle deviations. Electrons that are scattered through angles greater than 90° are termed backscattered electrons (BSE). They carry information related to the atomic number and composition of the sample, making them particularly useful for contrast imaging.

Inelastic interactions, on the other hand, occur when the incident electrons transfer part of their energy to the specimen's electrons or atoms. Depending on the binding energy of the affected electrons, such energy loss can result in excitations or ionizations. A key signal produced in this way is the emission of secondary electrons (SE), defined as low-energy electrons with energies typically below 50 eV. Due to their shallow escape depth, SEs provide high-resolution information about the sample's surface topography. In addition to BSE and SE, other signals such as characteristic X-rays, Auger electrons, and cathodoluminescence (x-rax continuum) are generated, which can be used for compositional and

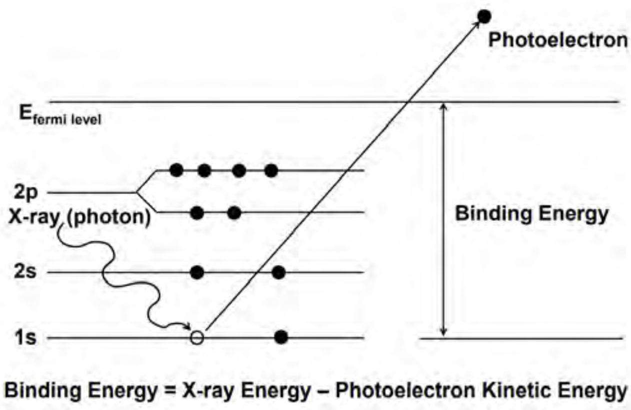

Figure 2.14: Photoelectron generation by X-ray radiation (taken from [93], originally from ULVAC-PHI manual).

analytical studies.

2.7.2 X-ray Photoelectron Spectroscopy

X-ray photoelectron spectroscopy (XPS offers an essential tool for surface chemistry analysis. The principle behind XPS is the photoeffect. An XPS device focuses an X-ray beam on a sample, which ejects photoelectrons. These are recorded as a spectrum, with an intensity corresponding to the number of detected electrons as a function of their kinetic energy (KE). The KE is typically converted to a binding energy (BE) scale for analysis. A spectrum consists of a spectral background profile, photoelectron peaks, originating from primary photoemission, and Auger electron peaks, resulting from core-hole decay. The spectral background is influenced by the analyzer mode used. The device used in this study employs the fixed analyzer transmission (FAT) mode, also known as constant analyzer energy (CAE), in which the analyzer transmission remains constant across the entire energy range. This results in a continuous background, which arises from various sources such as inelastically scattered photoelectrons, Auger electron secondary electron cascades (often originating from deeper within the sample), and electrons generated by additional photon sources, including X-ray satellites or bremsstrahlung if achromatic sources are used. Survey spectra over a wide binding energy range provide essential qualitative information, including elemental composition and relevant binding energy ranges, which are critical for planning and interpreting high-resolution measurements. Of special relevance for this study are photoelectron and Auger peaks. The mechanisms behind their occurrences are detailed below.

Photoelectron Peaks

Fig. 2.14 illustrates the generation of photoelectrons from X-rays. Monochromatic X-rays are generated through bremsstrahlung at an anode and guided towards an investigated sample. There, X-rays hit electrons in the lower orbit of an atom, which absorb the incoming photon's energy and leave the atomic orbit. The kinetic energy of ejected electrons is given by Barr *et al.* [94]:

$$h\nu = E_{kin} + E_b + q\Phi \tag{2.56}$$

where $h\nu$ is the known energy of the X-rays, E_{kin} the measured kinetic energy, E_b the material specific binding energy (BE) of the electrons, and $q\Phi$ the work function of the XPS device. The binding energy of the electrons is characteristic for an element due to their different energy levels for a specific orbit. A chemical bonding with other elements shifts the binding energy, which allows the use of electron spectroscopy for chemical analysis (ESCA) technique to identify the chemical components of a sample.

ϕ represents a work-function–like parameter associated with the specific surface of the material. In experimental measurements, this term typically includes a minor correction arising from the instrument's own work function due to the contact potential between the sample and the detector. The corresponding equation can be interpreted as an expression of energy conservation. Practically, ϕ serves as an effective instrumental correction factor, compensating for the few electronvolts of kinetic energy lost by photoelectrons as they traverse from the bulk material to the detector. In most cases, this parameter remains constant and requires little or no adjustment.

There are, however, effects that can shift the binding energy beyond scale alignment. Insulated surfaces can get charged under continuous X-ray irradiation. After the generation of a photoelectron, the sample is left positively charged. If this charge is not neutralized, it starts to accumulate, creating an electric field that hinders the further escape of photoelectrons from the sample. This alters the measured kinetic energy of the photoelectrons, resulting in a shift toward higher binding energies. A common method to prevent this charge buildup is to shower the sample with low-energy electrons. The employed XPS device within this study, ULVAC-PHI Inc. "PHI 5000 VersaProbe", also incorporates a more homogeneous neutralization of the surface by a 20 eV argon ion beam.

Some photoelectron peaks in XPS are relatively straightforward to interpret, particularly when they arise from narrow, symmetric transitions in materials with minimal background signal. As noted by Brundle and Crist [**brundle_X-ray_2020**], such cases are often intuitive in terms of background subtraction and peak isolation. However, more complex peak structures arise in many elements due to a range of processes affecting the spectra.

Effects, such as multiplet splitting, shake-up, and shakeoff events, can broaden peaks or introduce additional satellite features [95]. For example, shake-up satellite features originate from the photoexcitation process. They must be included in the overall peak intensity for accurate chemical quantification, as emphasized in works by Biesinger [96], Thomas *et al.* [97], and Brundle and Crist [**brundle_X-ray_2020**].

When dealing with such complex spectra, it is crucial to collect data over a sufficiently wide energy range to capture all relevant satellite peaks. The whole peak structure should be recorded, extending well beyond the primary peak to accommodate background sub-

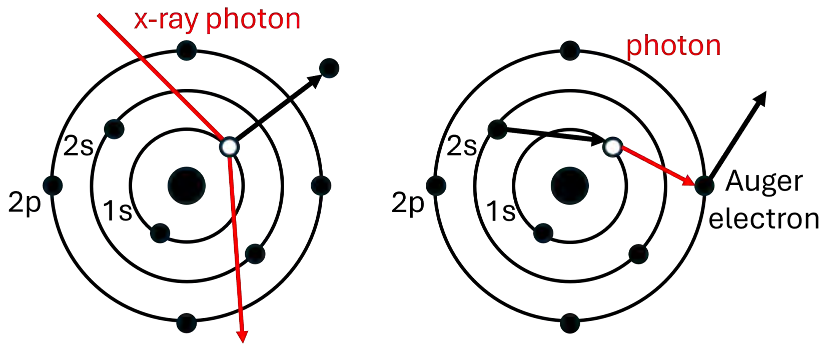

Figure 2.15: Schematic of the Auger electron generation.

traction procedures. For the most accurate elemental quantification, all relevant peak intensities, including satellites, should be incorporated in the analysis.

Auger Peaks

Auger spectra originate from a non-radiative relaxation process following core-level ionization. Fig. 2.15 illustrates the process. When a core state electron is ejected (e.g., via XPS), an electron from the shell, a higher energy level, fills the vacancy, and the excess energy is transferred to another core level electron, which is then ejected as an Auger electron. Unlike photoelectrons, the kinetic energy of an Auger electron is independent of the photon energy and depends solely on the electronic structure of the atom. Their energy is given by:

$$E_{kin,Auger} = E_{core\ state} - E_{shell} - E'_C \tag{2.57}$$

where $E_{kin,Auger}$ is the kinetic energy of the Auger electron, $E_{core\ state}$ the potential energy of the core level ionization, E_{shell} the energy of the outer shell electron, and E'_C the energy of the core level electron that absorbs the emitted photon.

In XPS, Auger peaks provide complementary chemical information, especially useful for elemental identification and distinguishing between oxidation states, when the photoelectron peaks are superimposed and hard to deconvolute. Their kinetic energies and characteristic line shapes are sensitive to the chemical environment, making them valuable for surface and chemical state analysis. However, Auger peaks generally have a more complicated shape than photoelectron peaks, requiring a more careful deconvolution.

Shake-up Peaks

Shake-up peaks or satellites arise from multi-electron interactions during the photoemission process. When a core-level electron is ejected, a valence electron may be simultaneously excited to a higher unoccupied energy level, resulting in a photoelectron with slightly reduced kinetic energy. This creates a satellite peak at higher binding energy (lower kinetic energy) relative to the main photoelectron peak, which is referred to as a shake-up peak.

Shake-up features are especially prominent in systems with strong electron correlation, such as transition metal compounds. Although they are generally not used for quantitative analysis, their presence may indicate the presence of specific chemical states. Recognizing and including shake-up peaks in data analysis is therefore very helpful for accurate chemical quantification and interpretation of complex spectra in XPS.

Observation Depth

An important parameter for XPS measurements is the observation depth d, the length scale in which X-rays can intrude into the material and electrons can escape to be detected. It can be calculated by:

$$d = 3\lambda_{pe} \sin\Theta \tag{2.58}$$

where λ_{pe} is the inelastic mean free path and Θ the X-ray incident angle on the substrate in rad. λ_{pe} is given by [98]:

$$\lambda_{pe} = \left(\frac{2170}{E^2} + 0.72 \cdot \sqrt{aE}\right) \cdot a \tag{2.59}$$

here E is the kinetic energy of the samples element ($E = E_{photon} - E_{binding}$) and a is the monolayer thickness:

$$a^3 = \frac{A}{\rho n N} \times 10^{24} \tag{2.60}$$

where A is the standard atomic weight, n the number of atoms in the molecule, N the Avogadro constant and ρ the bulk density in kg m^{-3}.

For the case of copper, the monolayer thickness can be calculated to $a = 0.228$ nm. This results in an inelastic mean free path of $\lambda_{pe} = 1.85$ nm. The “PHI 5000 VersaProbe” possesses an analyzer angle of 45°. The observation depth of the XPS, therefore, calculates to $d = 3.92$ nm. The oxidation of the copper layer influences this by reducing the monolayer size. For the much lighter CuO, for example, this would result in an observation depth of $d = 3.10$ nm.

3 Experimental Setup

To study the various aspects, such as species densities and surface modification, a multitude of experimental setups had to be employed. The setups can be broadly separated by the spectroscopy measurements performed for the investigation of the species densities and the surface modification setup with the COST jet utilized in both. Therefore, a general overview of the jet is given below.

3.1 COST jet

The plasma source used in this study is the capacitively coupled microplasma jet known as the “COST Reference Microplasma Jet” [53]. It was a central component in all experimental setups within this study, although its installation varied strongly. It operates at a radio frequency of 13.56 MHz using a plane electrode configuration. The discharge channel between the electrodes is cubic in shape. It has an area of 1 mm × 1 mm and a length of 30 mm. Two quartz glass planes are glued to the sides of the electrodes, providing optical access.

For all experiments, the gas supply of the COST jet consisted of one or multiple mass flow controllers (MFCs) that regulated the gas admixture and flow rate. Helium was used as a carrier gas, as it cools the electrodes and prevents thermal instabilities within the discharge due to the gas’s high thermal conductivity. As an admixture, molecular oxygen was used. The COST jet’s production of reactive oxygen species, especially atomic oxygen, is well-investrigated [54, 55], making it an ideal candidate for studying its effects on the chemical composition of treated surfaces.

Besides the flow and admixture, the dissipated plasma power is an important control parameter. In case of the COST jet, it can be measured by the method presented in Golda *et al.* [53]. A voltage and current probe are located inside the COST jet’s housing. This allows the measurement of the applied voltage and resulting current through an external connection to an oscilloscope. The measured voltage and current at the probes are correlated to the actual applied voltage using a calibration factor, which must be measured beforehand. The dissipated plasma power can then be calculated by:

$$P = U\ I\ \cos\left(\Phi - \Phi_0\right) \tag{3.1}$$

where U and I are the voltage and current and Φ is the phase shift between them and

Φ_0 a reference phaseshift. Through the COST power monitor program [99], the plasma power and a fast oscilloscope (> 10GS/s), the dissipated plasma power can be calculated in real time. However, a reference phaseshift has to be taken before every measurement.

3.2 Spectroscopy Setup

To measure the reactive molecular oxygen densities produced by the COST jet, optical spectroscopy methods were used. A central part of the reactive molecular species density investigation was their transport or flux to a sample. Therefore, the measurements were conducted in the effluent of the COST jet. The optical setups for the absorption spectroscopy of ozone and emission spectroscopy of $O_2(a^1\Delta_g)$ shared a very similar setup as detailed below. A sketch of the setup is shown in Fig. 3.1. It will be described in more detail in the sections about the spectroscopy methods.

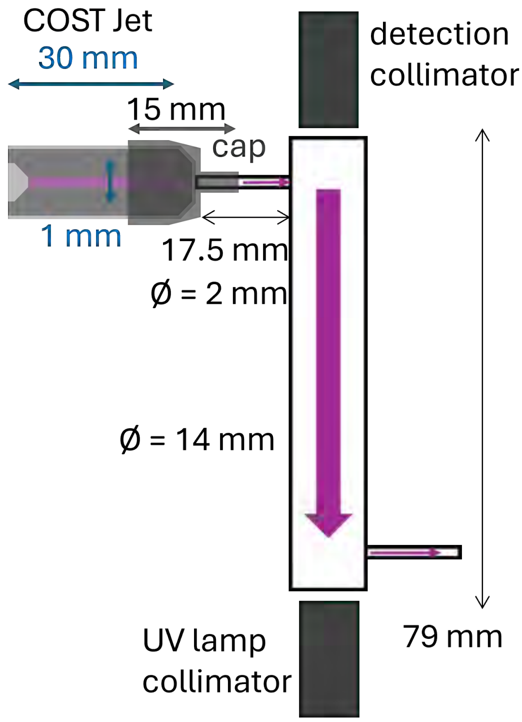

Figure 3.1: Schematic of the quartz flow cell dimensions and the connection to the COST jet, as well as the position of the collimators for the optical setups. The purple arrows indicate the gas flow direction.

3.2.1 Flow Cell

The densities of various reactive species can be determined using emission and absorption spectroscopy. However, applying these methods in the effluent of a COST jet is often difficult due to typically low emission in cross-field configuration APPJs [100], the small observable volume [34, 35], and the short absorption path lengths inherent to the effluent geometry [101]. Achieving a sufficient signal-to-noise ratio in spectroscopic measurements generally requires either a large detection volume or extended optical paths. This is particularly important when detecting weakly emitting, long-lived species such as $O_2(a^1\Delta_g)$ [34, 35].

To address this, a gas flow cell was employed to confine the effluent, thereby enhancing the detection volume for both emission and absorption processes. Although the gas flow cell does not provide spatially resolved data on species distribution within the effluent, it offers a means to estimate the average density of long-lived species generated by the COST jet. A schematic of the setup is presented in Figure 3.1. The cell is constructed from quartz glass to ensure UV transparency, which is necessary for absorption spectroscopy. It is connected to the COST jet via a plastic cap, which channels the effluent from the jet's cubic discharge channel into a 17.5 mm long cylindrical tube with a 2 mm diameter. From there, the flow enters the cylindrical gas flow cell, which has an inner diameter of 14 mm and a length of 79 mm. Optical access is enabled by planar windows at both ends of the flow cell. Additionally, a long outlet pipe is attached to prevent ambient air from flowing back into the cell.

3.2.2 Optical Spectroscopy

Absorption Spectroscopy of Ozone

Knowledge of the ozone density is crucial due to its significant quenching effect on excited molecular oxygen species. The shared optical setup of the absorption spectroscopy measurement is shown in Fig. 3.1 and employs the technique as proposed by [102]. Light of a calibrated lamp was guided through the flow cell and measured at the other end with a spectrometer. This way, a volume-averaged absorption signal could be collected in the flow cell.

The light source used for absorption spectroscopy was a laser-driven broadband lamp (Energetiq EQ-99 LDLS). The light was guided through a fiber attached to the UV lamp and a collimator, which parallelized the light to a beam diameter of 13 mm. This matched the dimensions of the gas flow cell. The light passed through a narrow bandpass UV filter (Edmund optics bandpass filter, OD 4, CW = 254 nm, FWHM = 10 nm). This wavelength range fits to the absorption of the Hartley band of ozone. It reduces the energy input of the UV light, preventing the dissociation of O_2 and thus an artificial increase in the ozone formation. At the end of the gas flow cell, another collimator and optical fiber were used to guide the light into a UV-sensitive spectrometer (Avantes AVASPEC-ULS-2048x64TEC-EVO, UV sensitive from 200 nm to 720 nm; resolution 0.3 nm). The intensity of the absorption spectra was calculated from the averaged intensity within the filter wavelength range (approx. 250-260 nm)

The ozone density was determined using absorption spectroscopy, with all spectra having an integration time of 1 second. It was ensured beforehand that the signal remained stable over time by monitoring it for a few minutes, confirming consistency once the jet was heated up. An initial spectrum of the broadband lamp was recorded just before igniting the plasma (I_0), followed by a spectrum taken every minute for 5 minutes after plasma ignition (I_{T}), IT), ensuring the measurement was performed in an equilibrium state of the ozone density within the flow cell. After each measurement, a minimum of 10 minutes was allowed for the absorption signal to reset to an undetectable level by flushing the cell with the gas flow.

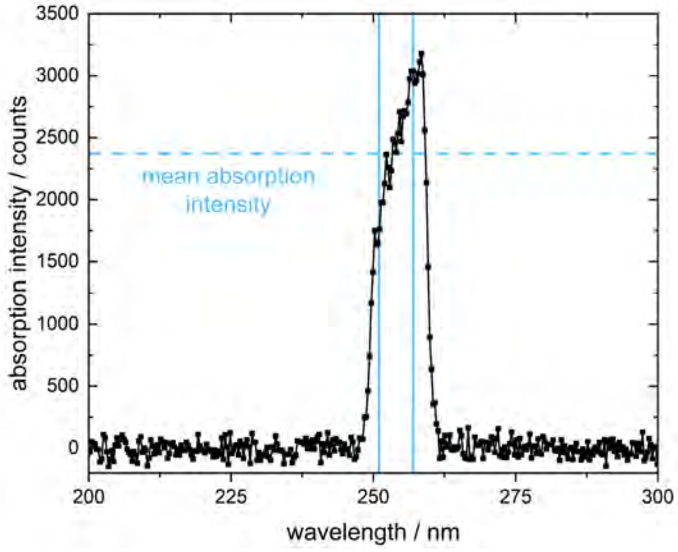

Figure 3.2: Mean absorption intensity of the ozone absorption spectra.

Fig. 3.2 visualizes the calculation of the mean absorption intensity of ozone. The intensity of the absorption spectrum was calculated by taking the mean intensity between 251 nm and 257 nm. The ozone density was then calculated using Lambert-Beer's law. Ozone's absorption coefficient was taken from Inn *et al.* [103] as shown in Fig. 3.3.

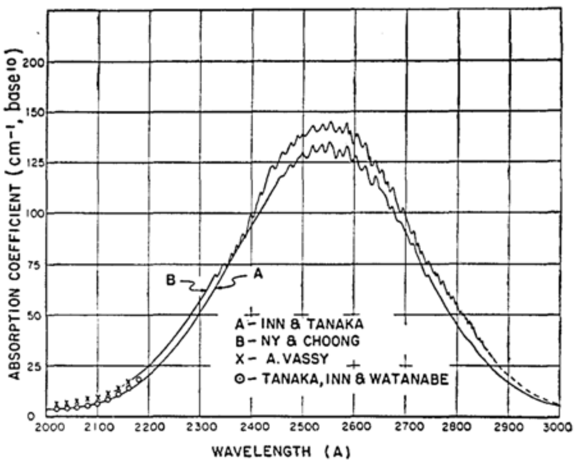

Figure 3.3: Ozone absorption coefficient as a function of wavelength in the range of 200–300 nm (image taken from [103]).

Energy-Intensity Calibration Setup

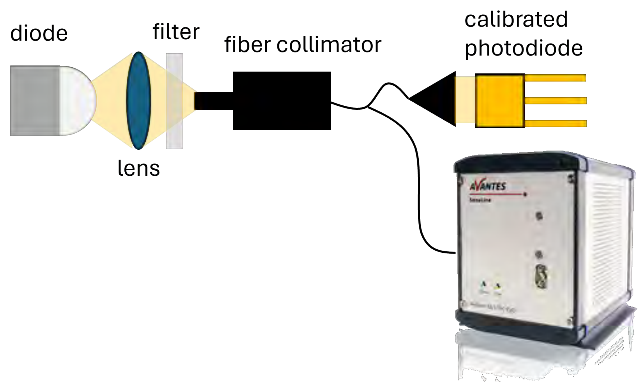

Figure 3.4: Optical setup for the wavelength-specific energy-intensity calibration of the spectrometer.

The $O_2(a^1\Delta_g)$ and $O_2(b^1\Sigma_g^+)$ densities could be calculated from their emission by conducting an energy calibration of the spectrometer. This was achieved by an absolutely calibrated photodiode. The method is inspired by [35], although no previous literature for its application to $O_2(b^1\Sigma_g^+)$ was found. This allowed to relate the intensity measured by the spectrometer to an emission power. The setup is shown in Fig. 3.4. For the $O_2(a^1\Delta_g)$ density, a laser diode (RLT1270-20MGS-B; PW = 1270 nm, FWHM = 0.3 nm) was used with the same emission wavelength as $O_2(a^1\Delta_g)$. It was placed at the end of the collimator, where it gathered the emission signal from the flow cell or the jet plasma volume and coupled it into the fiber. The fiber was then either connected to a calibrated photodiode or the spectrometer. The optical setup was unchanged when switching the fiber between the spectrometer for the intensity measurement and the photodiode for the power measurement. The intensity of the laser diode was measured and compared to the measured radiative power given by an absolutely calibrated InGaAs-photodiode (Thorlabs FGA21-CAL; wavelength range: 800 - 1700 nm). This allows the calculation of the energy-intensity calibration constant $C = \frac{I_0}{P \cdot t_{\mathrm{Int}}}$, where I_0 is the peak intensity of the laser diode at 1270 nm, P the measured power of the calibrated photodiode and t_{Int} the integration time of the spectrometer.

The $O_2(b^1\Sigma_g^+)$ signal had to be calibrated similarly as described for $O_2(a^1\Delta_g)$. Here, an LED (Thorlabs LED760L; PW = 760 nm, FWHM = 24 nm) was employed, instead of a laser diode. An optical filter (CW = 760 nm, FWHM = 10 nm) was placed between diode and spectrometer. It led to a more comparable power measurement between the calibrated diode and the spectrometer, as the width of the $O_2(b^1\Sigma_g^+)$ spectrum is similar to the spectral width of the filter. The intensity of the spectrometer signal was then integrated over the spectral width and compared to the energy of a calibrated Si-photodiode (Thorlabs FDS100; wavelength range: 350 - 1100 nm).

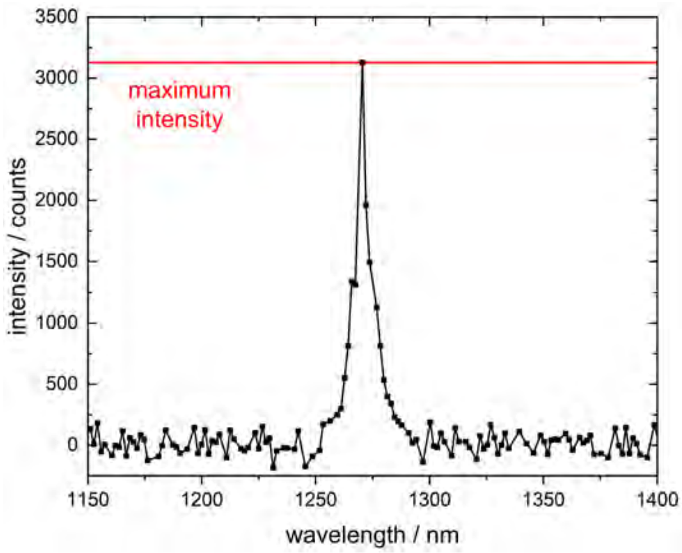

Figure 3.6: Maximum intensity for the $O_2(a^1\Delta_g)$ spectra.

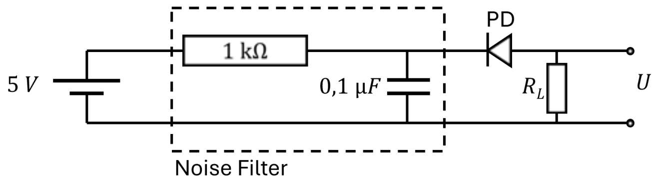

Figure 3.5: Circuit schematics for the absolutely calibrated photodiode.

Fig. 3.5 shows the schematics for the circuit of the diode setup for the power calibration. The resistance could be changed to adjust the sensitivity of the output voltage. The optical power (P_{photo}) can then be calculated by:

$$P_{\text{photo}} = \frac{U_{diode}}{R_L \cdot C(\lambda)} \tag{3.2}$$

Here, U_{diode} is the measured voltage from the diode, R_L is the diode resistance, and $C(\lambda)$ is the wavelength-dependent efficiency of the diode.

Emission Spectroscopy of $O_2(a^1\Delta_g)$

Fig. 3.1 shows the shared optical setup for the $O_2(a^1\Delta_g)$ detection as proposed by [35], although the UV lamp collimator has no use here. The setup allowed to measure a volume-averaged intensity in the flow cell. The emission of the $O_2(a^1\Delta_g)$ at 1270 nm was collected by the detection collimator and guided through an optical fiber into an infrared sensitive spectrometer (Avantes AVASPEC-NIR512-1.7HSC-EVO, NIR150-1.2 use from 900 nm to 1695 nm; wavelength resolution 0.3 nm). The collimator had a diameter of approx. 10 mm, which allowed to gather the emission passing through the plane quartz windows of the gas flow cell.

Table 3.1: Quenching coefficients of different reactive species with $O_2(a^1\Delta_g)$ calculated using their respective densities and rate coefficients. Rate coefficients are taken from [105].

Reaction	q_i / s^{-1}	k_i / $cm^3\,s^{-1}$	n_i / cm^{-3}
$O_2(a^1\Delta_g) + O_2 \longrightarrow 2\,O_2$	0.1	$1.5 \cdot 10^{-18}$	$5.0 \cdot 10^{16}$
$O_2(a^1\Delta_g) + O \longrightarrow O_2 + O$	0.8	$2.0 \cdot 10^{-16}$	$4.0 \cdot 10^{15}$
$O_2(a^1\Delta_g) + O_3 \longrightarrow O + 2\,O_2$	12.1	$4.0 \cdot 10^{-15}$	$3.0 \cdot 10^{15}$
$O_2(a^1\Delta_g) + He \longrightarrow O_2 + He$	0.1	$1.0 \cdot 10^{-21}$	$1.0 \cdot 10^{19}$

An example of the $O_2(a^1\Delta_g)$ spectra is shown in Fig. 3.6. The $O_2(a^1\Delta_g)$ emission spectra were time integrated over 10 s. Generally, the $O_2(a^1\Delta_g)$ emission had its maximum intensity at 1270 nm as shown in 3.6.

An important step to deduce the $O_2(a^1\Delta_g)$ density from the emission was the energy calibration of the spectrometer. To this end, an absolutely calibrated diode was used as described in the energy-intensity calibration setup. The $O_2(a^1\Delta_g)$ density can then be calculated by the following equation [32, 35, 104]:

$$n_{O_2(a^1\Delta_g)} = I \cdot C \cdot \frac{1}{A_{ik} \cdot Q} \cdot \frac{\lambda}{h \cdot c} \cdot \frac{1}{V} \cdot \frac{1}{f(d\Omega) \cdot g} \tag{3.3}$$

where I is the intensity, C is the wavelength dependent energy-intensity calibration constant of the spectrometer, V the volume of the flow cell. A_{ik} is the Einstein coefficient of $O_2(a^1\Delta_g)$ ($A_{ik} = 2.22 \cdot 10^{-4}$ s^{-1} [33]). $Q = \frac{A_{ik}}{A_{ik}+q}$ is the photon yield, which relates the observable radiative transition to the non-radiative decay of the $O_2(a^1\Delta_g)$ molecule. $q = \sum_i k_i n_i$ is the quenching rate. $f(d\Omega) = 2.7 \cdot 10^{-3}$ is the geometric factor, which was calculated by a Monte Carlo simulation that evaluated the probability that a photon emitted in the flow cell volume will reach the detector. $g = 0.63$ is the loss factor of the optical components (estimated through the transmission of the optical components).

Table 3.1 shows the quenching rates of the most prominent quenching partners for $O_2(a^1\Delta_g)$. Ozone possesses by far the highest rate coefficient, which simplifies Eq. 3.3 to $q = k_{O_3} \cdot n_{O_3}$, with k_{O_3} being the quenching rate coefficient of ozone with $O_2(a^1\Delta_g)$ and n_{O_3} the ozone density. The previously acquired data for the ozone density of the experiment is used to calculate the absolute $O_2(a^1\Delta_g)$ density.

Emission Spectroscopy of $O_2(b^1\Sigma_g^+)$

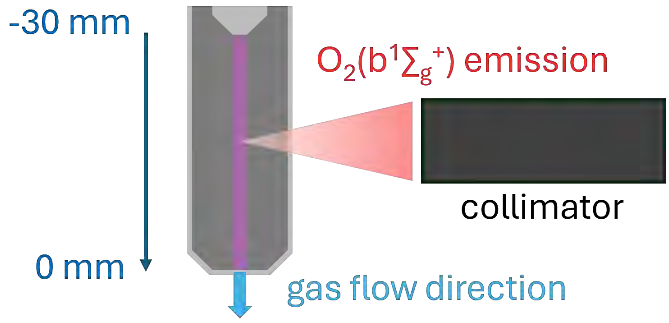

Figure 3.7: Emission spectroscopy setup for the $O_2(b^1\Sigma_g^+)$ measurement in the jet. Blue arrow indicates gas flow direction.

The setup for the $O_2(b^1\Sigma_g^+)$ emission spectroscopy is shown in Fig. 3.7. The emission was directly collected in the plasma region of the COST jet without the use of the flow cell. $O_2(b^1\Sigma_g^+)$ emits at 760 nm and was captured with the infrared sensitive spectrometer used in the $O_2(a^1\Delta_g)$ measurement. The integration time was 1 s. The emission was measured in the discharge channel of the COST jet because the relatively short lifetime of $O_2(b^1\Sigma_g^+)$ quickly reduces its density beyond the detection threshold outside of the COST jet.

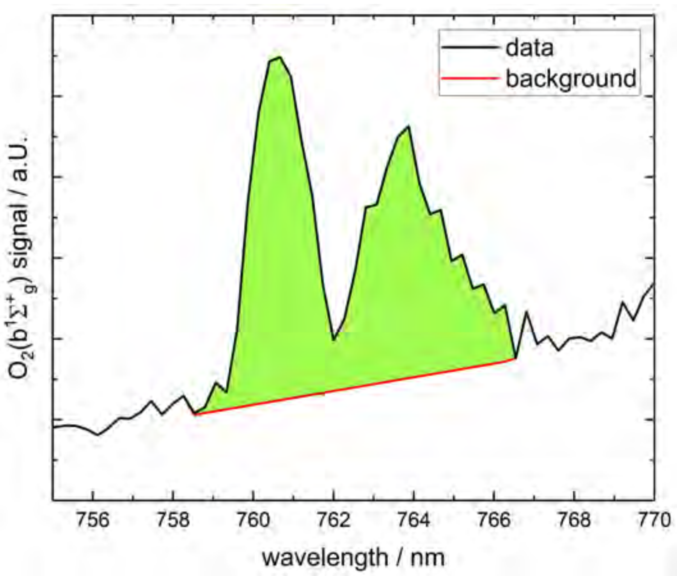

Figure 3.8: $O_2(b^1\Sigma_g^+)$ emission spectrum and intensity calculation.

Fig. 3.8 shows an example molecular emission spectrum of $O_2(b^1\Sigma_g^+)$. The emission intensity was the wavelength-integrated emission signal of $O_2(b^1\Sigma_g^+)$ over the background (indicated by the green area).

3.3 Surface Modification Setup

Besides the spectroscopy setups used to investigate different plasma species, the jet was also employed in the surface modification setup, although heavily modified to meet experimental requirements, which will be covered later in this chapter. The following section describes the main components of the combined laser-plasma treatment setup, beginning with a description of the various substrates used and then detailing the actual experimental setup.

3.3.1 Copper Samples

Within this study, two kinds of samples were investigated. (I) Copper films deposited on silicon wafers offered a highly homogeneous surface roughness, which eases laser structuring. The primary focus lay on copper thin films (10 nm and below), but also thicker layers ($h > 100$ nm) were investigated. (II) Additionally, the study looked into copper foil (99.95% OFHC Copper Foil 0.1 mm thick hard (CV00-FL-000261) from Goodfellow) as a bulk material more suited for application purposes. However, its high initial surface roughness provides a challenge for laser structuring. Therefore, electropolishing was used to smooth the surface, which also eases the surface analysis.

Copper Thin Film Deposition

The copper samples are silicon wafers with a copper layer deposited by high-power impulse magnetron sputtering (HiPIMS) [106, 107]. The experimental setup of the chamber is shown in Fig. 3.9.

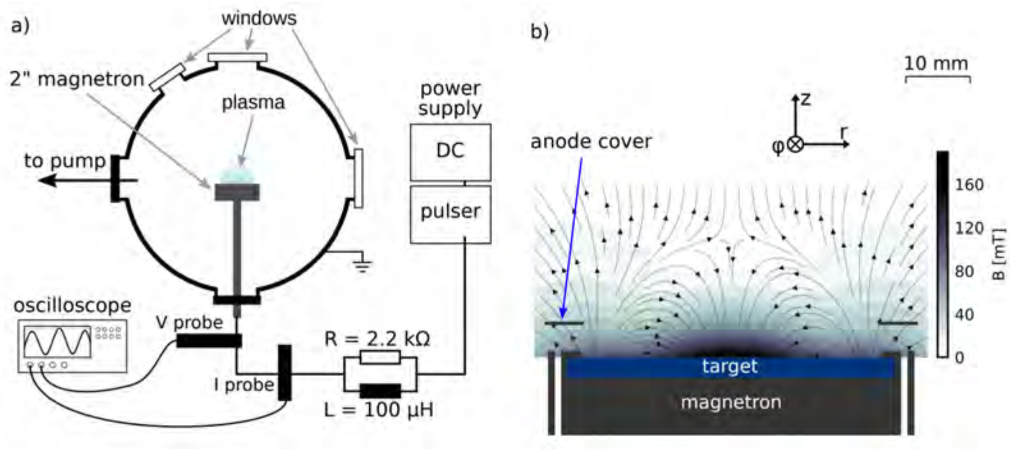

Figure 3.9: a) Experimental setup: Vacuum chamber, magnetron, and electrical connection to the power supply. b) Enlarged magnetron view with magnetic field configuration. B-field was reconstructed with Hall-probe measurements, developed by Krüger *et al.* [108]. The colormap shows the absolute magnetic field strength. (image taken from [109])

Table 3.2 shows the employed generator settings of the HiPIMS chamber. For the deposition, high plasma powers, close to the maximum plasma power, were used. This resulted in a strong adhesion of the copper film to the silicon wafer. The deposition rate was determined to 0.9 nm/s. This knowledge enabled a precise layer thickness control. Additionally, the HIPIMS deposition yielded a smooth surface morphology, perfect for laser structuring and morphological investigations. Its roughness R_q of 0.2 µm was measured by a laser spectroscopy microscope (Keyence VK-9710). The higher layer adhesion from HiPIMS deposition also proved critical for PLID particle formation, as layers deposited with direct current magnetron sputtering (DCMS) led to layer ablation under laser irradiation.

Table 3.2: HiPIMS chamber generator settings for copper deposition

setting	value
voltage / V	740
current / A	109
frequency / Hz	35
pulsetime / µs	50
pressure / mbar	$5.2 \cdot 10^{-3}$

Electropolishing Setup

The copper foil was cut into 30 mm × 5 mm strips. The rough initial surface of the copper foil (99.95% OFHC Copper Foil 0.1mm thick hard (CV00-FL-000261) from Goodfellow) was smoothed by electropolishing. Fig. 3.10 shows the electropolishing setup. Before treatment, the copper foil was cleaned in distilled water. The copper foil and the stainless steel plate were submerged in phosphoric acid. Both were connected to a voltage generator using steel clamps. The copper cathode was then set to 3 V, which resulted in a current of 0.1 A. A treatment time of 300 s resulted in smooth surfaces with minimal material loss. The initial surface roughness of R_q = 3.1 µm was measured by LSM. After electropolishing, the roughness could be reduced to 1.5 µm. It should be noted that the roughness measurements were averaged over an area of 10 mm. Within the size of the laser spot of up to 500 µm, the roughness was much lower at under 1 µm, as can be seen in the later presented SEM image of the electropolished copper foil (Fig. 4.29).

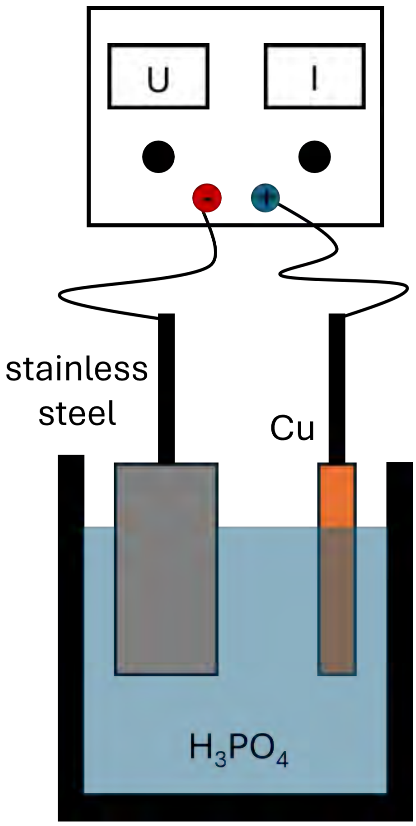

Figure 3.10: Setup sketch of the electropolishing of the copper foil cathode using a stainless steel anode in orthophosphoric acid. Copper foil and a steel plate were connected to a voltage generator.

3.3.2 Nd:YAG Laser System

For surface structuring, a frequency-doubled Nd:YAG laser by Continuum with a wavelength of 532 nm running at 20 Hz was used. Investigation of successful surface structuring laser parameters necessitated a control over

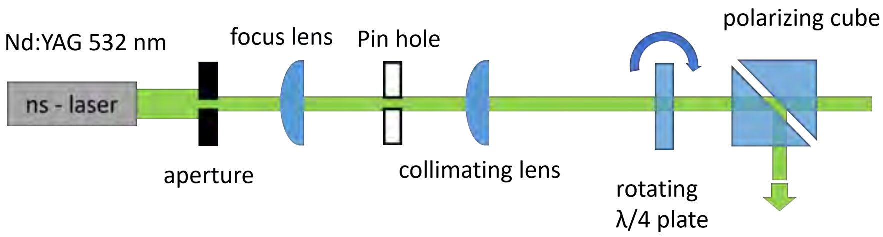

Figure 3.11: Main optical components of the laser system.

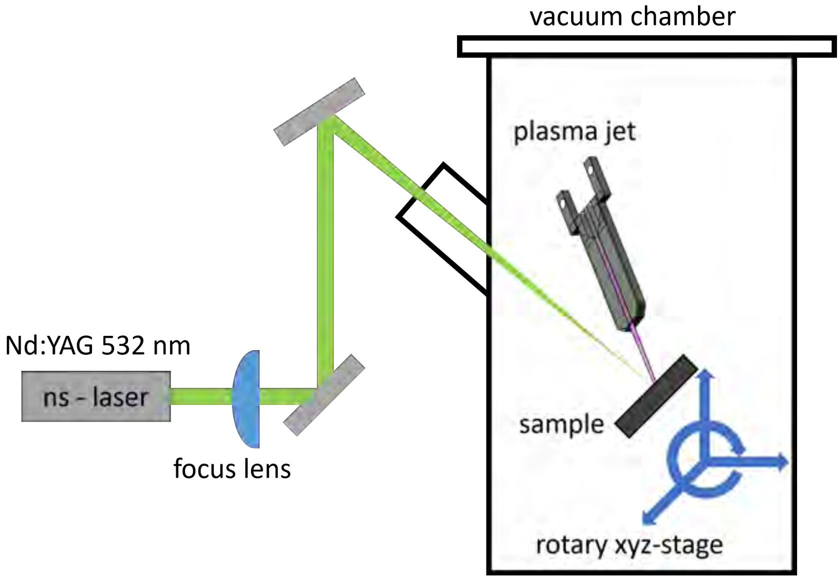

Figure 3.12: Setup for the sample treatment, combining plasma treatment and laser irradiation

the pulse energy and a high beam quality. Fig. 3.11 shows the optical components of the laser system. Beam quality enhancement by a pinhole provided a Gaussian laser energy distribution profile, which is further elaborated on in the Results chapter. Its energy and beam shape were measured using a laser energy probe and a beam profiler (gentec-eo Beamage 3.0). The laser energy could be varied through a combination of a polarizing beamsplitting cube (Thorlabs CCM1-PBS25-532-HP/M 30mm Cage Mounted HP Polarizing BS Cube 532nm from Thorlabs) and a 1/4-λ waveplate (Thorslabs WPMQ05M-532 Mounted Multi Order 1/4 Waveplate 532nm). The polarizing cube filters light according to its polarization. P-polarized light can pass through, while s-polarized light gets coupled out. Light of the laser would pass through the 1/4-λ waveplate, which, depending on the rotation, aligns the electric field either parallel (p-polarized) to the incident plane of the polarizing cube or perpendicular to it (s-polarized). Therefore, turning the waveplate changes the amount of light that is filtered out. Additionally, the amplifier of the laser system was turned off. This resulted in a laser energy of up to 1.03 mJ after the pinhole.

3.3.3 Combined Laser-Plasma Surface Treatment Setup

The surface treatment aims to combine laser irradiation with reactive species provided by a COST jet. The experimental setup is shown in Fig. 3.12. The sample is mounted on a stage that can move in all spatial directions and can be tilted relative to the laser beam. It was rotated so that the laser was aligned parallel to the sample surface normal. The COST jet effluent was lined up with the laser spot position on the sample to provide the gas stream directly to the irradiated area. The COST jet was shifted 45° degrees to the side of the laser's position, thus hitting the surface at an angle of 45°. The distance between the COST jet and the sample could be varied by moving the stage. As an optimal distance between jet and surface 5 mm was chosen, identified by the reactive species measurements presented later in the Results chapter. The flow of helium and oxygen could be adjusted using mass flow controllers (Analyt-MCT). For the gas admixture, mostly 1 slm He with 0.5% O_2 was chosen, as it provided the highest production of atomic oxygen [54], which plays a key role in the oxidation of copper [110]. This admixture also provided a suitable ratio between atomic oxygen and $O_2(a^1\Delta_g)$ for a distance of 5 mm to facilitate the chemical processes given by Gusakov *et al.* [28] as shown in the reactive species results chapter. To mitigate the effects of unknown reactive species in ambient air, the laser-plasma treatment was conducted inside a vacuum chamber with a controlled atmosphere at 980 mbar, using the same admixture as the gas flow.

To investigate the influence of laser and plasma treatment on the surface, the treatment time has to be adjusted precisely. Furthermore, it had to be ensured that the treatment with laser and plasma occurs simultaneously to observe if the combined treatment of laser and plasma induces unique changes to the surface. To this end, the plasma and laser treatment were synchronized. An external delay generator was used to trigger the Q-switch pulse of the laser at the required frequency of 20 Hz. Additionally, it was connected to a processing unit (ARDUINO UNO) that used the signal as a trigger for a step motor that handled a laser shutter. It was installed right before the window where the laser entered the chamber. When starting a measurement, the shutter would open when a Q-switch pulse occurred, thus making sure it opened just before a laser pulse enters the chamber. With this process, a treatment of only three laser shots was the shortest possible. The inertia of the step motor prevented a further reduction. During longer treatments of over 10 laser shots, the shutter was fast enough to achieve a deviation of only one laser shot.

Synchronization with the plasma ignition was achieved by a switchable power amplifier of a COST jet generator. During the treatment, the processing unit would remotely turn on the power amplifier after receiving the Q-switch signal, igniting the plasma. The plasma power of the COST jet had to be set before the measurement because it could not be adjusted within the short treatment times manually. Additionally, turning the plasma on and off within short time frames did not allow the COST jet to reach its equilibrium, resulting in different plasma powers. Thus, the plasma power remained the primary source of uncertainty in reproducibility for the treatment. To reduce this uncertainty, the jet was heated up before the measurement to reach an equilibrium.

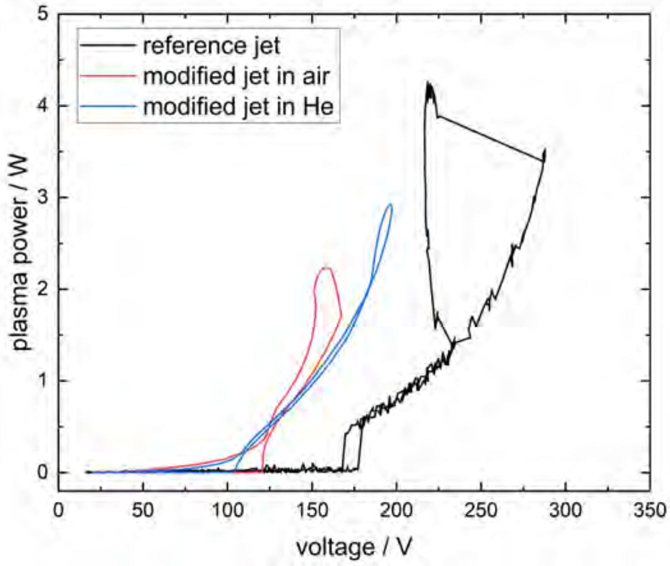

Figure 3.13: Dissipated plasma power for the modified (clay-covered) jet compared to an unmodified version in different atmospheres.

COST jet Ignition in a Helium Atmosphere

A further challenge posed the ignition of the COST jet in the helium atmosphere. As helium is much easier to ignite than air, the helium atmosphere resulted in parasitic discharges mainly around the coil of the jet and between the powered electrode and the housing. To prevent the formation of parasitic discharges, the COST jet's electrode and capacitor were covered in modeling clay (Bostik), and a plastic foil was placed over the housing in front of the coil as an insulator. This prevented the formation of parasitic discharges in a helium atmosphere near atmospheric pressure within the reactor chamber. The clay covering caused a shift from 1420 to 477 in the jet's calibration factor (shown in Tab. **??**) and necessitated a retuning of the capacitor to achieve the best possible coupling of the jet. Although this setup is far from ideal for this application, making further adjustments to the COST jet was outside the scope of this study.

To investigate if the clay covering affected the dissipated plasma power, power curves were measured. The voltage of the power generator was slowly increased while the current and phaseshift were measured by a fast oscilloscope (Lecroy). The COST power monitor program enabled the real-time calculation of the dissipated plasma power. Fig. 3.13 compares the dissipated plasma power depending on the generator voltage U of the modified jet to an unmodified reference jet in an air and helium atmosphere. Ignition for the unmodified jet takes place at around 175 V while the clay-covered jet ignites at 125 V in air and helium. The unmodified jet begins to arc at approx. 300 V and a plasma power of 3.5 W. The clay covering of the jet shifts the ignition voltage towards lower values. In an air atmosphere, the jet ignites at approx. 125 V, while the ignition voltage drops down to 100 V in a helium atmosphere. The plasma powers reached before arcing also differ from the unmodified case. In air, the jet only reaches a power of 2 W. In the helium atmosphere, the jet arcs at about 3 W. For powers over 3 W parasitic discharges ignited within the housing of the jet.

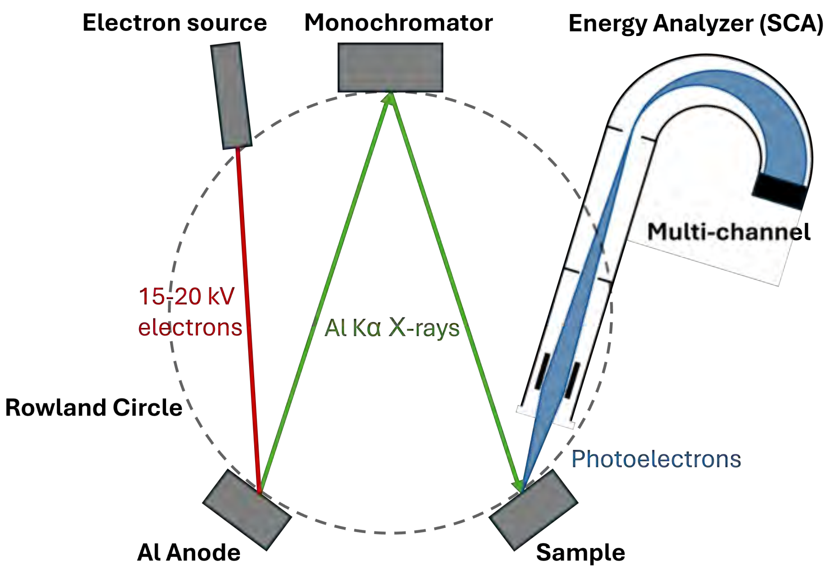

Figure 3.14: Schematic of the XPS device and visualization of the Roland circle.

The modified jet allows an ignition in a helium atmosphere, which proved quite challenging for the unmodified jet. The clay molding was able to prevent the parasitic discharges within operation conditions. However, measuring the plasma power was very challenging. Between measurements, the reference phase shifted noticeably. This necessitated taking a new reference phase before every power measurement. The shift in ignition voltage probably stems from the clay interfering with the voltage and current probes in the jet. It was also observed that the clay covering, especially at the capacitor, showed signs of heating. The clay mass is therefore clearly absorbing some power of the system. From optical emission spectroscopy of the plasma, no change in discharge behavior could be observed, except for influencing the measurements from the probes between the modified and unmodified jet. It is therefore believed that the clay coverage did not alter the discharge conditions, even though the power curves deviate from those of the unmodified jet.

As already mentioned, during treatment, the jet is turned on and off within short time frames, which further complicates plasma power measurement. The plasma system must first reach an equilibrium, which can take up to an hour. Before measurements, the jet was therefore always heated up over longer time frames to prevent these instabilities. Nonetheless, the experimental conditions often did not allow for these measures.

3.4 XPS Device

To study the effects of the laser-plasma treatment, the chemical surface conditions had to be investigated. The stoichiometry analysis of treated substrates was conducted with the XPS device ULVAC-PHI Inc. "PHI 5000 VersaProbe". Fig. 3.14 shows the schematic for its most important components. The electron source generates electrons from a lanthanum filament. From there, the electrons are focused and accelerated towards an Al anode. Due to bremsstrahlung, X-rays are produced from the anode and directed at the monochromator. It is a (100) crystal monochromator that filters the $K_{\alpha3,4}$, $K_{\alpha5,6}$ and K_{beta} emission lines and the Al bremsstrahlung background, according to the Rowland circle method. This leaves only the $K_{\alpha1,2}$ line at 1486.6 eV which is narrowed to 0.26 eV FWHM. From the monochromator, the emission hits the sample, inducing the ejection of photoelectrons. These electrons are then gathered by the input lens of the hemispherical capacitor analyzer and analyzed with regard to their energy. The observed spot size on the sample can be varied up to 200 µm. The multi-channel measures the kinetic energy of the collected electrons. The employed XPS device and substrate material of copper result in an observation depth of $d = 3.92\,\mathrm{nm}$.

4 Results & Discussion

With the experimental setups established, this chapter presents the results obtained using the described methods. The reactive molecular oxygen species measurements are covered first, as they are crucial in optimizing a combined surface treatment for the CuO formation. After that, the morphology analysis of the copper samples is detailed, followed by their chemical analysis. Lastly, results of a fs-laser treatment are shown, which provide an outlook for further refinement of the synthesis process of copper catalysts.

4.1 Reactive Oxygen Species

The following results were produced with the help of Robin Minke during his Bachelor thesis, who performed the preliminary measurements and built the setup for the species diagnostics. Furthermore, the data of the theoretical models were provided by projects A4, Youfan He, and A9, Máté Vass, within the CRC 1316. The results presented here are part of a collaborative paper [111].

One aim of this thesis is to deepen the understanding of oxygen–species reaction kinetics in the COST jet by supplying new experimental data for the hard-to-measure states $O_2(a^1\Delta_g)$ and $O_2(b^1\Sigma_g^+)$, the first and second electronically excited levels of molecular oxygen. The knowledge about their density and fluxes also plays a crucial role in understanding the formation of copper oxides. Because both states are efficiently quenched by ozone, accurate knowledge of the ozone density is essential for determining their absolute concentrations. The densities of the reactive oxygen species were investigated using optical spectroscopy. Emission spectroscopy for the molecular oxygen species $O_2(a^1\Delta_g)$ and $O_2(b^1\Sigma_g^+)$, and absorption spectroscopy for ozone, was employed. The measurements for ozone and $O_2(a^1\Delta_g)$ are performed using a flow cell setup to compensate for the weak emission or absorption of the species.

They are benchmarked against two complementary models: (i) a pseudo-1D plug-flow simulation, used to validate the experimental values and to analyse reaction pathways, and (ii) a 2D fluid simulation, employed to capture the spatially resolved interplay between gas flow, temperature, and species transport inside the flow cell. While the plug-flow model neglects the inherently two-dimensional distribution of species in the cell, the fluid model resolves these gradients, but at a considerably higher computational cost, making extensive parameter variations less practical. A validation of the models by the experimental data would allow to extrapolate the spatial resolution of the species densities to different setups geometries, circumventing the rather limited information gained about spatial distribution provided by the optical diagnostic. This information enables the optimization of the plasma parameters towards a controlled copper oxide formation.

4.1.1 Chemical Models

Given the complexity of plasma-chemical interactions, modeling serves as a powerful tool for analyzing species interactions and estimating species densities, particularly when experimental quantification is difficult. Zero-dimensional (0D) models offer a good compromise between computational efficiency and accuracy, especially for simple gas mixtures such as He/N_2 or He/O_2 [112–126]. These models can be used to investigate the effects of different parameters, such as gas temperature, mixing ratios, and plasma power, on plasma behavior and the generation of reactive species.

For plasma jets, the extension of these models to plug flow simulations [114, 116, 120–122] enables spatially resolved analysis of species evolution along the gas flow. This approach also allows the modeling of time-dependent effects [105], thereby improving the physical realism of the simulations. The pseudo-1D plug flow model employed in this study was provided by the project A4 within the CRC 1316 by Youfan He.

The distribution of reactive species within the gas flow cell can affect the measured densities considerably. However, the commonly used pseudo-one-dimensional (1D) plug flow model does not provide the spatial behavior of species inside the cell, which is inherently two-dimensional. To address this, a 2D fluid simulation provided by Máté Vass from project A9 was employed. This approach provides spatio-temporally resolved species densities and also offers information on flow velocity and gas temperature. While the 2D simulation yields more detailed insights, it is computationally more demanding, making comprehensive parameter scans time-intensive. In many practical cases, a rough approximation of the species densities is sufficient, for which the simpler pseudo-1D plug flow model remains adequate.

The two simulations presented below employ a nearly identical chemical kinetics scheme, resulting in comparable predictions for the distribution of reactive species within the plasma chamber. Only simplified wall interactions were considered for the reactive species, and in the case of ozone, wall reactions were entirely neglected. Additionally, the used wall reaction rates were optimized explicitly for the plasma zone of the COST jet and the flow cell. A detailed investigation of accurate wall rate coefficients for the various species was beyond the scope of this study.

Pseudo-1D Plug Flow Model

In this study, a pseudo-one-dimensional (pseudo-1D) plug flow model is employed to determine the spatial profiles of species densities along the direction of gas flow within the jet chamber [127, 128]. The model solves the particle balance equations and the electron energy balance equation from a zero-dimensional simulation to yield time-dependent species densities and an effective electron temperature within an infinitesimally small plug volume. This volume moves with the gas flow, allowing the conversion of temporal evolution into spatial profiles by utilizing the gas velocity.

The gas temperature in the jet chamber is varied in the simulation as a function of the absorbed power, following equation (1) from [127]. The gas temperatures at the feed inlet and in both downstream regions (i.e., the 17.5 mm long tube and the 79 mm long gas flow cell shown in Fig. 3.1) are assumed to be 300 K. The pressure is uniformly set to $1 \cdot 10^5$ Pa in all regions.

The plug flow calculations in the two effluent regions follow a similar approach to that in the jet chamber. Still, they are adapted to account for differences in geometry and power input. Specifically, the rectangular cross-sectional area of the jet chamber ($1 \cdot 1\,\mathrm{mm}^2$) is smaller than the cylindrical inlet tube ($1 \cdot 1\,\pi\,\mathrm{mm}^2$ and $7 \cdot 7\,\pi\,\mathrm{mm}^2$) of the flow cell. Accordingly, flow velocities in the effluent regions are calculated by substituting the appropriate gas temperature, pressure, and cross-sectional area values into equation (5) from [128]. As a result, the gas flow velocity in the jet chamber is higher than in either effluent region. For instance, at 1 slm He with 0.5 % O_2 admixture, flow velocities in the 30 mm long jet chamber, the 17.5 mm entry tube, and the 79 mm gas flow cell, are estimated to be approximately $1882\,\mathrm{cm\,s^{-1}}$, $533\,\mathrm{cm\,s^{-1}}$, and $11\,\mathrm{cm\,s^{-1}}$, respectively. The velocity used in the plug flow model for the jet chamber aligns well with the result from the fluid model (Fig. 4.1), whereas velocities in the effluent regions tend to be underestimated compared to the fluid simulation. In the case of the 79 mm gas flow cell, this underestimation is likely due to the plug flow model's assumption of an axial gas flow direction consistent with the jet and tube, which contrasts with the more realistic perpendicular flow observed in the fluid model and depicted in the experimental setup (Fig. 3.1).

Wall reaction rates for neutral species are determined by adjusting the effective diffusion length [129], volume, and surface area to those relevant for each effluent region. Moreover, in the simulations for the effluent zones, the electron energy balance equation (i.e., equation (9) in [128]) is omitted due to the lack of power deposition and the correspondingly negligible influence of electron density. Therefore, only particle balance equations are solved in these regions.

The electron energy distribution functions (EEDFs) are calculated using a Boltzmann solver based on the steady-state solution of the Boltzmann equation under the two-term approximation. Specifically, the open-source simulation tool Lisbon Kinetics Boltzmann (LoKI-B) by Tejero-del-Caz *et al.* [130] is used to compute EEDFs over a range of reduced electric fields.

The plasma chemistry set used in this work is identical to that described in [127], which lists all species and reactions involved. The modeled species include He, $He(2^3S)$, He_2^*, He^+, He_2^+, $O(^3P)$, $O_2(v=0)$, O_3, $O(^1D)$, $O_2(a^1\Delta_g)$, O^+, O_2^+, O_4^+, O^-, O_2^-, O_3^-, O_4^-, e^-, and $O_2(b^1\Sigma_{g+})$. It is worth noting that the simulated $O(^3P)$ densities in He/O_2 plasma jets, as reported in [127], are in good agreement with experimental measurements from various studies under different power, flow, and mixture conditions [54].

Fluid Model

The two-dimensional spatially resolved simulation in this study is performed using *non-PDPSIM*, a fluid-based plasma modeling code [131, 132]. This code solves the continuity equations for charged and neutral species under the drift-diffusion approximation, along with the compressible Navier-Stokes equations to obtain species densities, velocity fields, and gas temperature distributions on an unstructured triangular mesh. The plasma model includes electrons (e^-), positive ions (O_2^+, O^+, He^+), and negative ions (O^-, O_2^-, O_3^-). The considered neutral species are He, O_2, O, O_3, $O_2(v{=}1\text{–}4)$ (first four vibrational states of O_2), $O_3(v)$, $O_2(a^1\Delta_g)$, $O_2(b^1\Sigma_g^+)$, $O(^1D)$, and He^* (representing a combination of $He(2^3S)$ and $He(2^1S)$). Transport coefficients for heavy species are computed assuming thermal equilibrium with the local gas temperature. Electron transport parameters (mobility and diffusivity) are derived using a two-term Boltzmann solver. The simulation uses the local mean energy approximation, solving the electron energy balance accordingly. The chemical reaction set and electron impact cross sections used in the Boltzmann solver are taken from [133]. Although the reaction scheme differs slightly from that used in the plug flow model, both have been independently validated for COST jet conditions. Given the objective of comparing with experimental data, the use of different yet credible chemistry sets is deemed appropriate.

The mesh resolution is adapted to the characteristic physical scales of the different regions. Within the jet, grid spacing is $3 \cdot 10^{-5}$ m in the y-direction (between the electrodes) and $7 \cdot 10^{-4}$ m along the x-direction, owing to stronger gradients across the electrode gap. In the connecting tube between the jet and flow cell, the grid spacing is $2 \cdot 10^{-4}$ m, and in the flow cell itself, the resolution is coarsened to $7 \cdot 10^{-4}$ m, as the expected gradients are smaller.

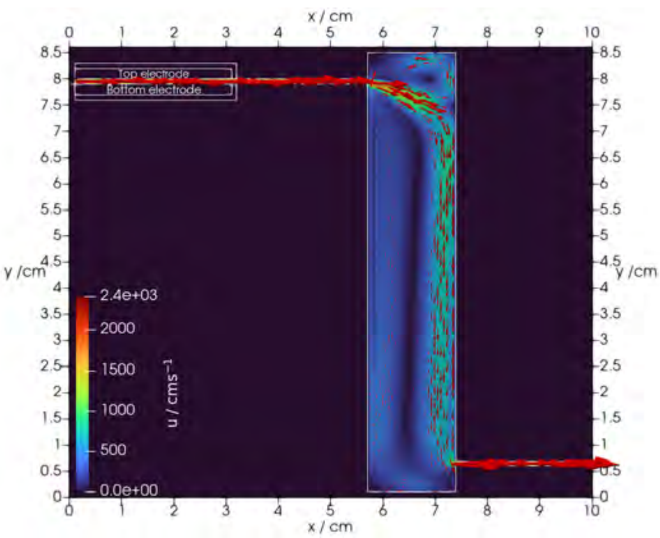

Figure 4.1: Computational domain and spatial distribution for the gas velocity at 1 slm He flow. The color bar shows the gas velocity, while the red arrows indicate the gas flow direction.

Fig. 4.1 shows the simulation domain together with the steady-state gas velocity distribution for a helium inflow of 1 slm. Neutral species generated in the COST jet (with the top electrode powered and the bottom electrode grounded) flow through a 2 mm gap-length tube into the flow cell. The computational geometry matches the dimensions of the experimental system. As illustrated in the Fig. 4.1, the gas flow in the cell is spatially non-uniform. Due to the change in gap length between the electrode region and the connecting tube, the gas velocity drops by a factor of 2 (as this is a 2D simulation). Upon entering the flow cell, the gas velocity decreases further, and two vortices form near the inlet.

The simulations were carried out for a total physical time of 0.2 s for the neutral species and flow fields, while plasma quantities were resolved over 30 μs using a time-slicing strategy [132]. This corresponds to approximately 10 flow-through times for the domain, which is sufficient for capturing convective transport. However, complete diffusive equilibration, especially for stable species like ozone, would require considerably longer timescales (on the order of seconds) due to slower mixing processes. Most species, including ions and short-lived neutrals, reach near-convergence within the simulated time. Long-lived species such as ozone, and to a lesser extent $O_2(a^1\Delta_g)$, which interacts with ozone, exhibit some continued evolution. Based on the convergence behavior, the uncertainty in their volume-averaged densities at the end of the simulation is estimated to be around 10–15%. Although the model is not fully converged in the flow cell region, the results capture the dominant spatial trends and absolute levels necessary for a meaningful comparison with experimental data.

4.1.2 Flow Cell Equilibrium

It is well known that APPJstake time to reach an equilibrium state. In this timeframe, species densities can change considerably due to heating for example. In the case of the flow cell. This dependence is even further enhanced by the diffusion-driven processes. To obtain reliable experimental data, it is therefore crucial to understand the key parameters that influence measured species densities. When experimentally measuring the signals of $O_2(a^1\Delta_g)$ and ozone, it was observed that the signal takes a few minutes to stabilize. When considering the gas flow of 1 slm and the volume of the flow cell of 12 ml, the flow cell should be filled after only a few milliseconds. Therefore, diffusion and other processes play a critical role here, as was already alluded to in the 2D fluid simulation. To assess the signal stability of the optical measurements, the respective signal was monitored over a period of time. The gas flow cell was previously flushed with a helium flow with an admixture of He + 0.5 % O_2 to clean the flow cell of any impurities.

Fig. 4.2 depicts the ozone density after plasma ignition for the following 250 s for a plasma power of 1 W, a flow of 1 slm He, and an admixture of 0.5% oxygen. The ozone density increases until approximately 100 s and then reaches a plateau. This behavior can be understood as the flow cell filling up with the products of the COST jet effluent, causing the ozone density to rise. The initial buildup is relatively fast, but slows down after the

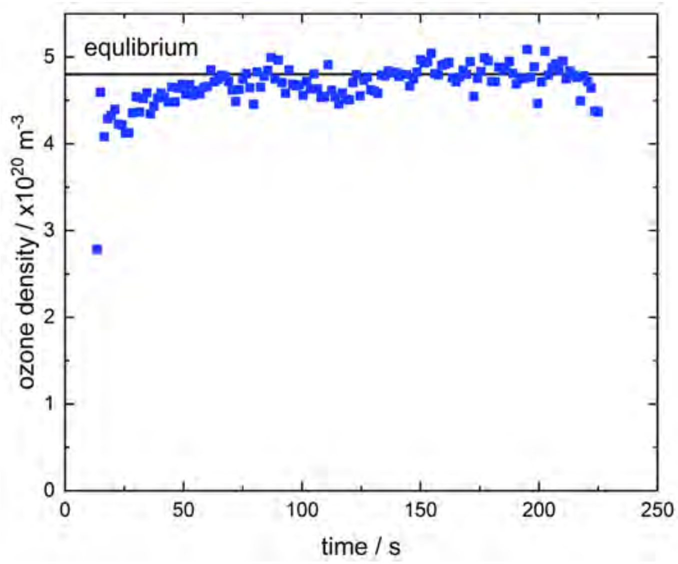

Figure 4.2: Evolution of the ozone density over 250 s for 1 W plasma power, 1 slm flow and 0.5% oxygen admixture.

first 25 s. The time it takes to reach an equilibrium is far higher than expected if the flow cell just had to be filled with the content of the effluent. This can be explained by the 2D fluid simulation. As shown in Fig. 4.1, due to the vortex flow inside the cell, the equilibrium state is mostly determined by the diffusion of species instead of the gas convection. The time scales are therefore much longer than expected.

A similar behavior can be observed for the $O_2(a^1\Delta_g)$ emission signal. Fig. 4.3 shows the spectrometer signal of the $O_2(a^1\Delta_g)$ emission signal over a time of 500 s after plasma ignition. Initially, the signal rises rapidly and reaches a maximum after 30 s. From there, it decreases slowly until 200 s. The initial rise is due to filling the flow cell with the effluent from the COST jet. The slight decrease until 200 s can be explained by the increasing ozone density in the first 50 s. The higher ozone density quenches $O_2(a^1\Delta_g)$ stronger, reducing its density until an equilibrium is reached.

A further influence on the measured densities within the flow cell can be observed when varying the discharge conditions, such as power. Fig. 4.4 shows the evolution of the $O_2(a^1\Delta_g)$ intensity over time after changing the plasma power from 1 W to 0.2 W and 1 W to 1.6 W, respectively. Here, the discharge was left running at 1 W until the signal stabilized. Then, the discharge was switched off, and the flow cell was briefly flooded with the helium and oxygen admixture. After that, the jet was reignited with either a higher or lower plasma power, and the measurement was started. This procedure was chosen to start the measurement at different temperatures induced by the discharge.

After plasma ignition, a fast increase in the $O_2(a^1\Delta_g)$ emission intensity can be observed, as shown in Fig. 4.3. However, instead of reaching an equilibrium state after approximately 100 s, the emission intensity changes further for both powers. At 0.2 W the intensity continues to rise even after 750 s while it decreases for 1.6 W. These long-term changes in the system's equilibrium state are likely caused by temperature variations. After the

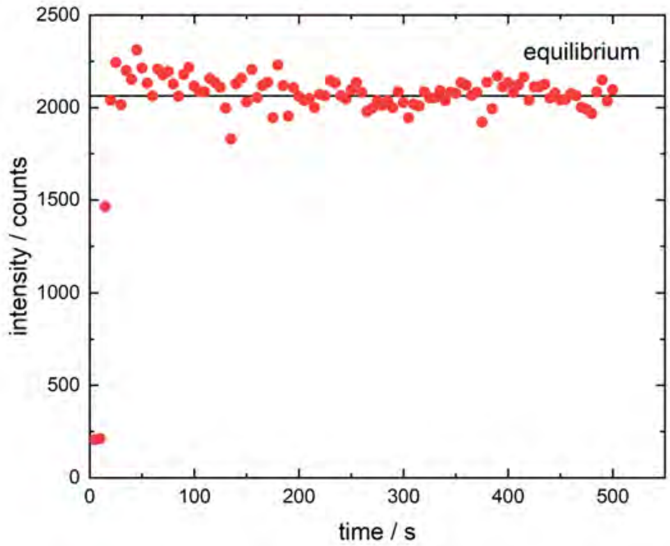

Figure 4.3: Evolution of the $O_2(a^1\Delta_g)$ signal over 500s for 1 W plasma power, 1 slm flow and 5% oxygen admixture.

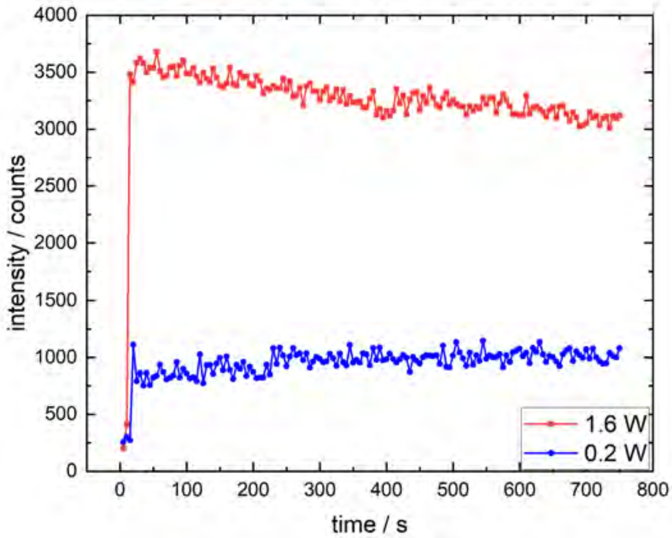

Figure 4.4: $O_2(a^1\Delta_g)$ signal over 750 s after changing the plasma power from 1 W to 0.2 W and 1.6 W. The flow of 1 slm and admixture of 5% oxygen stayed constant.

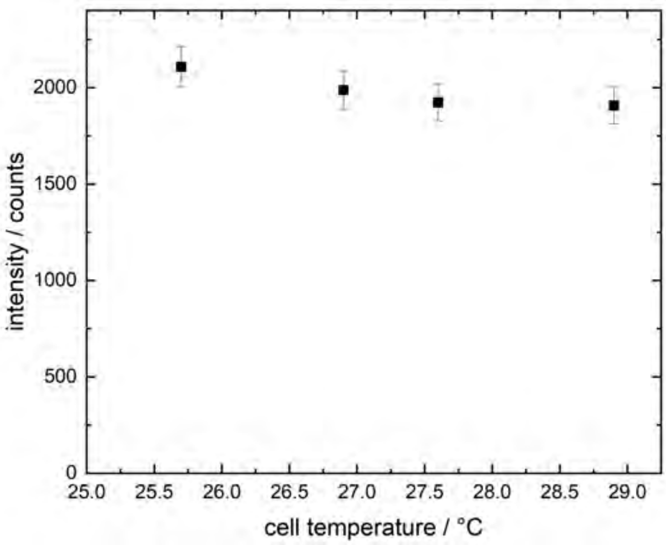

Figure 4.5: $O_2(a^1\Delta_g)$ signal evolution after temperature decrease for 1 W plasma power, 1 slm flow and 5% oxygen admixture.

decrease in power for the 0.2 W from 1 W, the temperature in the flow cell decreases. This in turn leads to an increase in the $O_2(a^1\Delta_g)$ intensity. The opposite is happening for the 1.6 W plasma power increase from 1 W plasma power. Here, the temperature rises due to the increased plasma power, which decreases the $O_2(a^1\Delta_g)$ density. Therefore, it can be concluded that the temperature of the flow cell seems to impact the equilibrium state of the $O_2(a^1\Delta_g)$ density. Although not shown here, ozone is also known to be sensitive to temperature changes [134, 135].

To measure the influence of the flow cell temperature on the $O_2(a^1\Delta_g)$ signal, thermocouple elements were fixed to the jet and the front of the flow cell close to the jet. The cell was heated beforehand by applying a high plasma power, as the flow cell setup did not provide a means to heat the cell separately. After reaching a temperature of 40 °C, the plasma was turned off, and the cell was flushed with a flow of 1 slm and an admixture of 0.5 % oxygen for 1 min. Afterwards, the plasma was ignited again, and the temperature was measured every minute, and a spectrum of the $O_2(a^1\Delta_g)$ signal was taken. Fig. 4.5 shows the evolution of the $O_2(a^1\Delta_g)$ emission signal for a declining flow cell temperature while plasma power, flow, and admixture were kept constant at 1 W plasma power, 1 slm flow, and 5% oxygen admixture. It can be seen that the signal intensity increases slightly while the temperature decreases. The temperature did not noticeably decrease after reaching 25.7 °C. Therefore, it can be concluded that higher temperatures lead to a lower intensity of the emission signal and consequently a smaller $O_2(a^1\Delta_g)$ density. Before taking measurements, it is crucial to wait long enough for the system to reach an equilibrium state. This way, uncertainties in the density measurements can be reduced.

4.1.3 Ozone Density

The 2D-fluid simulation provides an initial insight into gas dynamics within the flow cell, while the preliminary measurements have identified crucial control parameters. With this

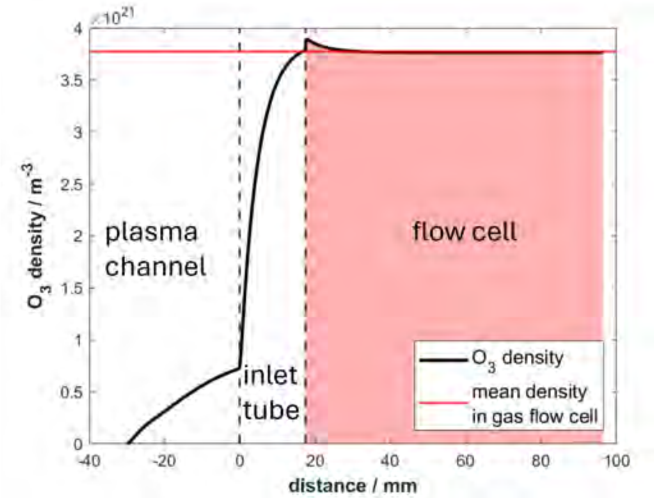

Figure 4.6: O_3 density calculated by the plug-flow model along the gas flow direction inside and outside the COST jet. The averaged density in the gas flow cell volume is shown as a red line. Dashed lines indicate the transition from the jet (left) to the inlet tube (middle) and to the flow cell (right). An effluent temperature of 300 K, a power of 1 W, a 1 slm He flow, and a 0.5% oxygen admixture are assumed.

knowledge, the ozone density can be investigated in the flow cell setup. Its density was studied under varying power, flow rate, and O_2 admixture conditions and compared to the plug flow simulation and the 2D fluid simulation densities.

Pseudo-1D Plug Flow Simulation Density

Fig. 4.6 presents the ozone density predicted by the plug flow model along the gas flow direction, with $x = 0\,\mathrm{m}$ marking the end of the jet electrodes. Within the plasma channel, the ozone density increases asymptotically, reaching its maximum at the jet nozzle. Along the jet, molecular oxygen is dissociated into atomic oxygen, which subsequently reacts with O_2 to form ozone, one of the dominant production mechanisms. With increasing dissociation along the jet, more atomic oxygen becomes available for ozone formation [54]. The production eventually balances with ozone consumption via reactions with $O_2(b^1\Sigma_g^+)$. However, at a flow rate of 1 slm, the residence time within the plasma region is too short to reach equilibrium.

In the inlet tube leading to the gas cell, the ozone density continues to rise due to the three-body recombination reaction Eq.(2.24) $O + O_2 + He \leftrightarrow O_3 + He$. The rapid increase in the ozone density after the jet-to-tube transition arises from the reduced gas velocity in the inlet tube. The slower flow results in longer residence times for the same path length, thereby “squeezing” ozone’s formation into a shorter distance. This seemingly enhances the ozone formation. Moreover, ozone destruction pathways, such as reactions with $O_2(b^1\Sigma_g^+)$, are less pronounced in the effluent region.

Upon entering the flow cell, the gas velocity decreases drastically, considerably increasing the residence time. This causes a sharp rise in ozone density, as it’s effluent production from atomic oxygen is squeezed into a shorter timeframe. The same is true for the remain-

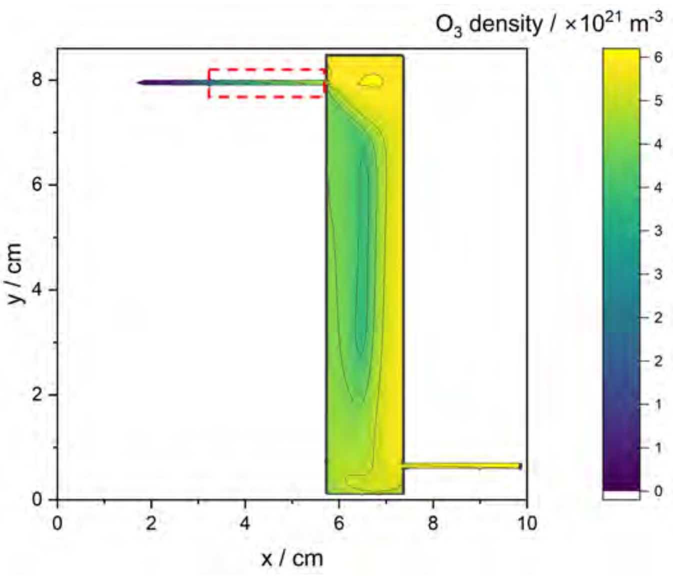

Figure 4.7: O_3 density distribution inside the gas flow cell simulated with the fluid model for an effluent temperature of 300 K, power of 1 W, a 1 slm He flow, and a 0.5 % oxygen admixture. The red dotted area indicates the inlet tube downstream of the COST jet channel.

ing $O_2(b^1\Sigma_g^+)$, which leads to the destruction of ozone. After the decrease in $O_2(b^1\Sigma_g^+)$, destruction reactions have only a minor impact and ozone has a long lifetime, the density remains nearly constant in the flow cell. The plasma chemistry, therefore, converges towards longer-lived species such as ozone and molecular oxygen. The ozone density in the flow cell is averaged along the flow direction, as illustrated in Fig. 4.6. The averaged value is then compared to the experimental data.

2D Fluid Simulation Density

Fig. 4.7 displays the two-dimensional ozone density distribution in the gas flow cell obtained from the 2D fluid model. The effluent enters a tube that connects vertically to the flow cell, as described in the setup section. Consistent with the plug flow simulation, the ozone density increases considerably outside the plasma zone, particularly within the flow cell. Inside the cell, the flow circulates in a vortex along the walls, producing the highest densities near the outer edges of the cell. In contrast, along the central axis, the density is lower due to the vortex dynamics. Moreover, the recess at the entrance, where the optical window is located, also induces a vortex, leading to locally elevated densities compared to the rest of the volume. The inhomogeneous ozone distribution is a result of the relatively short simulation time (≈ 0.2 s). With longer simulation times, the modeled densities of long-lived oxygen species such as ozone would be expected to approach a more homogeneous distribution throughout the cell. This is mainly due to diffusion: with a diffusion coefficient of ozone in helium of $D_{O_3} = 7.13 \cdot 10^{-5}$ m^2/s [18], the homogenization timescale is on the order of seconds. Extending the simulation time sufficiently, however, proved to be computationally too demanding and was therefore beyond the scope of this study.

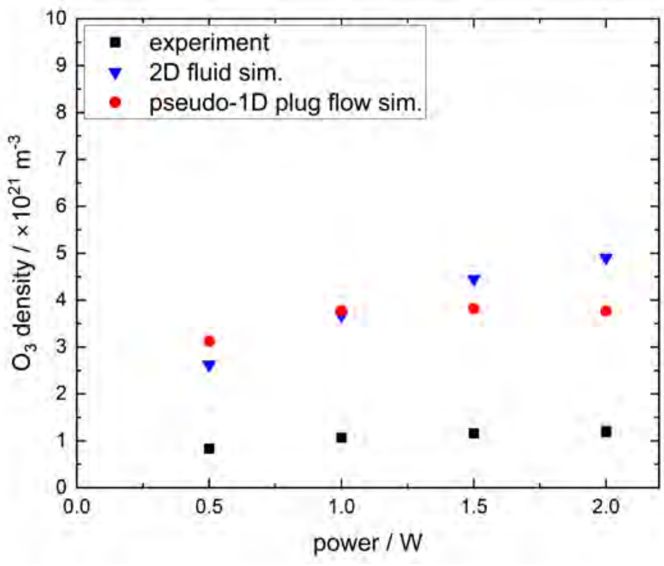

Figure 4.8: O_3 density comparison between simulation and experiment for an effluent temperature of 300 K, a 1 slm He flow, and a 0.5 % oxygen admixture as a function of plasma power.

Comparison of Experimental to Simulated Densities

For a given set of plasma parameters, an ozone absorption spectrum was recorded every minute for 5 to 10 minutes until an equilibrium intensity was reached. From the recorded spectra, the average intensity in the equilibrium was calculated by Lambert-Beer's Law. Due to the small uncertainty, most error bars of the experimental data are not visible within the graphs. The measurements were compared with simulation results from both the pseudo-1D plug flow model and the 2D fluid model.

Fig. 4.8 presents the averaged ozone density as a function of plasma power for a helium flow of 1 slm and an oxygen admixture of 0.5 %. The value for a measurement was averaged over five absorption spectra within a measurement time of 5 min. The uncertainty of the ozone density measurements was calculated based on the equilibrated ozone density from multiple measurements. For a given set of plasma parameters and a controlled temperature, the uncertainty resulted in approx. 2%. The ozone density was therefore very reproducible. It should, however, be noted that the UV lamp exhibited intensity variations of up to 650 counts. For low oxygen admixtures, this could result in an uncertainty of up to 10% because of the low absorption signal. Higher admixtures were not affected by this.

Both experimental and simulated results show a steady increase in ozone density with increasing plasma power. Higher plasma power enhances the dissociation of molecular oxygen, thereby increasing the density of atomic oxygen. This, in turn, raises ozone formation through recombination with molecular oxygen. The experimental data reveal an approximately linear increase of ozone density with power, a trend also reproduced by the 2D fluid model, though with a steeper slope than the experiment. While the two simulations agree closely with each other, their predicted values are roughly three times higher than the experimental results, but still within the same order of magnitude. The plug flow model shows a more asymptotic rise, reaching a plateau at 1 W, where ozone production is

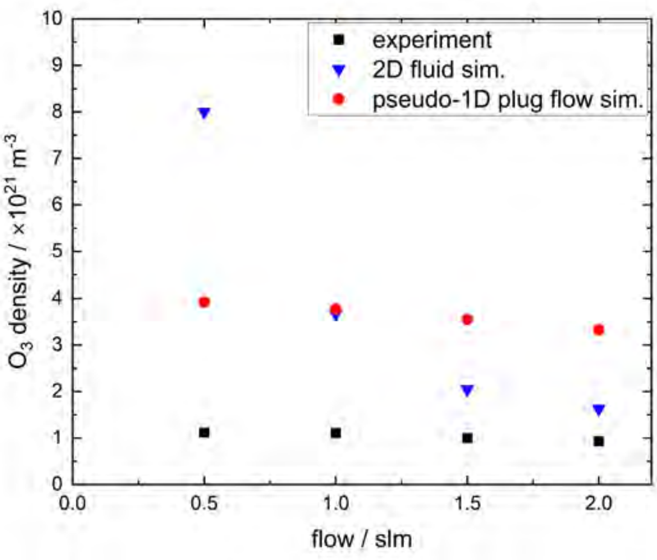

Figure 4.9: O_3 density comparison between simulation and experiment for an effluent temperature of 300 K, a plasma power of 1 W, and a 0.5 % oxygen admixture as a function of helium flow.

likely balanced by reactions with $O_2(b^1\Sigma_g^+)$, preventing further growth. The consistency between the two simulations supports the assumption that the volume-averaged ozone density in the plug flow model is reliable, provided that ozone is distributed homogeneously in the flow cell. The discrepancy with experimental data could stem from neglected processes, such as ozone wall losses, or from a general overestimation of production in the simulations. Additionally, small deviations in the actual effluent temperature from the assumed 300 K could also contribute to the experimentally observed lower ozone densities.

The effect of gas flow velocity on ozone density is illustrated in Fig. 4.9. Both, experiment and simulations, confirm that the ozone density is highest at low flow rates and decreases with increasing flow velocity. This behavior results from the longer residence time in the plasma zone at lower flows. Since ozone is primarily formed through the three-body reaction of atomic oxygen with molecular oxygen, longer residence times enhance the dissociation of oxygen, thereby increasing the atomic oxygen density and, consequently, ozone production. Both the experimental data and the plug flow simulation show an almost linear decrease with gas velocity, with very similar slopes. In contrast, the 2D fluid simulation predicts a more asymptotic decrease. This discrepancy can be attributed to the limited simulation time, which does not allow the fluid model to reach a homogeneous ozone distribution in the flow cell (see Fig. 4.7). At low flows, the time required for equilibrium is significantly longer, resulting in substantial deviations from the experiment, whereas at higher flows, equilibrium is reached more quickly, and the deviation is smaller. As with the power variation results, the simulations generally overestimate ozone density, though at high flows, the 2D fluid model comes very close to the experimental values as the distribution becomes more uniform. With longer computational times, the 2D fluid simulation would likely provide a more accurate match to the measured densities.

Fig. 4.10 (a) illustrates the ozone density as a function of oxygen admixture. Both simulations and experimental data show that the ozone density increases with higher

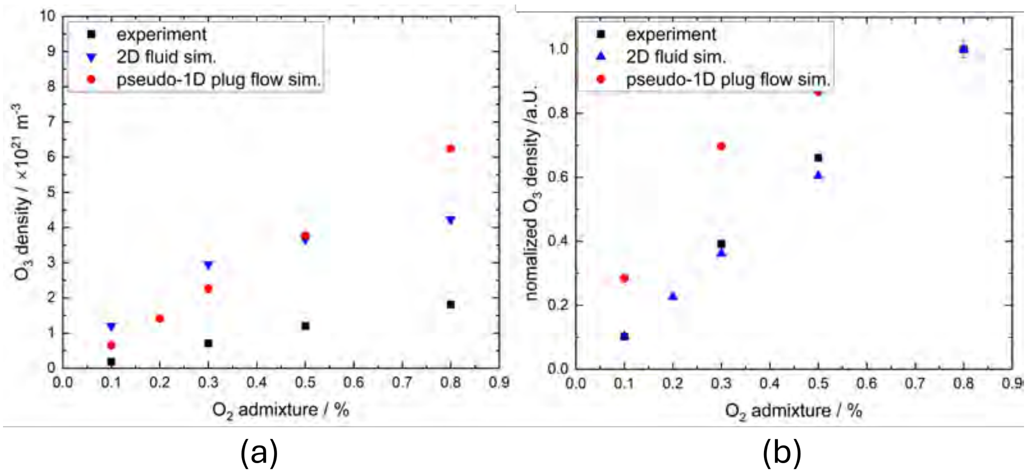

Figure 4.10: (a) O_3 density comparison between simulation and experiment for an effluent temperature of 300 K, a plasma power of 1 W, and a helium flow of 1 slm as a function of oxygen admixture. (b) shows the normalized O_3 density for the same data

oxygen admixture. Since ozone is formed through the recombination of atomic oxygen with molecular oxygen, this behavior is expected. The COST jet is known to produce atomic oxygen most efficiently at an admixture of about 0.5 % oxygen in helium [54]. Accordingly, one might expect the ozone density to peak near this value. However, the ozone density continues to rise slightly with increasing admixture, since more molecular oxygen is available for reactions with atomic oxygen. At very low admixtures, the atomic oxygen density is limited because only small amounts of molecular oxygen are available for dissociation. At higher admixtures, the atomic oxygen density decreases again, as dissociation becomes less efficient and recombination to ozone occurs more rapidly.

For low admixtures, both simulations accurately reproduce the experimental results. At higher admixtures, however, they overestimate the ozone density. Among the two models, the 2D fluid simulation shows a more asymptotic increase and better reflects the experimental trend. In contrast, the plug flow model predicts an almost linear increase, resulting in larger deviations from the measured values at higher admixtures. This suggests that gas dynamics and the resulting inhomogeneous species distribution play a more important role at higher oxygen admixtures, while at lower admixtures the agreement is generally better. With a longer computation time, it may also achieve improved agreement in the flow variation case, as higher flows have already shown better consistency with experimental results.

Overall, both models capture the correct order of magnitude, though they overestimate the ozone density by approximately a factor of three. Fig. 4.10 (b) shows the normalized ozone densities for the two simulations and the experimental results to their respective maxima. It can be seen that the 2D fluid simulation reproduces the dependence on the admixture observed in the experiment very well, as it exhibits a slope very similar to that of the experimental results. The plug flow simulation successfully captured the trends in power and flow variations, but represents the admixture dependence less accurately, as described in the previous sections.

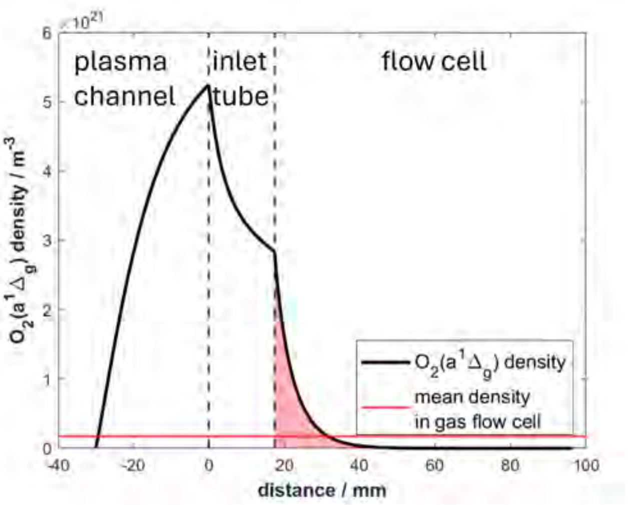

Figure 4.11: $O_2(a^1\Delta_g)$ density calculated by the plug flow model along the jet and effluent in the gas flow cell. Dashed lines indicate the transition from the jet (left) to the inlet tube (middle) and to the flow cell (right). The averaged density for the gas flow cell volume is shown as a red line. Parameters: effluent temperature 300 K, plasma power 1 W, helium flow 1 slm, and 0.5 % oxygen admixture.

When comparing the experimental ozone densities with those reported in other studies, the values obtained here are in good agreement. For example, Harris et al. [136] investigated ozone generation in the effluent of a different RF APPJ using helium with up to 1 % oxygen admixture and found ozone densities of approximately $1 \cdot 10^{21}\,\mathrm{m}^{-3}$, which is very close to the experimental results of the present work.

4.1.4 $O_2(a^1\Delta_g)$ Density

Knowledge of the ozone density allows the determination of its quenching effect on the excited molecular oxygen species $O_2(a^1\Delta_g)$ and $O_2(b^1\Sigma_g^+)$. With this, their densities can be calculated. The experimentally determined $O_2(a^1\Delta_g)$ density was compared to the plug flow simulation and the 2D fluid simulation in the same manner as for ozone.

Pseudo-1D Plug Flow Density

The simulated $O_2(a^1\Delta_g)$ density for the plug flow model is presented in Fig. 4.11. Within the discharge region, the $O_2(a^1\Delta_g)$ density rises asymptotically towards the jet exit. The gas then transitions into the wider inlet tube ($d = 2\,\mathrm{mm}$) before entering the flow cell, as marked by the dashed lines. In the effluent, $O_2(a^1\Delta_g)$ decays exponentially due to reactions with other species. This behavior is consistent with observations for other species, such as atomic oxygen [54]. Upon entering the flow cell, the decay rate with respect to distance increases because the larger cross-section reduces the gas velocity, leading to faster decay over the same spatial length.

For comparison with the experimental data, the plug flow model densities were averaged along the flow direction after the inlet tube, as indicated by the red region in Fig. 4.11. While $O_2(a^1\Delta_g)$ is not distributed homogeneously throughout the flow cell, this averaging

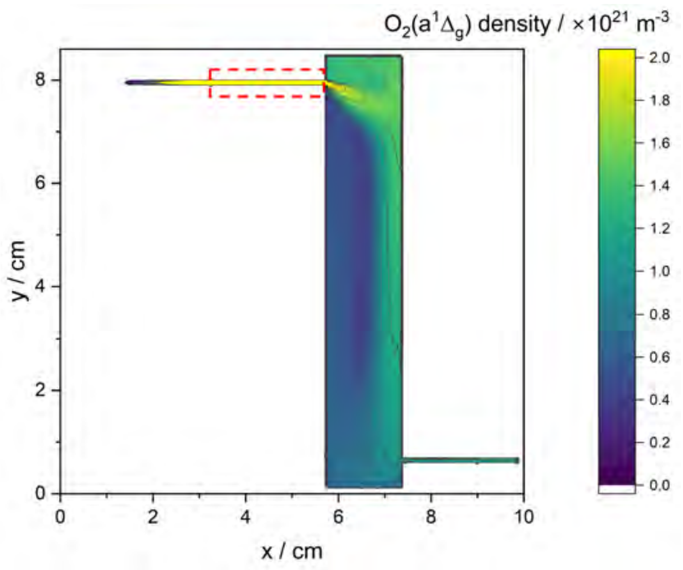

Figure 4.12: Two-dimensional $O_2(a^1\Delta_g)$ density distribution in the gas flow cell volume calculated by the 2D fluid simulation of the COST jet for effluent temperature of 300 K, plasma power of 1 W, helium flow of 1 slm, and a 0.5 % oxygen admixture. The red dotted area indicates the inlet tube downstream of the COST jet channel.

approach still provides a reasonably good agreement between the plug flow model and the experimental measurements, as will be shown later.

2D Fluid Simulation Density

Fig. 4.12 depicts the $O_2(a^1\Delta_g)$ distribution inside the flow cell geometry. The density decreases along the entrance tube before reaching the cell. In the flow cell, the density decrease is even steeper due to the slower gas flow velocity. Similar to ozone, the $O_2(a^1\Delta_g)$ density is slightly higher along the flow cell wall opposite the entrance tube compared to the entrance side, with a relative minimum in the central region of the cell. The decrease in density follows the flow vortex inside the cell, highlighting the missing diffusion that a longer simulation time would provide. This results in a more inhomogeneous distribution compared to ozone. At the entrance of the flow cell, the density is approximately $2.4 \cdot 10^{21}$ m^{-3}, which compares well with the plug flow prediction of about $3.0 \cdot 10^{21}$ m^{-3}. By the time the gas exits the flow cell, the density is nearly halved to $1.3 \cdot 10^{21}$ m^{-3}, which is considerably higher than predicted by the plug flow model, largely due to the slower gas velocity in the plug flow simulation. For comparison with the experiment, the density was averaged over the entire gas flow cell volume in the same way as for ozone.

Comparison of Experimental to Simulated Densities

The $O_2(a^1\Delta_g)$ density generated by the COST jet was investigated by varying the plasma power, gas flow, and oxygen admixture. After setting the plasma parameters and igniting the plasma, an $O_2(a^1\Delta_g)$ spectrum was taken every minute for 5 to 10 min until an equilibrium intensity was reached. Then the average intensity of the equilibrated spectra was calculated. This could then be converted to an $O_2(a^1\Delta_g)$ density with the energy

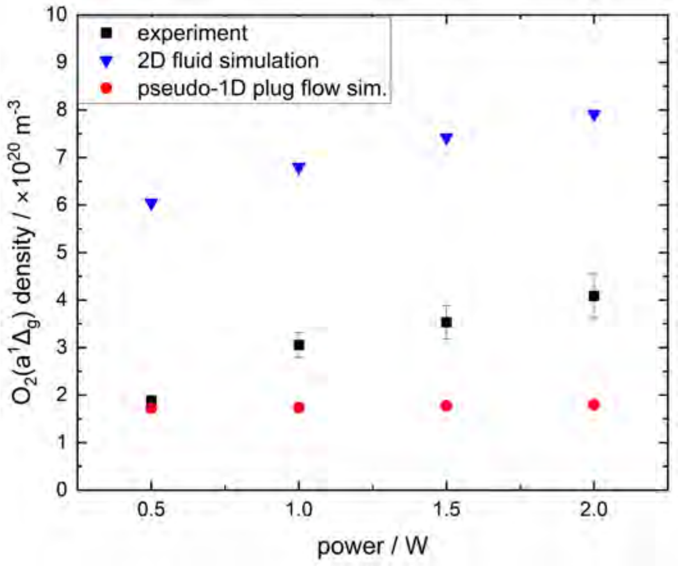

Figure 4.13: Comparison of $O_2(a^1\Delta_g)$ density between experiment and simulation for an effluent temperature of 300 K, helium flow of 1 slm, and an oxygen admixture of 0.5 %, as a function of plasma power.

calibration of the spectrometer and knowledge of the ozone quenching. The uncertainty for $O_2(a^1\Delta_g)$ was determined by the variance over multiple measurements, as well as the uncertainty of the ozone density by Gaussian error propagation. It was determined to be approximately 5%. High flows of 2 slm, however, exhibited an uncertainty of up to 10%. Due to challenging to determine values, such as the geometric factor, a systematic error may be significantly higher. The experimental results were then compared to the averaged values calculated from the simulation data.

Fig. 4.13 shows the dependence of $O_2(a^1\Delta_g)$ density on plasma power for both experiment and simulation. The 2D fluid simulation and the experimental data consistently exhibit an increase in density with higher power. Since $O_2(a^1\Delta_g)$ is primarily produced by electron impact excitation and by the reaction of $O_2(b^1\Sigma_g^+)$ with ozone, an increase in plasma power, which enhances both ozone and $O_2(b^1\Sigma_g^+)$ production, naturally leads to higher $O_2(a^1\Delta_g)$ densities.

The experimental measurements display a steady rise in $O_2(a^1\Delta_g)$ density with power. The 2D fluid simulation follows the same trend, though the simulated values are roughly three times larger. Nevertheless, the general behavior is well reproduced. As previously noted, the ozone distribution in the flow cell does not fully reach steady state during the short simulation time. This spatial inhomogeneity of ozone may locally lower the effective reaction rate with $O_2(a^1\Delta_g)$, resulting in higher average densities in the simulation.

The plug flow simulation yields densities of the same order of magnitude as the experiment and the 2D fluid model. However, it shows only a weak dependence on plasma power. This is primarily due to the slow gas velocity in the flow cell: because of the long residence time in both the cell and inlet tube, most of the $O_2(a^1\Delta_g)$ has already decayed. As a result, only the tail of the exponential distribution remains, which is less sensitive to changes in the initial $O_2(a^1\Delta_g)$ production inside the plasma channel.

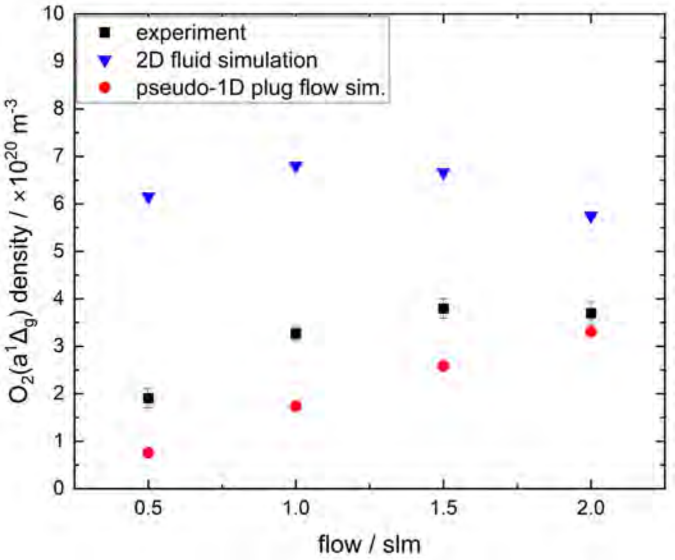

Figure 4.14: Comparison of $O_2(a^1\Delta_g)$ density between experiment and simulation for an effluent temperature of 300 K, plasma power of 1 W, and an oxygen admixture of 0.5 %, as a function of gas flow.

In Fig. 4.14, the $O_2(a^1\Delta_g)$ density is shown as a function of the gas flow. The experimental results indicate an increasing density with rising gas flow, reaching a maximum at 1.5 slm before slightly decreasing towards 2.0 slm. The shorter residence time at higher flow velocities reduces the $O_2(a^1\Delta_g)$ quenching, thereby allowing a higher density to reach the flow cell, increasing the average density. Conversely, the increased velocity reduces the residence time within the plasma region, which lowers the production of $O_2(a^1\Delta_g)$. These two effects appear to balance each other between 1.5 slm and 2.0 slm. Beyond this point, it is reasonable to assume that the density will decrease further, since the decreasing residence time in the plasma volume limits $O_2(a^1\Delta_g)$ formation.

The 2D fluid simulation shows a similar trend: an increase in $O_2(a^1\Delta_g)$ density between 0.5 slm and 1.0 slm, followed by a plateau and then a decline after 1.5 slm. This behavior can be explained in the same way as for the experiment. However, the decrease in the simulation occurs earlier, most likely because the species distribution has not reached complete equilibrium during the limited simulation time.

The plug flow simulation, in contrast, exhibits a more linear increase in density, with values slightly lower than those observed experimentally. Due to the low gas velocity in the flow cell, an increase in flow rate has a stronger effect on raising the averaged $O_2(a^1\Delta_g)$ density than the opposing reduction in production caused by the shorter residence time in the plasma volume. This results in the nearly linear trend. At flow rates beyond 2 slm, however, a decrease in density would still be expected as the residence time in the plasma region becomes too short for sufficient $O_2(a^1\Delta_g)$ production.

Fig. 4.15 illustrates the effect of varying the oxygen admixture on the $O_2(a^1\Delta_g)$ density, with plasma power held constant at 1 W. Experimentally, increasing the oxygen fraction leads to an asymptotic rise in $O_2(a^1\Delta_g)$ density in the effluent, likely due to the greater probability of electron impact excitation in the jet when more oxygen molecules

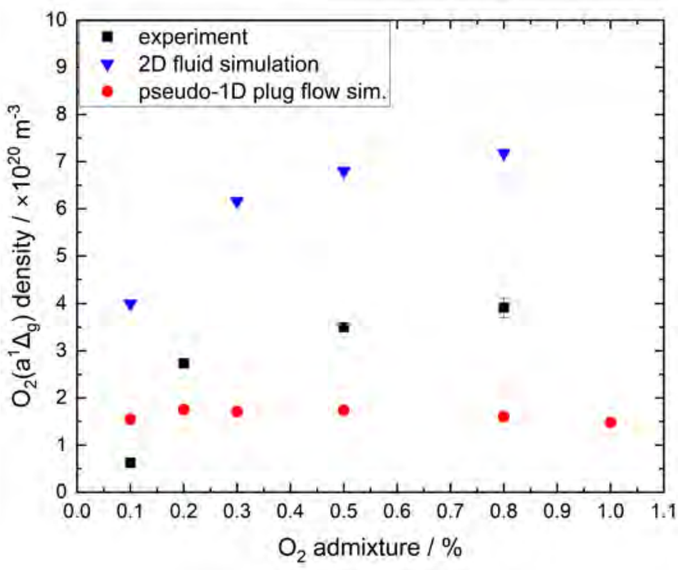

Figure 4.15: $O_2(a^1\Delta_g)$ density comparison between simulation and experiment for an effluent temperature of 300 K, power of 1 W and 1 slm He flow depending on the oxygen admixture.

are present. The 2D fluid simulation captures this trend closely but slightly overestimates the density values.

The plug flow simulation shows minimal sensitivity to the oxygen admixture. A small increase in density is observed between 0.1% and 0.2%, while it remains nearly constant for higher admixtures. For admixtures above 0.5%, the $O_2(a^1\Delta_g)$ density even slightly decreases. This behavior is attributed to the slow gas flow in the flow cell, resulting in a low density reaching the measurement region. Additionally, the higher ozone densities predicted by the plug flow model (see Fig. 4.10) enhance $O_2(a^1\Delta_g)$ destruction rates.

Overall, the plug flow simulation aligns well with the absolute experimental values but does not reproduce the trend accurately due to the likely underestimated gas velocity in the flow cell. In contrast, the 2D fluid simulation reproduces the experimental trend effectively but overestimates $O_2(a^1\Delta_g)$ densities, which is likely caused by the limited simulation time preventing an equilibrium. Longer simulations could reduce this discrepancy, as evidenced by the improved agreement at higher flow rates.

To assess whether the derived $O_2(a^1\Delta_g)$ densities are realistic, a comparison to other studies is needed, especially as $O_2(a^1\Delta_g)$ density is not highly validated for the simulations. Sousa *et al.* [35] measured $O_2(a^1\Delta_g)$ densities up to $\sim 1 \cdot 10^{21}$ m^{-3} using an RF-excited helium-oxygen APPJ with a 1 slm flow and 0.5% oxygen admixture. This is approximately a factor of three higher than the experimental values obtained in this study, likely caused by the differences in the APPJ design and the unspecified plasma power in their setup. Nevertheless, the values remain within the same order of magnitude.

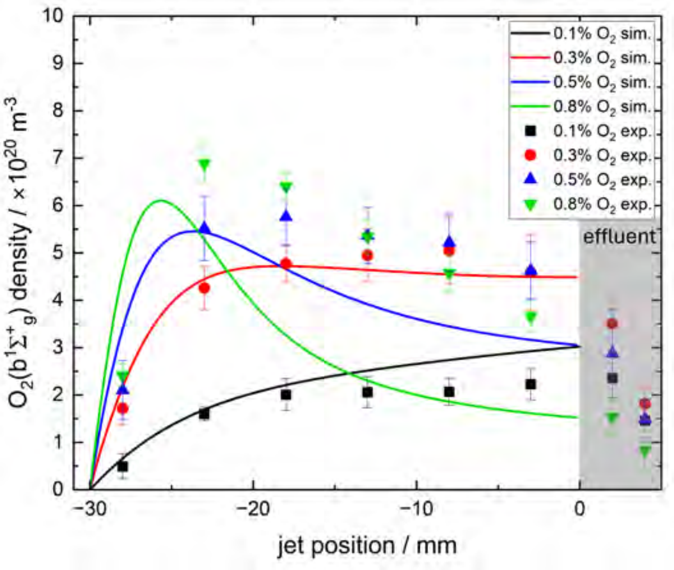

Figure 4.16: $O_2(b^1\Sigma_g^+)$ density distribution along the COST jet discharge channel for varying oxygen admixtures. The grey area indicates the effluent region. Plasma power: 1 W, helium flow: 1 slm.

4.1.5 $O_2(b^1\Sigma_g^+)$ Density

The $O_2(b^1\Sigma_g^+)$ spectra were recorded directly in the COST jet's discharge channel. The measured $O_2(b^1\Sigma_g^+)$ density in the jet stabilized immediately after plasma ignition, provided the jet had already reached its operating temperature. Therefore, no lengthy equilibration times were needed. For a given set of plasma parameters, the collimator was moved along the COST jet's discharge channel in steps of 5 mm and an $O_2(b^1\Sigma_g^+)$ spectrum was captured. Through the energy calibration of the spectrometer and the knowledge of the ozone density, the $O_2(b^1\Sigma_g^+)$ density could be calculated. As the measurements were performed directly inside the COST jet without the flow cell, no consideration of complicated effluent geometries is needed. Consequently, no comparison was made with the 2D fluid simulation.

Because the $O_2(b^1\Sigma_g^+)$ density strongly depends on both the position within the jet and the oxygen admixture, Fig. 4.16 focuses on these variations to highlight the differences between the 1D plug flow simulation and the experimentally determined values. The uncertainty of $O_2(b^1\Sigma_g^+)$ was calculated by the variance over multiple measurements. The uncertainty varied widely depending on the position within the jet. During the rise of the $O_2(b^1\Sigma_g^+)$ density uncertainties were around 15-20%. This is a result of the low density and the steep increase, which introduced a high deviation if the position in the jet was not exactly reproduced. During the equilibrium or slow decline, a smaller uncertainty of up to 10% was observed. In the effluent, the uncertainties were significantly higher, reaching up to 40%, which is expected near the detection limit, as well as gas convection and diffusion.

Fig. 4.16 shows the measured $O_2(b^1\Sigma_g^+)$ density along the discharge channel for different oxygen admixtures in comparison with the 1D plug flow model. At 0.1 % oxygen, the density rises asymptotically, reaching its maximum near the end of the discharge channel, then decays in the effluent. For 0.3 % oxygen, the density increases slightly steeper, and the maximum is reached earlier at around -8 mm from the jet exit, followed by a gradual decay. Higher oxygen admixtures exhibit a similar trend, with the maximum position shifting closer to the gas inlet and a modest increase in peak density as the oxygen fraction increases.

The plug flow simulation reproduces the experimental $O_2(b^1\Sigma_g^+)$ densities very well for oxygen admixtures of 0.1 % and 0.3 %. For higher admixtures, the simulated density reaches a maximum within the first third of the discharge channel, with the peak shifting closer to the jet inlet as the oxygen fraction increases, consistent with experimental observations. The maximum density also rises with increasing oxygen content. However, the post-peak decay in the simulation is faster than observed experimentally, resulting in lower densities at the channel exit compared to the experiment.

This behavior can be attributed to the simulation's overestimation of ozone density (see, e.g., Fig. 4.8). In the simulation, the ozone density rises along the discharge channel, enhancing the consumption of $O_2(b^1\Sigma_g^+)$. As ozone accumulates near the jet exit, the simulated $O_2(b^1\Sigma_g^+)$ density peaks earlier and decays more rapidly. The overestimation of ozone becomes more pronounced at higher oxygen admixtures, as shown in Fig. 4.10, which explains the discrepancy in the simulated $O_2(b^1\Sigma_g^+)$ profiles.

Overall, the plug flow simulation yields a good agreement with experimental values and accurately captures the general trends. The higher oxygen admixtures, however, reveal an overestimated consumption rate of $O_2(b^1\Sigma_g^+)$, likely caused by the elevated ozone densities in the simulation (Figures 4.8, 4.9, 4.10). These observations are consistent with the ozone measurements and support the conclusion that the simulation overestimates ozone production.

Experimental values of $O_2(b^1\Sigma_g^+)$ densities for APPJs were not found. Therefore, comparison with simulation results was crucial. Without such benchmarks, evaluating the reliability of experimental measurements would have been very challenging.

4.1.6 Summary & Concluding Remarks

Comparison of the experimental results with both the pseudo-1D plug flow and the 2D fluid simulations in the effluent region shows that each model successfully reproduces the species densities within the same order of magnitude as the measured values. This demonstrates that the plug flow model provides reliable estimates even in complex effluent geometries. The 2D fluid simulation, on the other hand, is able to accurately describe the trends in reactive species densities under varying power, flow rate, and admixture conditions, making it particularly suitable when detailed spatial distributions are required. Extending the simulation time to reach equilibrium in the flow cell better may further improve agreement with experimental results.

Both simulations overestimate the ozone density at oxygen admixtures above 0.1%, as discussed in the ozone density analysis. This overestimation is further supported by the elevated consumption of $O_2(b^1\Sigma_g^+)$ in the simulations compared to experimental measurements, suggesting limitations in the current reaction sets. These findings align with Turner's work [123], which highlights the strong coupling between $O_2(b^1\Sigma_g^+)$ and ozone densities. Moreover, uncertainties in surface reaction rates, particularly for oxygen species, may also contribute to the observed discrepancies, as wall reactions are not fully characterized and ozone-wall interactions are not accounted for.

Quantitative and qualitative differences between the plug flow and 2D simulations can be attributed to factors such as residence time, spatial resolution, and variations in the reaction sets. Though largely similar, the reaction sets used are not identical, and small differences can potentially impact species densities considerably due to the sensitivity of plasma chemistry to individual reactions [123].

To further improve the matching between simulations and experiment, refining the flow cell design could reduce vortex formation, potentially decreasing the required simulation time and improving agreement between experimental and simulation results. Additionally, a closer investigation of uncertain rate coefficients, especially for wall interactions in plasma and effluent regions, could yield better accuracy. Despite these limitations, the simulations perform well even under challenging conditions, underlining the robustness of the validated plasma chemistry models.

Since the COST jet used in this study is primarily employed with unconfined effluents, it is essential to evaluate the transferability of measured species densities to systems with unconfined effluents. Given the relatively long lifetimes of key species like $O_2(a^1\Delta_g)$ and ozone, their densities are likely representative even under unconfined conditions, provided the flow remains laminar. Furthermore, it has been shown that a controlled helium atmosphere, as used in the combined laser-plasma treatment setup, can prolong the lifetime of reactive species [19], resulting in conditions that resemble a confined effluent. However, in turbulent environments or differing application geometries, gas mixing could substantially alter species distributions. Nonetheless, these investigations offer a solid reference point and underscore the importance of accounting for strong species interactions in plasma effluent modeling.

The provided measurements of $O_2(a^1\Delta_g)$ allow a comparison to the atomic oxygen density measured in [55] for the COST jet. $O_2(a^1\Delta_g)$ is in the order of the atomic oxygen density at a surface with a distance of 8 mm. The former reaches around $4 \cdot 10^{20}\ \mathrm{m^{-3}}$ while atomic oxygen is at $3.5 \cdot 10^{20}\ \mathrm{m^{-3}}$. When considering a gas velocity of 16.67 m/s (with a 1 slm gas flow) for the 1 mm · 1 mm cross section of the COST jet, this results in fluxes of $\Gamma_{O_2(a^1\Delta_g)} = 6.6 \cdot 10^{19}\ \mathrm{m^{-2}s^{-1}}$ and $\Gamma_O = 2.1 \cdot 10^{19}\ \mathrm{m^{-2}s^{-1}}$. Therefore, the fluxes reaching the substrate surface are comparable, potentially facilitating the chemical processes suggested by Gusakov *et al.* [28] and enabling the formation of higher oxidation states like CuO on the copper substrates. The He + 0.5% oxygen admixture used for the surface modification measurements, therefore, provided a good compromise as it provided a high atomic oxygen density [54] while still offering a comparable $O_2(a^1\Delta_g)$ density for the chosen jet and surface distance.

It should be noted that the ratio between $O_2(a^1\Delta_g)$ and atomic oxygen can be influenced by the distance of the jet to the sample. For shorter distances, the atomic oxygen density is higher, while setting the jet and surface further apart increases the ratio towards $O_2(a^1\Delta_g)$, as atomic oxygen gets quenched much faster than the long-lived $O_2(a^1\Delta_g)$. The jet-surface distance could therefore be used to control the chemical composition of the surface. For shorter distances, a higher atomic oxygen density could lead to higher Cu_2O formation, as the higher atomic oxygen density oxidizes the surface but also triggers counter oxidation reactions, reverting CuO to Cu_2O.

4.2 ns-Laser Surface Structuring

The results presented here were supported by the work of Lennart Kulik during his Bachelor thesis, who performed the preliminary measurements in finding working laser parameters and contributed to the setup for the combined laser-plasma treatment. Experimental data were published in [55].

After establishing that the used parameters for the COST jet and sample interaction are favorable for CuO formation, laser parameters for a successful surface structuring are needed. The following chapter covers preparatory measurements of the laser source, as well as an investigation of the laser-induced surface structures and the influence of the COST jet effluent on their formation.

Spatial Filtering

Before performing surface structuring, a precise control of the laser parameters is necessary. Especially, the laser energy is important as it influences which structures are produced on a sample. The laser energy is carried by the laser pulse, which is spatially and temporally distributed. Its spatial distribution is especially important because an inhomogeneous energy profile complicates the localization and uniformity of surface modifications. Consequently, the beam shape has a significant influence on the success of laser structuring. A flat-top beam, with its homogeneous energy distribution across the spot, would be ideal for controlled processing. However, generating and maintaining this beam shape is challenging, as it is easily distorted by optical components, limiting its practical implementation.

Fig. 4.17 shows the original laser beam profile of the Nd:YAG laser system for the 532 nm beam. The laser is tuned to provide a flat-top profile, though, as is clearly seen here, the laser profile consists of multiple ring-like shapes, which are not homogeneous enough for controlled surface structuring. It is therefore unsuited for surface structuring. The intensity and scale of the images were left out as they are not important when evaluating the beam quality. Additionally, they were not taken in the focal point of the laser at the sample's position. Instead, they were collected before the focal lens into the chamber to have a better resolution on the profiler.

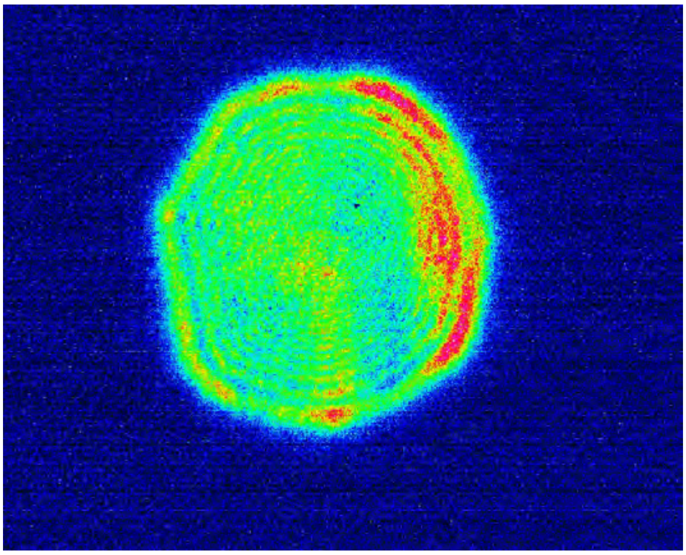

Figure 4.17: Laser profile of the 532 nm wavelength beam of the Nd:YAG laser system.

As established in the Beam Shape and Quality chapter, a more homogenous or "clean" beam shape can be achieved by spatial filtering. An example setup is shown in Fig. 2.6. To calculate the pinhole size for spatial filtering of the initial laser beam profile, Eq.(2.43) was used. For the setup, the following values apply: $\lambda = 532\,\text{nm}$, $f = 20\,\text{cm}$, and $D = 9\,\text{mm}$. This gives a theoretical pinhole size of:

$$D_P = 25.2\,\mu\text{m} \tag{4.1}$$

However, since the input beam is already assumed to be a Gaussian profile with small disturbances, and the laser employed within this study exhibits many diffraction effects and probably additional higher transverse modes, the beam cannot be focused as tightly as a single Gaussian beam. The beam waist is consequently considerably larger. A tighter focus and a smaller pinhole size often lead to damage to the pinhole. Ultimately, a pinhole with a diameter of 200 µm was employed. This provided a good compromise between robusticity and beam shape quality.

In Fig. 4.18, the left image shows the "clean" laser beam after spatial filtering, taken by a beam shape analyzer. Here, the 2D laser shape is depicted with the x-axis as the width and the y-axis representing height. When compared to Fig. 4.17 it can be observed that the profile is a lot more homogeneous.

Fig. 4.18 on the right shows a 1D-profile through the maximum of the 2D laser profile along the x-axis. The profile was fitted with a Gaussian to check for the quality of the spatial filtering. The high R^2 indicates that utilizing a pinhole was very successful in filtering out noise, leaving only the TEM_{00} mode. Although a Gaussian shape is less ideal than a flat-top profile, it still provides a predictable energy distribution within the laser spot, making it suitable for structuring surfaces.

A minimum laser energy is needed when inducing surface structures on a sample. Through

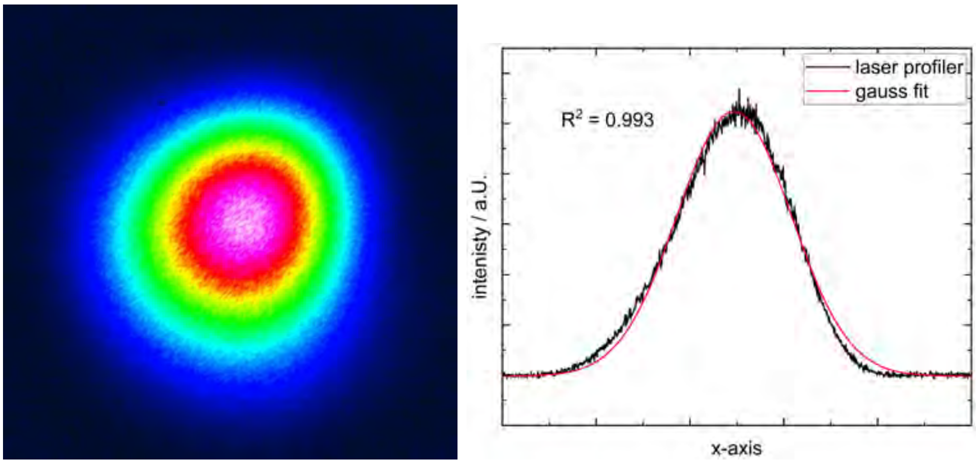

Figure 4.18: (left) Laser beam shape after spatial filtering for the 532 nm wavelength of the Nd:YAG laser system. (right) Gaussian fit of the 2D laser profile from the x-axis. Gaussian fit results in a R^2 of 0.993.

the Gaussian shape of the beam, the laser energy is not distributed evenly within the laser profile. This influences the size of the laser spot created on the sample when the laser energy is changed, as only the narrow peak of the laser beam possesses sufficient energy to meet the threshold energy of the surface. Therefore, lower energies should result in a smaller laser spot on the sample. To begin, the threshold energy of the Cu-coated Si wafers was investigated by varying the laser energy until no laser spot could be observed. This way, the threshold energy was determined to be approximately 260 µJ.

To investigate whether the threshold energy was the dominant mechanism behind the laser spot size on the sample after energy variation, its diameter was measured for different laser energies. Simultaneously, the beam shape was observed. The laser beam was measured with a beam shape analyzer (gentec-eo Beamage 3.0) and the induced laser spot on the sample was observed under a laser scanning microscope (Keyence VK-9700K Laserscan Color Microscope). For each of the given laser energies, the laser profile was measured with a beam profiler, and a spot on a copper film was induced. A minimal laser energy for inducing laser structures on the surface was found. This laser energy was related to a minimum intensity of the beam profiler measurements. The laser profiles were then fitted with a 3D Gaussian function to calculate their radii at this minimal intensity. For every laser energy, the radius of the equiline meeting the threshold intensity was calculated. The shape of the equilines for different laser energies is shown in Fig. 4.19. It can be seen that the diameter of the equilines gets smaller with a decrease in the laser energy.

Fig. 4.20 shows the normalized radius of the laser beam equilines compared to the radius of the induced spot on the surface for a laser energy variation. The radii were normalized to their respective maxima at 870 µJ. For both, a decrease in the radius size can be observed if the laser energy is decreased. The decrease for the induced spot size on the sample follows the radius of the equilines quite closely. Only for the spot near the threshold energy, the induced spot on the sample is higher than expected for the equiline of the laser profile. These observations suggest that the threshold energy is the dominant mechanism influencing the laser spot size generated on a sample. As the laser energy

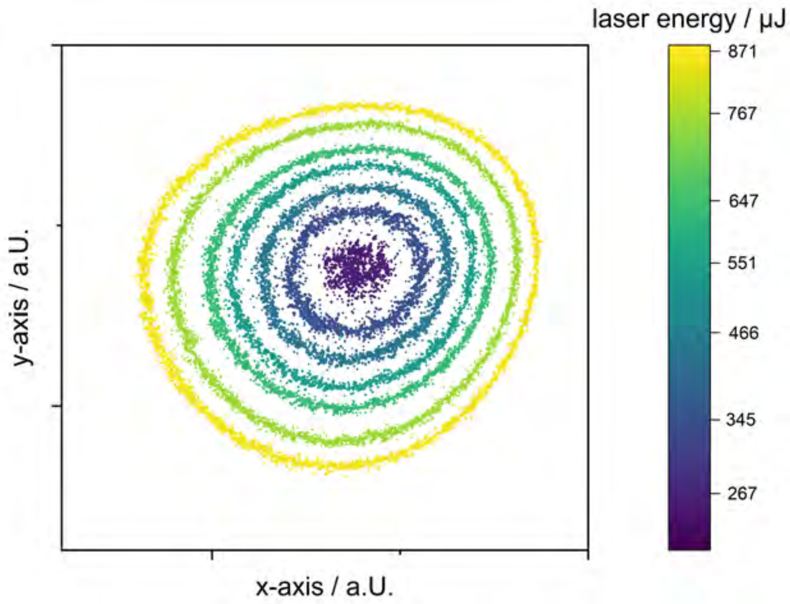

Figure 4.19: Laser profile equilines for a treshold energy of 260 µJ during laser energy variation. The equiline color indicates the laser pulse energy as shown on the color bar.

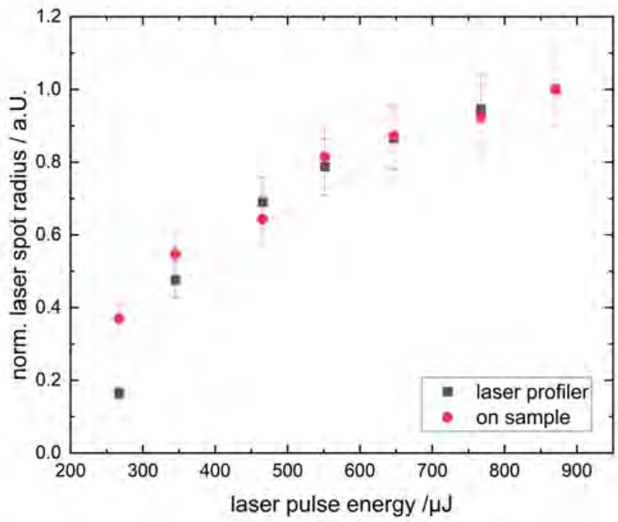

Figure 4.20: Normalized diameters of the laser profile compared to the induced laser spot on the sample.

decreases, a smaller area of the Gaussian profile is able to overcome the threshold energy, which reduces the observed beam size on the sample. The small deviation of the two radii for laser energies near the threshold can most likely be attributed to measurement errors. Controlling the exact laser energy is challenging, as the pulse energy is quite unstable from pulse to pulse, with a variance of up to 10%. It is also difficult to determine a precise border for a laser spot. Especially for the small spots, this may lead to greater uncertainty.

The threshold energy depends on the focusing of the beam and is therefore better understood as a threshold energy density. To reproduce these results, it might be valuable to know the laser fluence. Because the exact laser spot size in focus is hard to measure, it is only possible to give an estimate of this value through the size of the induced spot on a sample. For high laser energies, most laser profiles possess sufficient energy to overcome the threshold. This removes the dependency of the induced spot size on the laser energy, making it possible to deduce a laser fluence. The laser was focused on the sample at an energy of 870 µJ. After the treatment, a spot of approximately 247 µm radius was induced. This results in an upper threshold for the laser fluence of $3.5\,\mathrm{J/cm^2}$.

4.2.1 Pulsed Laser-Induced Dewetting on Copper Thin Films

With a controllable laser energy profile and knowledge of the threshold laser fluence, laser parameters for the successful formation of laser-induced surface structures can be investigated. For a systematic approach to finding suitable laser parameters, a well-defined and reproducible starting surface is required. This minimizes variations caused by differences in surface composition, oxidation, or roughness. Therefore, thin copper films were deposited on silicon wafers via high-power impulse magnetron sputtering (HiPIMS). These films provided clean surfaces with very low roughness and allowed precise control of the film thickness. The samples were then positioned on the stage inside the combined laser-plasma chamber and irradiated by the laser in a helium atmosphere. Through the pulsed laser-induced dewetting (PLID) mechanism, nanoparticles were formed on the prepared copper layers.

The nanoparticle spacing and size in PLID can be described by the thin film hydrodynamic dewetting theory [48] proposed by Trice *et al.*. To validate this correlation, copper films of varying thicknesses, ranging from 3 nm to 10 nm, were irradiated until particle formation was observed. Although the optimum laser parameters vary with film thickness, the particle size and distribution did not change considerably for irradiation times between 5 s and 20 s, corresponding to 100 and 400 shots, respectively. Therefore, for all investigated thicknesses, a laser energy of approximately 560 µJ with an irradiation time of 10 s (200 shots) was applied, striking a balance between sufficient time for complete pattern formation and short enough to prevent sample damage.

The PLID-generated nanostructures were analyzed using secondary electron microscopy. Particle diameters were determined with ImageJ, and their distributions were fitted with a Gaussian to extract the mean diameter for each film thickness. As illustrated in Fig. 4.21, the diameter dependence follows the prediction of thin film hydrodynamic dewetting

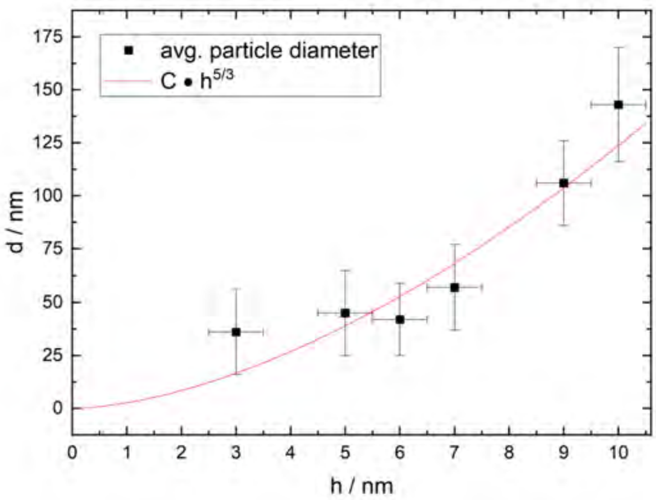

Figure 4.21: PLID nanoparticle diameter as a function of copper layer thickness, fitted using thin film hydrodynamic dewetting theory as described by Trice *et al.* [48]. The inserted image shows PLID nanoparticles after 10 s of laser irradiation on a 4 nm copper layer on silicon.

theory [48] very closely. Assuming a hemispherical particle geometry, and by evaluating the mean nearest-neighbor distance and particle diameter, the resulting surface roughness was estimated to be $R_m = 8 \pm 1$ nm with a particle density of $\rho = 3 \pm 1$ µm^{-2} for a layer thickness of 10 nm.

4.2.2 Gas Flow Interaction with Surface Structuring

Extensive research has been carried out on the formation of laser-induced surface structures [48, 49]. Yet, the effect of a gas flow or the presence of reactive species in an effluent have not been systematically explored. Since both nanoparticle formation and the incorporation of reactive species into the surface are crucial for the presented approach, it was necessary to examine how surface structuring and plasma treatment interact and how potential disturbances can be mitigated.

It was found that introducing a gas flow during laser irradiation alters the optimal conditions for reproducible nanoparticle formation. Therefore, both the distance of the jet to the substrate and the laser pulse energy were varied to study their influence on nanoparticle generation and to determine parameter ranges that allow stable and consistent surface structuring under combined treatment conditions.

Fig. 4.22 shows SEM images after laser irradiation at 560 µJ with a helium flow of 1 slm for different jet-to-surface distances. At the smallest distance of 3 mm (Fig. 4.22(a)), no PLID nanoparticles are formed; instead, LIPSS or hole-like structures dominate. This behavior can be explained by the cooling of the copper film through the gas flow during irradiation. For PLID to occur according to thin-film hydrodynamic dewetting theory, the surface must undergo instantaneous melting, avoiding steep temperature gradients [48]. The helium flow, however, provides additional cooling, which may prevent complete melting during a single pulse and thereby hinder nanoparticle formation.

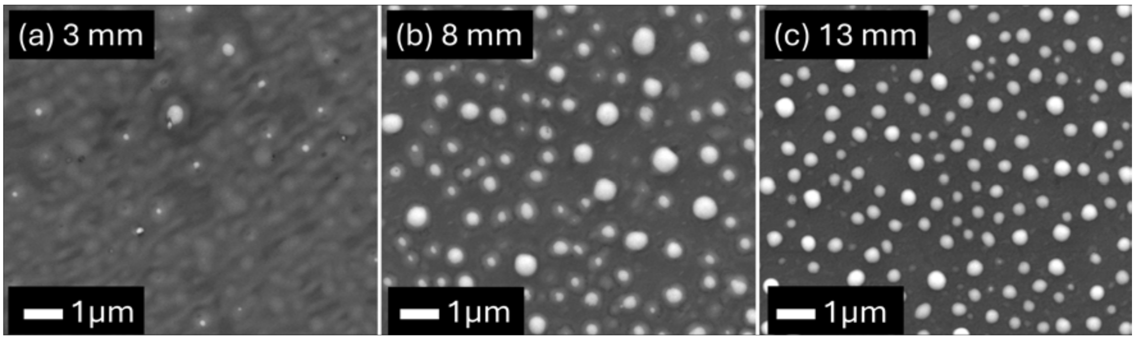

Figure 4.22: SEM images of PLID nanoparticles for a laser energy of 560 µJ and a He gas flow of 1 slm with different jet-to-surface distances: (a) 3 mm, (b) 8 mm, and (c) 13 mm.

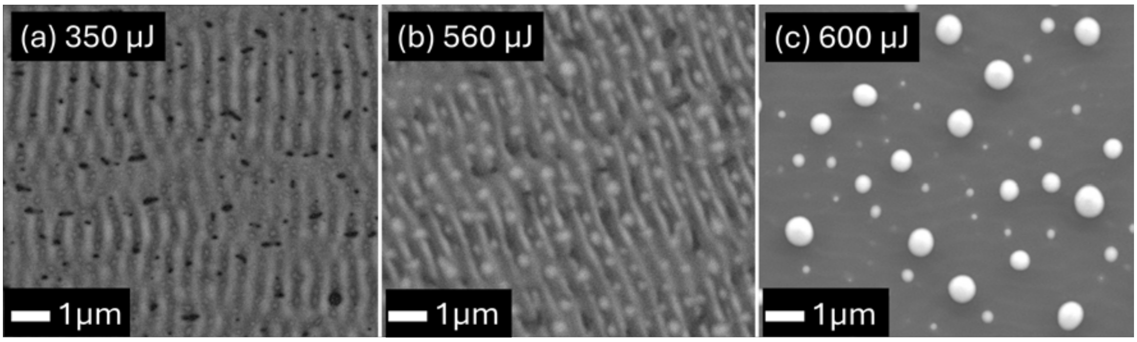

Figure 4.23: SEM images of PLID nanoparticles for a 10 nm Cu layer with 1 slm He gas flow and an 8 mm jet-to-surface distance at different laser energies: (a) 350 µJ, (b) 560 µJ, and (c) 600 µJ.

At 8 mm jet-to-surface distance (Fig. 4.22(b)), particles are formed but appear distorted or "smeared" compared to PLID without gas flow. Besides cooling, the flowing helium may disrupt droplet formation through frictional forces. At 13 mm distance (Fig. 4.22(c)), well-defined nanoparticles are observed. At this range, the gas jet's interaction with the sample surface is weak enough not to disturb the process, likely due to decreasing flow velocity caused by Stokes friction with the surrounding atmosphere. However, atomic oxygen density measurements [55] suggest that at 1 slm flow and larger jet-to-surface distances, the reactive species densities become too low to effectively influence surface chemistry, limiting distance variation as a viable control parameter.

An alternative approach to counteracting the cooling effect of the gas flow is to increase the laser energy, thereby ensuring complete melting of the copper film during each pulse. Fig. 4.23 presents SEM images of surface morphologies for different laser energies at an 8 mm jet-to-surface distance under 1 slm helium flow.

At lower energies, 350 µJ and 560 µJ, LIPSS formation dominates, as seen in Figs. 4.23(a) and (b). In particular, Fig. 4.23(b) shows a transition state, with LIPSS-like periodic structures containing some particle-like features. This indicates that the energy input was insufficient to completely melt the film under the cooling influence of the gas flow. LIPSS result from the interference of incident and surface-scattered laser light [47] and do not require a fully molten surface, explaining their predominance under these conditions.

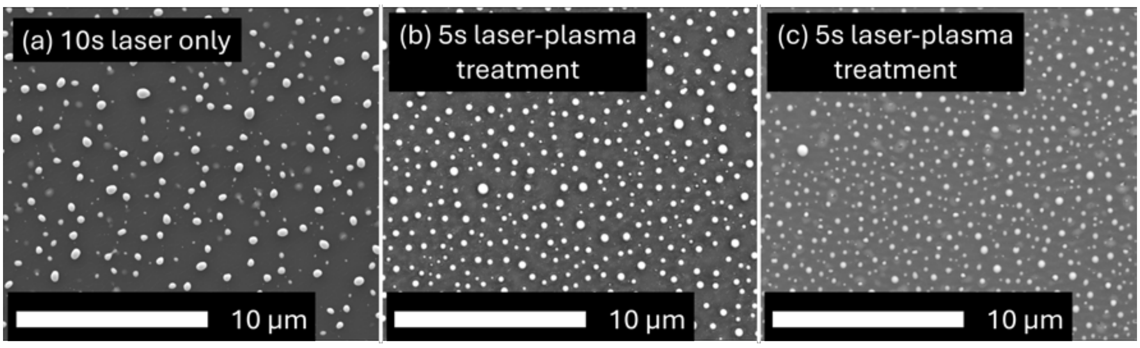

Figure 4.24: SEM images of the PLID nanoparticles for a 10 nm Cu layer on silicon for the different treatment types. (a) 560 µJ laser pulse energy for 10 s laser irradiation without gas flow, (b) 600 µJ laser pulse energy for 5 s with laser-plasma treatment, (c) 600 µJ laser pulse energy for 10 s with laser-plasma treatment

At 600 µJ (Fig. 4.23(c)), complete PLID nanoparticle formation is achieved. Thus, higher laser energy compensates for gas-flow-induced cooling and enables surface morphologies comparable to those obtained without gas flow. This is critical for subsequent comparisons of purely laser-structured versus laser-plasma-treated samples, as the surface morphology affects the resulting chemical modifications.

Fig. 4.24 shows SEM images of the spots investigated with XPS. Image a) depicts the laser irradiated surface, while b) and c) show the surface after combined treatment of plasma and laser for 5 s and 10 s, respectively. The difference in particle size and distribution between the treatments is within the uncertainty shown in Fig. 4.21 for a layer thickness of 10 nm. This is beneficial for a XPS analysis as different surface structures could potentially disturb the comparability between measurements.

4.2.3 Laser Scanning Scale-up

The employed laser surface structuring generated only small spots on the treated samples. This method provided a controlled approach to studying the effects of treatment time and laser energy variation on the structuring and chemical composition of samples. However, analysis methods like cyclic voltammetry or gas chromatography, which could provide more insight into the actual catalytic performance of the treated surfaces, often require larger surface areas. Small structures, therefore, pose a significant challenge to these methods. A scale-up is needed to provide a bigger surface area that these techniques can utilize. To that end, laser scanning was employed to increase the size of the treated area. Samples were placed in the vacuum chamber under a controlled atmosphere. A constant flow of 1 slm helium was chosen without oxygen admixture, as the primary focus of these measurements was surface structuring rather than chemical composition control. The jet had a distance of 5 mm from the sample.

Fig. 4.25 shows a schematic for the laser scanning with the two variables, step size s_{step} and scan velocity $\vec{v}_{\text{scan}}$. For a given laser energy, the sample was scanned by slowly moving the sample holder in the vacuum chamber at a constant speed until the desired length of

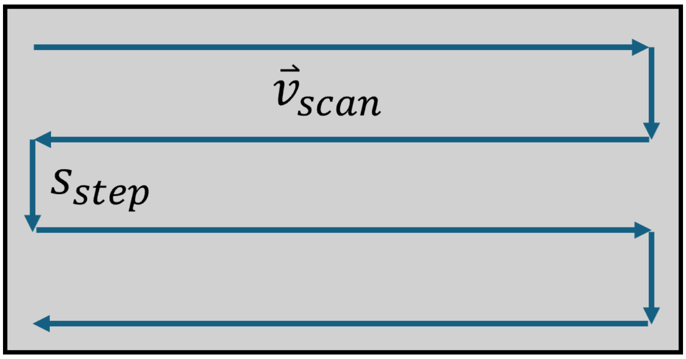

Figure 4.25: Laser scanning schematic with step size s_{step} and scan velocity $\vec{v}_{\text{scan}}$.

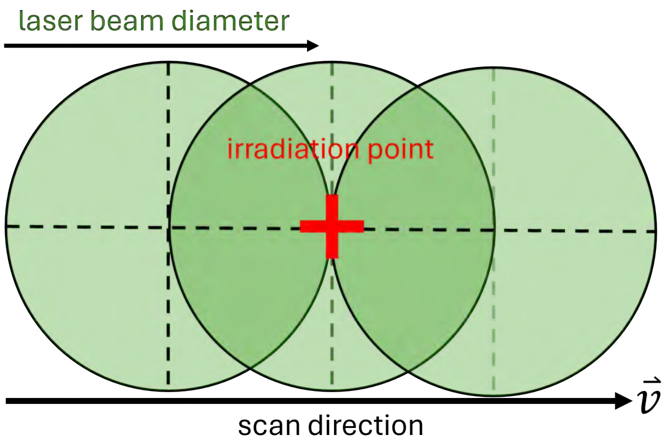

Figure 4.26: Irradiation time for a point on the sample surface (red cross) for the laser scanning (velocity direction indicated by $\vec{v}$) is dependent on the laser spot size and the scanning velocity.

the structuring area was reached. The sample stage then performed a downwards step according to the step size, and the scanning was repeated in the opposite direction. This way, a variable area could be treated. However, the low repetition rate of 20 Hz of the laser resulted in long treatment times to generate bigger areas. An area of 1 cm × 1 cm took roughly 3 h.

To have a reference to previous laser spot measurements, a connection between the scan velocity and the previously used irradiation time had to be established. Fig. 4.26 visualizes the irradiation time, which a spot on the surface endures for the laser scanning method. The green area indicates the laser profile, which exceeds the energy threshold for surface structuring. When considering a spot on the surface right at the edge of the profile in scan direction, it becomes clear that its irradiation time only depends on the laser diameter and the scan velocity (the velocity with which the laser moves over the sample). The irradiation time is then the duration that the laser beam profile needs to pass over the spot. It can then be calculated by: $t = \frac{r_{\text{laser}}}{v_{\text{scan}}}$. For previous measurements, the induced spot on the surface was roughly 400 nm in diameter with a typical irradiation time of 10 s. To achieve comparable conditions for laser scanning, the scan velocity would therefore result in $v_{\text{scan}} = 40\,\mu\text{m/s}$.

In reality 50 µm/s and even 100 µm/s scanning speeds had the best results. These speeds

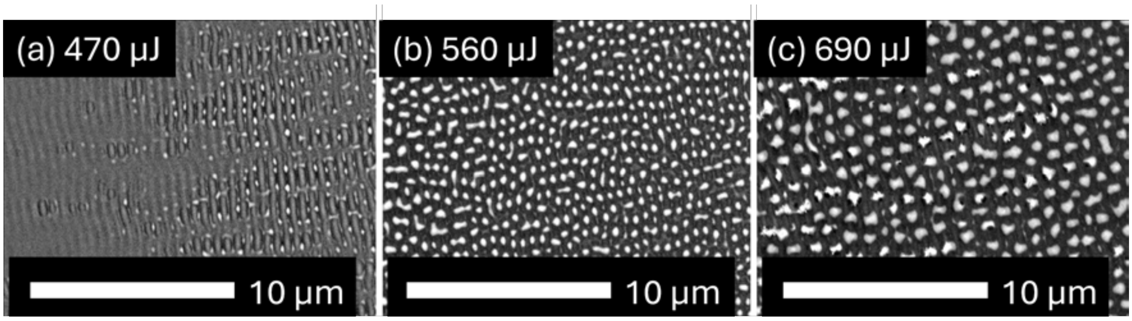

Figure 4.27: SEM images of surface structuring by laser scanning for (a) 470 µJ, (b) 560 µJ and (c) 690 µJ. All measurements were performed with a scanning speed of 50 µm/s and a step size of 50 µm.

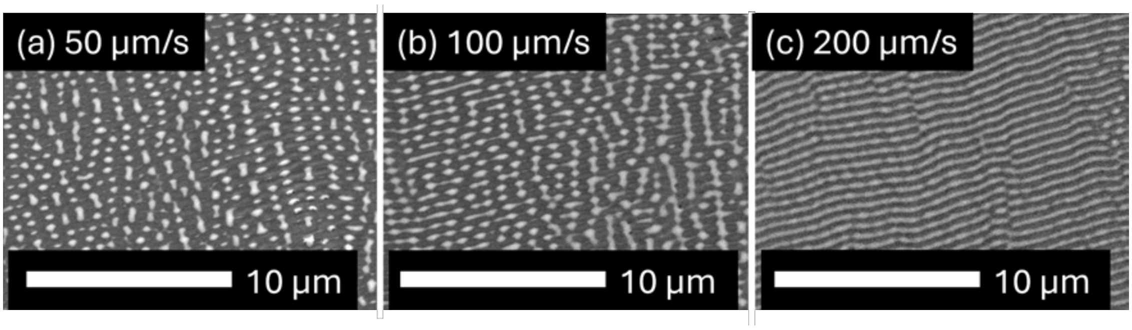

Figure 4.28: Surface structuring SEM images by laser scanning for (a) 50 µm/s, (b) 100 µm/s and (c) 200 µm/s. All measurements were performed with laser energy of 640 µJ and a step size of 50 µm.

are very close to the theoretical calculation, though. The slightly higher scan speeds likely result from the errors and inaccuracies in the laser profile, particularly the energy threshold. Even though the energy of the laser profile edge is not high enough to melt the surface, it is still able to heat it, which eases the melting when the laser is moved. This resulted in higher scan speeds or lower required irradiation times when compared to the laser spot structuring.

In contrast to the laser spot structuring, the laser scanning resulted in a much more homogeneous surface structure. Likely because the scanning compensated for the inhomogeneous laser profile. Fig. 4.27 depicts SEM images for a laser energy variation of a) 470 µJ, b) 560 µJ, and c) 690 µJ. The scanning speed of 50 µm/s and step size of 50 µm were the same for all measurements. A more LIPSS-like structure is visible for the lowest energy, as seen in Fig. 4.27 a). This then transitions to a mix of PLID and LIPSS structure for b) and then full PLIDS for c). This is consistent with previous findings for the laser spot measurements, where lower laser energies also produce LIPSS. However, for the laser scanning, a laser energy of 560 µm is already producing more PLID-like structures than the spot treatment. Additionally, successful PLID formation was observable up to an energy of 730 µJ. This may indicate that the successful formation of PLIDS for the laser scanning is somewhat more tolerant to variations in pulse energy compared to the spot treatment. A likely cause is the more homogeneous distribution of the laser energy over the treatment area.

Another parameter that influences the laser energy input to the sample is the scan velocity.

Faster scan rates should result in a lower energy input. Fig. 4.28 depicts SEM images for scanning speeds of a) 50 µm/s, b) 100 µm/s and c) 200 µm/s. The laser energy was kept the same at 640 µJ and the step size at 50 µm. Scan velocities of 50 µm/s result in PLID formation as previously established. Increasing the speed to 100 µm/s results in a composite structuring of PLIDS and LIPSS. A scan velocity of 200 µm/s is able to produce very homogeneous LIPSS. The scan velocity impacts the energy input into the surface, but the laser energy still plays a critical role. These structures were not observable with lower laser energies, highlighting that irradiation time and laser energy are not interchangeable, even though both contribute to the energy deposition into the sample.

4.2.4 Bulk Material Surface Structuring

The ns-laser surface structuring of the copper foil was performed by Jannis Kaufmann during his Master thesis, who also helped to build the electropolishing setup.

For real-world conditions, copper bulk materials like foils are much more applicable than thin film coatings. Thin layers provide very defined surface conditions, ideal for getting a grasp on tuning the laser parameters for successful surface structuring. However, they are very delicate under catalysis conditions and expensive to fabricate on large areas. To meet application requirements, a transition to bulk materials is needed. A thin copper foil (99.95% OFHC Copper Foil 0.1mm thick hard, CV00-FL-000261, from Goodfellow) was employed. PLID structuring is only possible on thin layer compound materials. This necessitated the switch to other laser structuring mechanisms, namely LIPSS.

This chapter provides an overview of the similarities and differences between the surface structuring of bulk materials and the more intensively studied thin layers using the ns-laser. This study shows that it is possible to produce reliable LIPSS patterns on bulk materials using a ns-laser, Even though the structuring of the bulk materials is much more complicated with the ns-laser, due to the rougher surface of the copper foil compared to the deposited copper layers.

The copper foil has a very rough surface, which complicates the investigation of successful laser parameters for surface structuring, as laser structuring is much more reliably achieved on smooth surfaces. To ease this process, the copper foil was electropolished for 300 s in phosphoric acid at a voltage of 3 V with a resulting current of 0.1 A to achieve a smoother surface. The surface structure change is presented in Fig. 4.29. The left side shows the original rough surface with a roughness of $R_q = 3.1\,\mu m$, most likely from the rolling of the copper foil. After electropolishing, the surface is smoothed and “islands”, most likely crystal facets, are visible. LSM measurements over an area of 10 mm resulted in a surface roughness decrease to $R_q = 1.5\,\mu m$. In the SEM image of Fig. 4.29, however, a roughness of that magnitude would be visible. Therefore, the roughness is probably much smoother on smaller scales in the µm-range. The SEM images did not allow for a quantification of the surface roughness.

Fig. 4.30 compares the SEM image of the electropolished Cu foil with the electropolished

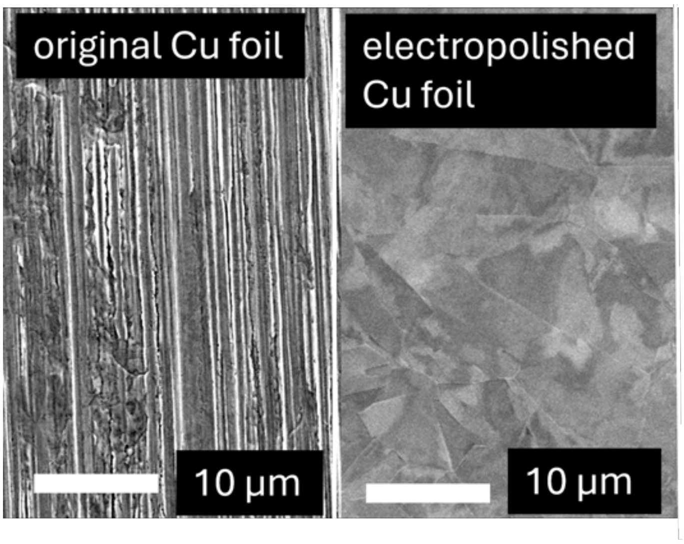

Figure 4.29: SEM images of the original Cu foil (left) and after electropolishing (right) in phosphoric acid for 300 s at a voltage of 3 V with a resulting current of 0.1 A.

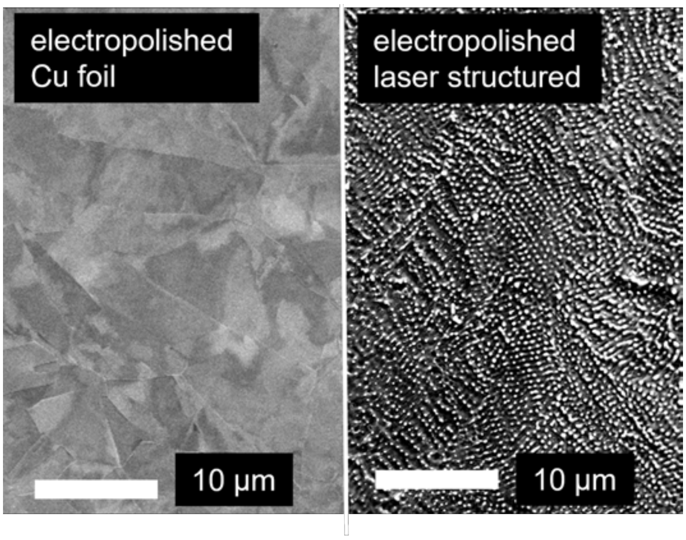

Figure 4.30: SEM images of electropolished Cu foil untreated (left) and laser structured (right) with a laser energy of 600 µJ, scan rate of 50 µm/s.

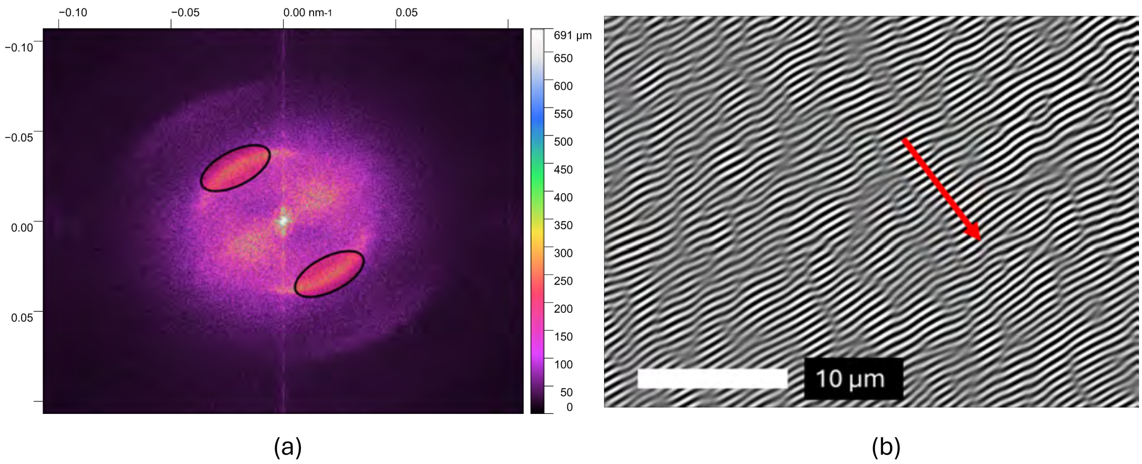

Figure 4.31: (a) 2D-FFT of the electropolished laser structured copper foil SEM image 4.30. Red areas indicate the filter of the most prominent periodic structures. (b) Zoomed in filtered 2D-FFT back-transformation.

Cu foil after laser structuring. Laser parameters for succesful LIPSS formation are a laser energy of 600 µJ and a scan rate of 50 µm/s. On the bulk copper, the LIPSS appear less parallel than for the thin films, although periodic structures are still faintly visible. To confirm the formation of LIPSS and exclude that these structures are just a roughening of the surface via melting by the laser, a 2D-Fast-Fourier-Transformation (2D-FFT) was used to extract periodic structures.

This transformation plots recurring periodic structures of the 2D SEM image into a 2D periodicity map. In Fourier space, the distance to the origin gives the periodicity. A periodic pattern would therefore be transformed into one point in Fourier space. Of course, real space structures seldom possess a perfect periodicity, which leads to a blurring in Fourier space. A point's intensity is specified by the number of structures with the same periodicity in the real-space image. The rotation of the Fourier space pattern in the x-y plane is given by the orientation of the periodic structures in real space. To isolate patterns in Fourier space, a filter for a specific periodicity can be employed, which is then back-transformed into real space. The resulting image only contains the periodic surface structures specified by the filter.

This is illustrated in Fig. 4.31. Fig. 4.31 (a) shows the 2D-FFT of the copper foil SEM image as seen in Fig. 4.30. The transformation was performed using the Gwyddion software, which can also generate the filtered back transformation, as shown in (b). The Fourier-transformed image was filtered for the most intense recurring periodic structure as shown by the red area. In the filtered back transformation only the red area is considered. The resulting wave-like pattern strongly indicates that the laser-induced structures on the electropolished Cu foil are indeed LIPSS.

LIPSS periodicity is mostly in the range of the laser wavelength. The periodicity of structures can be calculated in Fourier space by their distance to the point of origin. The inverse of the periodicity is then the pattern distance of the LIPSS $d = \frac{1}{\Lambda}$. The distance between two LIPSS peaks in Fourier-space was measured to 564 nm. Fig. 4.32 shows the

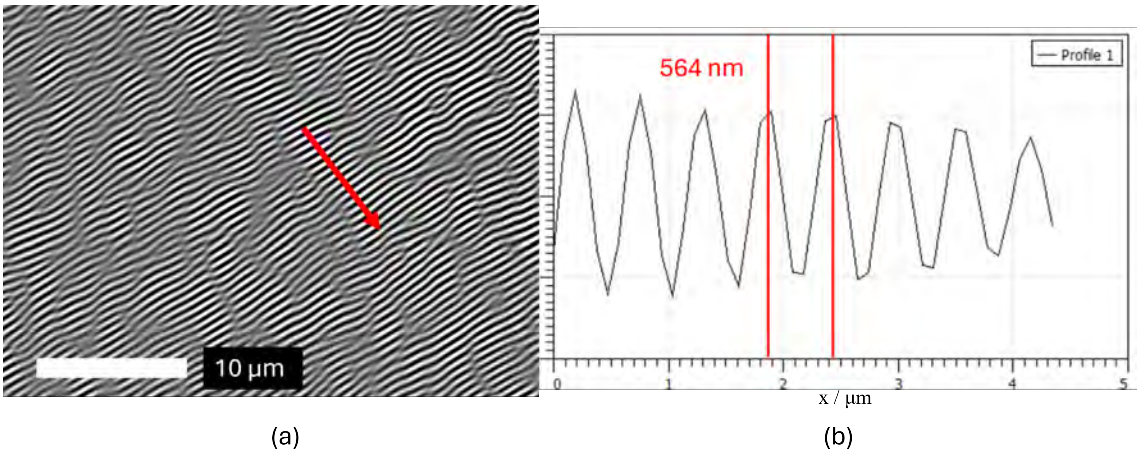

Figure 4.32: (a) Zoomed in filtered 2D-FFT back-transformation. (b) One-dimensional cut through the filtered LIPSS image along the direction indicated by the red arrow. Periodicity analysis predicts a 564 nm distance of the LIPSS maxima.

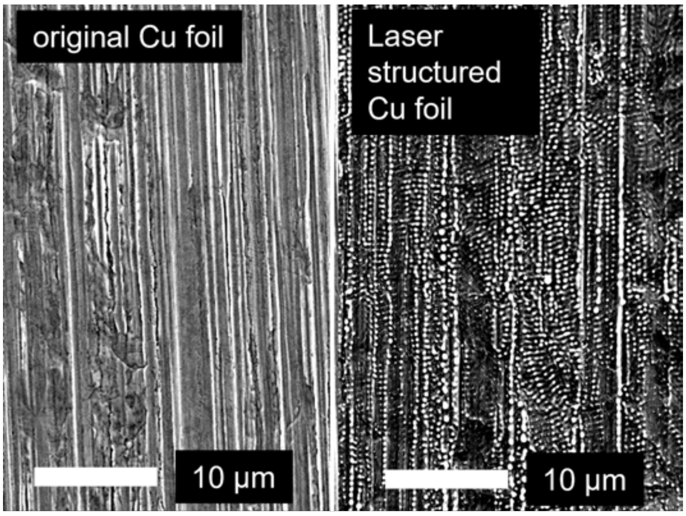

Figure 4.33: SEM images of the original Cu foil surface (left) and laser structured (right) with a laser energy of 600 µJ, scan rate of 50 µm/s.

one-dimensional intensity variation perpendicular to the depicted LIPSS pattern shown in Fig. 4.31 (b). It visualizes the LIPSS pattern distance calculated by the 2D-FFT, which aligns well with the 1D cut through the filtered LIPSS pattern. The calculated pattern distance is slightly larger than the used laser wavelength at 532 nm, but still comparable. The small deviation from the laser wavelength is most likely rooted in an uncertainty of the blurring in Fourier space through the existence of multiple periodic structures on the sample. Additionally, the laser might hit the sample at an angle instead of being perfectly perpendicular, which also results in an increase of the LIPSS distance as shown in [91]. Despite the deviation, the LIPSS periodicity correlates quite well with the laser wavelength, which is another indicator that the observed structures are LIPSS.

With knowledge about succesful laser paramerts for surface structuring it is possible to also generate LIPSS on the unpolished and therefore rougher surface of the coper foil. Fig. 4.33 shows SEM images of the unpolished copper foil surface (left) in comparison to

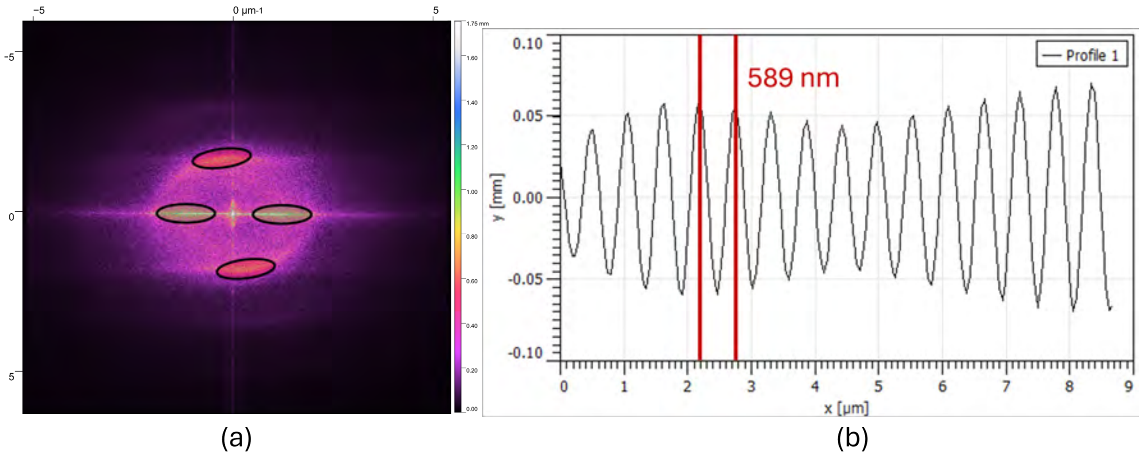

Figure 4.34: (a) 2D-FFT of the laser structured unpolished copper foil SEM image 4.33. The red area indicates the filtered periodicity for the back-transformation. The green area shows the periodic structures caused by the rolling of the foil. (b) LIPSS profile for a perpendicular cut through the back-transformed 2D-FFT.

post laser structuring (right). There are clearly periodic structures visible. Although the original “stripe”-like pattern of the unpolished foil is more prominent. To verify that the structures are indeed LIPSS, the image was analyzed as described above using 2D-FFT.

Fig. 4.34 (a) shows the 2D-FFT of the laser-structured SEM image in 4.33. The 2D-FFT image is much noisier than for the polished foil. This can be attributed to the rougher surface of the unpolished foil. There is also a high-intensity area along the x-axis of the image, as indicated by the green area. When transformed back (backtransfored not shown here), it becomes clear that this relates to the “stripe”-like patterns on the unpolished surface caused by the rolling of the copper foil. The red area marks the filter mask to extract the LIPSS structures. Fig. 4.34 (b) shows a perpendicular cut through the LIPSS pattern. A periodicity analysis as described previously reveals a mean distance between two LIPSS maxima to be at 589 nm. This is higher than for the polished foil. As before, this might be caused by the uncertainty of the much noisier data, which leads to a less homogeneous back transformation and LIPSS pattern. Another factor is the laser-sample alignment as described before. Additionally, the rougher surface may interfere with the laser structuring process, potentially increasing the size of the produced laser structures. Nevertheless, laser-induced structures offer a robust and reliable method for structuring even rough surfaces of bulk materials.

4.2.5 Summary & Concluding Remarks

Two materials were investigated regarding their laser surface structuring with a ns-laser. On thin films, laser irradiation facilitated the formation of nanoscale surface features, especially nanoparticles, which, in general, enhance catalytic properties [44–46]. SEM revealed that pulsed laser-induced dewetting governed the structuring, with nanoparticle size controlled by film thickness, consistent with the thin-film instability model by Trice *et al.*.

However, the gas flow from the COST jet interfered with nanoparticle formation by providing additional surface cooling, inhibiting complete melting. While increasing the jet-to-surface distance mitigated its influence, it also reduces the atomic oxygen density reaching the surface. A more promising alternative was raising the laser power to overcome the cooling effect and re-enable nanoparticle formation. The resulting particle distribution was homogeneous across the laser spot.

Lastly, surface structuring of copper foils as a bulk material was covered. Initially the foil possessed a rough surface, which made laser structuring challenging. Potentially, the surface roughness also may overshadow the effects of laser-induced surface structures on catalysis performance. However, a simple electropolishing process led to a smoother surface. Using 2D-FFT, it was confirmed that LIPSS could be produced on the polished and unpolished surfaces. Both had very similar periodicity to the LIPSS observed for the thin films. Therefore, ns-lasers offer a reliable tool to also structure bulk material surfaces, although the formation of these structures using ns-lasers is quite challenging. Moreover, the particles formed through PLID resist agglomeration, a common drawback in traditional nanoparticle fabrication, making this technique attractive in catalyst design.

4.3 Chemical Composition Analysis

Numerous studies have demonstrated that the chemical surface composition, in particular copper oxides, strongly influences catalytic performance by affecting both energy efficiency [11, 37–40] and selectivity [36]. Therefore, analyzing the surface chemistry is essential to evaluate its catalytic potential. Additionally, it is necessary to investigate how laser irradiation and its associated surface structuring influence copper oxidation in the presence of reactive plasma species. For this purpose, XPS measurements were carried out on the treated thin films. All experiments were performed in a helium atmosphere with an admixture of 0.5% oxygen.

4.3.1 XPS Analysis Method

To assess the effect of combined laser and plasma treatment on the oxidation state of copper, the samples were analyzed using an XPS device (PHI 5000 Versaprobe), focusing on the Cu2p and CuLMM Auger spectra.

During XPS measurements, charging effects can shift the recorded binding energies. A standard procedure to compensate for this, the adventitious carbon peak (C1s) was used as a reference. A thin carbon layer is present on any air-exposed sample, and the C−C bond provides a stable peak at 284.8 eV. Other measured energies were corrected accordingly to minimize charging-induced errors. The correction was carried out by fitting the C1s spectrum, where the C−C, C−OH, C=O, and OC=O contributions were fitted separately. After fitting, the C−C peak position was aligned to 284.8 eV. The position constraints for the different bond types are listed in Tab. 4.1. The FWHM was kept constant for all peaks, using the C−C bond (A) as reference.

Table 4.1: Fit constraints of the C1s bond types for charge correction.

bond type	position constraints / eV
C−C (A)	290.486 – 284.516
C−OH (B)	A+1.5
C=O (C)	A+3
OC=O (D)	291.629 , 291.486

Copper is a highly reactive metal and can form a variety of oxidation states. These are commonly categorized into Cu(0) (metallic copper), Cu(I), and Cu(II). Although higher oxidation states such as Cu(III) or Cu(IV) have been reported [138], they are unstable under ambient conditions and difficult to synthesize. This study focuses on the catalytically relevant copper oxide and hydroxide species: the Cu(I) oxide Cu_2O, and the Cu(II) species CuO and $Cu(OH)_2$, which are of primary interest for CO_2 reduction reaction (CO_2-RR) catalysts.

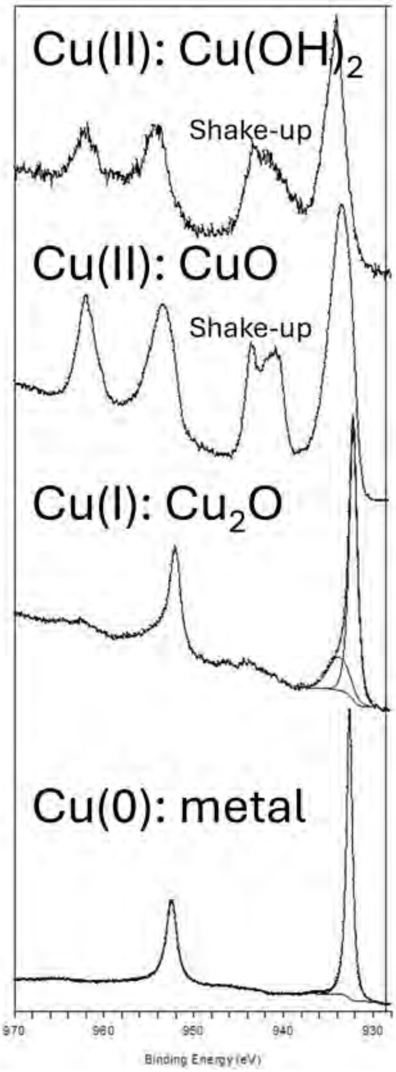

Figure 4.35: Cu 2p spectra for Cu metal, Cu_2O, CuO and Cu(OH)2 from bottom to top [137].

The most often referenced spectrum for copper XPS analysis is the Cu2p peak at binding energies from 920 eV to 955 eV as shown in Fig. 4.35. It illustrates the peak shape of the Cu2p spectrum for pure copper species, metallic copper, Cu_2O, CuO and $Cu(OH)_2$. While metallic Cu and Cu(I) peaks (Cu_2O) are indistinguishable in their binding energy, the Cu(II) species, CuO and $Cu(OH)_2$ exert a noticeable shift to higher binding energies. The two Cu(II) species also introduce so-called satellite or shake-up peaks with a noticeable shift in their binding energy into the spectrum. For the analysis of copper, they hold special relevance, as shake-up peaks are observed in Cu(II) compounds but not in Cu(I) or metallic copper because of differences in their electronic structures, as shown in Fig. 4.35. Cu(II) has an unfilled 3d shell, which provides unoccupied electronic states close in energy to the filled valence states. This allows valence electrons to be excited into these unoccupied states during photoemission, producing shake-up satellites. In contrast, Cu(I) and metallic Cu have filled 3d shells, leaving no available states for excitation. Therefore, shake-up peaks are an indicator of the presence of Cu(II) species.

A quantitative analysis, however, is nearly impossible using the Cu2p spectrum, because the peaks of Cu metal and Cu(I) species, as well as CuO and $Cu(OH)_2$, have very similar

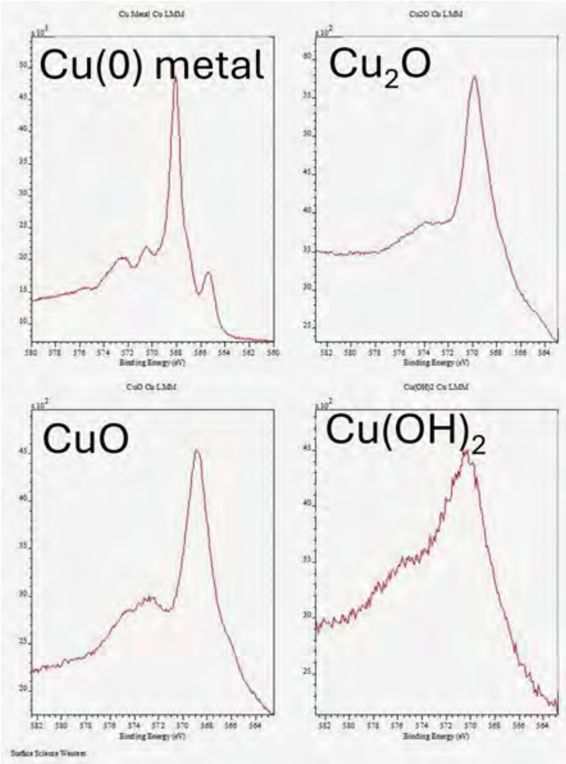

Figure 4.36: CuLMM Auger spectra for Cu metal (top, left), Cu_2O (top, right), CuO (bottom, left), and $Cu(OH)_2$ (bottom, right) (taken from M.C. Biesinger, unpublished data (2013)).

Table 4.2: Fit constraints of the Cu species reference spectra

Cu species	position constrains / eV
Cu metal	568.0 - 567.8
Cu_2O	569.9 - 569.7
$Cu(OH)_2$	570.3 - 570.1
CuO	569.0 - 568.8

binding energies and are not distinguishable from one another. Therefore, no deconvolution of the Cu2p peaks was performed. Instead, the CuLMM Auger spectra were investigated using the method described by Biesinger [96].

The shape of the Auger spectra is distinct for every Cu species as can be seen in Fig. 4.36. It depicts the Auger spectra for the pure copper species, metallic copper, Cu_2O, CuO, and $Cu(OH)_2$. Besides their shape, the binding energy of the spectra is very characteristic. The reference spectra were obtained from Biesinger and are CuLMM Auger spectra taken from pure copper species samples.

To calculate the concentration, the CuLMM spectra were fitted in CasaXPS [139] with their fitted area corresponding to their concentration. The fit constraints are shown in Tab. 4.2. Because the reference spectra had a fixed width of 16 eV, all Auger spectra were fitted for the range of 563 eV to 579 eV. Measurement and reference are both corrected with a linear background.

When a sample contains multiple Cu species, the resulting Auger peak shape is considered to be a superposition of the reference spectra for each species. This approximation introduces an uncertainty for heterogeneous compositions of copper species, because the background for the Auger spectra changes for composite states compared to the pure reference spectra. The mixing of different oxides is therefore the most significant contributor to the uncertainty of the CuLMM fitting. Multiple measurements resulted in a 10% deviation between samples, although this was dependent on the heterogeneity of the species mixture. Additionally, due to the uncertainty of the fitting procedure, it is advised not to consider small contributions of under 5%.

4.3.2 Copper Surface Modification

The analysis detailed above allows for a quantitative investigation of XPS measurements for treated samples. The following chapter analyses the effect of the combined laser-plasma treatment on the chemical surface composition in comparison to untreated and laser-structured copper thin film samples.

As discussed in the previous chapters, a jet-to-surface distance of 5 mm was chosen. With an increase in the laser energy, the influence of the gas flow cooling on the sample could be minimized. Furthermore, $O_2(a^1\Delta_g)$ reaches a density of $4 \cdot 10^{20}$ m^{-3}, which is close to the approximated atomic oxygen density of $3.5 \cdot 10^{20}$ m^{-3} [55] at a distance of 5 mm. It is therefore plausible to assume that the conditions described by Gusakov *et al.* are favorable for CuO formation.

The laser contributes energy to the surface by localized heating. Gusakov *et al.* [28] demonstrated that oxygen absorption into copper surfaces increases with temperature. It should be noted, however that in their study lower temperatures favored the formation of CuO, whereas at higher temperatures predominantly Cu_2O was produced. During laser irradiation, the melting temperature of copper at 1357 K is clearly exceeded, which is far above the temperature range investigated by Gusakov *et al.*. After the pulse, the irradiated spot cools down rapidly, solidifying the copper. Thus, following the pulse, the temperatures in the laser spot may enter a regime more favorable for CuO formation, while still being sufficiently high to enhance oxygen absorption into the surface.

While extended treatment times could increase the CuO fraction, the applicable range of irradiation times is limited by the laser. Too short an exposure does not produce the required surface structuring, whereas prolonged irradiation leads to material ablation, which interferes with controlled chemical surface modification.

Therefore, treatment times of 5 s and 10 s were chosen. While 10 s was the upper limit for the laser irradiation duration before damaging the surface, 5 s was chosen as a midpoint to the untreated samples, but still offered long enough irradiation time for the PLIDS formation. Before a treatment, the laser and jet effluent were aligned on the same point. To minimize the influence that multiple plasma treatments could have on a single sample, a new sample was chosen for every spot. After a treatment, the samples were directly put into the XPS device to minimize deterioration in the atmosphere. Multiple measurements

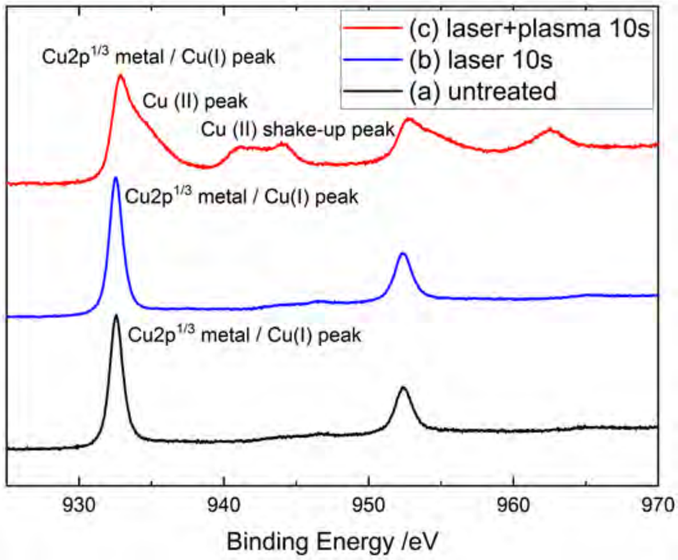

Figure 4.37: XPS Cu2p spectra of (a) the untreated Cu surface, (b) the laser-treated surface for 10 s, and (c) the simultaneous treatment with plasma and laser for 10 s.

were performed for treatment times of 10 s and 5 s, as well as for untreated thin films.

Fig. 4.37 displays the Cu2p spectra of the untreated Cu surface, a laser-treated surface, and a surface subjected to combined plasma and laser treatment, each for 10 s. The peak at a binding energy of approximately 932-933 eV indicates that the surface is primarily composed of the Cu(I) species Cu_2O and metallic copper. For both the untreated and laser-treated surfaces, only the Cu (metal)/Cu(I) peaks of the $Cu2p_{1/2}$ and $Cu2p_{3/2}$ are present. The XPS spectra of the laser-treated surface show no significant differences in the Cu2p (Fig. 4.37), CuLMM (Fig. 4.38), or O1s (not shown) regions compared to the untreated surface. Thus, it can be concluded that laser irradiation for surface structuring does not have a lasting effect on the chemical composition of the copper surface.

Applying plasma treatment simultaneously with laser irradiation induces a pronounced change in the oxidation state of the copper surface. In the Cu2p spectrum, the emergence of a shoulder peak at a binding energy of 934 eV can be observed. For the surface treated with both laser and plasma, broad features appear at 941-944 eV and 961-964 eV. These so-called shake-up peaks of the Cu2p region arise from ion excitations following X-ray photoionization, which reduce the kinetic energy of the emitted electrons. Such features are typically observed in paramagnetic materials, in this case corresponding to Cu(II) species, namely CuO and $Cu(OH)_2$. These oxidation states are absent in both the laser-only and untreated samples, clearly demonstrating the role of the plasma treatment. Since the binding energies of metallic copper and Cu_2O are indistinguishable in the Cu2p spectra, CuLMM Auger spectra were employed for quantitative analysis.

Fig. 4.38 shows the Auger spectra of the untreated surface and the surface treated with both laser and plasma for 10 s, to show the difference in the peak shape for different copper species ratios. The initial XPS spectra were fitted using a superposition of the reference spectra for the different copper species. For the untreated CuLMM spectrum, a double-

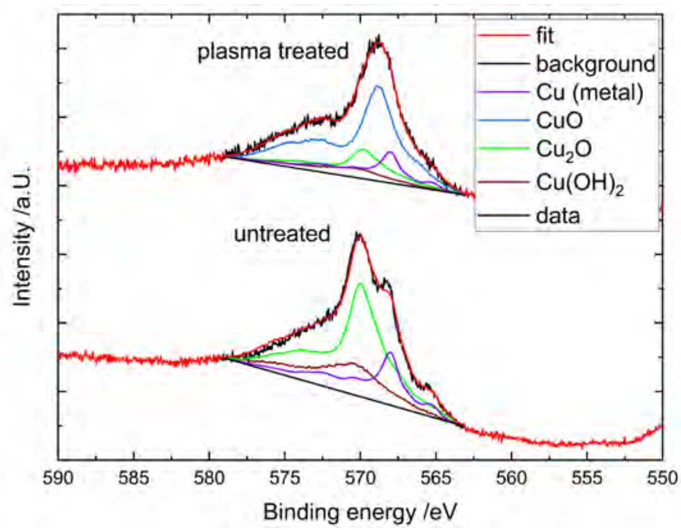

Figure 4.38: XPS CuLMM Auger spectra of the untreated Cu surface (bottom) and simultaneous treatment with plasma and laser for 10 s (top).

peak structure can be observed, resulting from the copper metal and Cu_2O reference spectra. The binding energies of these species are wide enough apart (ca. 2 eV) to make them distinguishable. The $Cu(OH)_2$ Auger reference spectra also contribute to the fit, although the Cu2p spectra do not indicate the presence of Cu(II) species ($Cu(OH)_2$), due to their lack of a shoulder peak at 934 eV and the missing shake-up peak. The presence of $Cu(OH)_2$ is not an effect of the plasma, as there are no OH species present, but could be a result of impurities in the vacuum chamber during production or due to the oxidation of treated samples when they come into contact with ambient air during transfer to the XPS. Such a high concentration is still questionable, as it would be visible in the Cu2p spectra through shake-up peaks. The $Cu(OH)_2$ concentration is still shown for the sake of completeness.

The overestimated copper hydroxide concentration was mainly observed for samples with a heterogeneous copper species composition. The elevated copper hydroxide concentration may be an artifact of the fitting procedure, since binding energies can shift due to the varying background of heterogeneous compositions, which cannot be fully described by a simple superposition of reference spectra. This effect could bias the fit towards copper hydroxide to compensate for mismatches between the fit and measurement at higher binding energies. However, the fitting routine mostly uses the $Cu(OH)_2$ Auger peak to fit the left flank. If the $Cu(OH)_2$ were left out, the peak with the next highest binding energy would be used to compensate, which is Cu_2O. The fitting of $Cu(OH)_2$ has therefore no significant impact on the more interesting CuO concentration. Another possible influence could be the silicon substrate or the nanoparticle morphology. It has been shown that interfaces between different materials can shift the observed binding energies [140]. X-rays may also alter the chemical composition through degradation of copper species [141], although given the relatively short acquisition times, this effect is unlikely to play a significant role here.

Fig. 4.39 shows the copper species composition for different treatment conditions and times compared to the untreated sample. For the untreated sample, the surface concen-

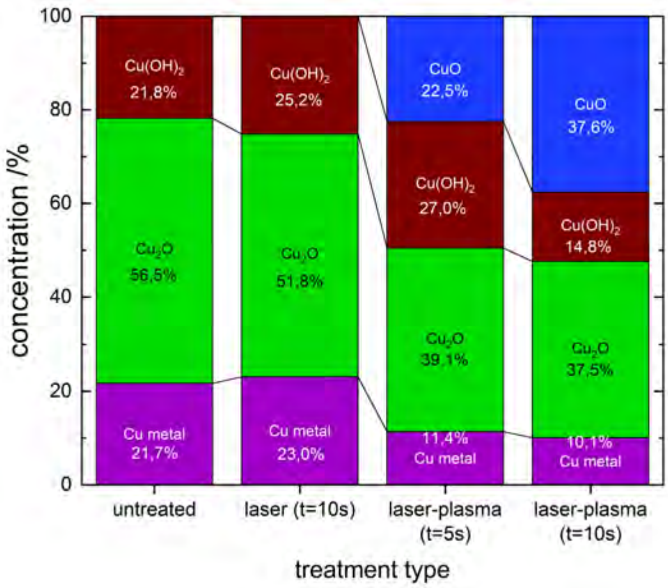

Figure 4.39: Concentration of the oxides CuO and Cu_2O, the hydroxide $Cu(OH)_2$ and metallic Cu for various treatment types and al aser fluence of 3.5 J/cm^2.

tration of Cu(I) oxide is approximately 57%, with only a slight deviation of 5% measured across multiple samples. The high oxide concentration is probably an effect of the surface oxidation of the thin copper layer. For the thin layers, most of the layer is oxidized, leaving only a small fraction of metallic copper underneath.

A similar composition is observed for the concentrations of metallic copper and copper hydroxide, with the former at approximately 20% and the latter at about 23%. This composition changes only slightly under laser irradiation. In this case, metallic copper and copper hydroxide increase marginally to 23% and 25%, respectively, while Cu_2O decreases to 52%. These variations remain within the uncertainty margin of the composition and support the claim from the Cu2p spectra that the laser irradiation alone does not influence the chemical composition.

When comparing the distribution of copper species between untreated or laser-only samples and those treated with laser and plasma for 5 s, a clear reduction of metallic copper from 22% to 11% can be seen, along with a decrease in Cu_2O from 53% to 39%. This reduction corresponds closely to the observed increase in CuO to 23%. It therefore appears reasonable that CuO forms primarily through further oxidation of metallic copper and Cu_2O. The $Cu(OH)_2$ fraction also rises to 27%. This may reflect an oxidation process, since it is also a Cu(II) species, but it could equally result from higher uncertainties due to the greater heterogeneity introduced by the presence of CuO.

For a treatment time of 10 s, the concentration of metallic copper remains almost unchanged compared to the 5 s case at about 10%, while CuO increases further from 23% to 38%. The $Cu(OH)_2$ concentration, however, decreases considerably from 27% to 15%, while Cu_2O and metallic copper remain nearly constant at 38% and 10%, respectively. From 5 s to 10 s treatment, $Cu(OH)_2$ is therefore converted mainly into CuO rather than metallic copper or Cu_2O. It would be expected that metallic copper and Cu_2O are completely oxidized before $Cu(OH)_2$ begins to decrease, as the latter is a Cu(II) species and should be comparatively more stable with respect to oxidation. The lower $Cu(OH)_2$ concentration may also be explained by the higher CuO content, which reduces the heterogeneity of the sample composition. This, in turn, shifts the peak toward lower binding energies, reducing discrepancies between the fit and the measurement on the high binding energy side.

4.3.3 Summary & Concluding Remarks

This study investigated a novel approach to catalyst functionalization by combining reactive species from an atmospheric pressure COST jet with the energy input of a pulsed laser. Thin copper films, deposited via high-power pulsed magnetron sputtering on silicon wafers, served as substrates. The thin copper layer is mostly oxidized due to contact with the ambient atmosphere.

XPS measurements revealed that laser irradiation left the surface composition largely unchanged compared to untreated samples, with predominantly Cu(I) oxides and minor hydroxide presence. In contrast, combined laser-plasma treatment produced Cu(II) species (CuO), with their concentration increasing with treatment time. This allows controlled tuning of the Cu_2O / CuO ratio. As Gusakov *et al.* [28] have shown, atomic oxygen alone cannot produce CuO in high quantities. It is therefore plausible that the generated $O_2(a^1\Delta_g)$'s flux to the surface by the COSt jet is indeed high enough to prevent counter oxidation reactions.

These findings demonstrate that the laser effectively structures the surface, while the plasma simultaneously modifies the chemical composition in a controlled manner. The ability to tune the CuO to Cu_2O ratio is a distinctive feature of this approach and may be of interest for further studies on complex copper-based catalysts. The high amount of CuO promises a high selectivity towards ethylene production. These findings suggest a potential pathway toward more robust and efficient catalyst materials. However, further measurements are needed to validate the stability and efficiency under CO_2-RR.

4.4 fs-Laser Surface Structuring

The following measurements were performed in collaboration with the chair "Ultrafast lasers and photonics" of Clara Saraceno, together with the PhD Samira Mansourzadeh.

Inducing surface structures on bulk materials is quite challenging with ns-lasers because their long pulse time primarily contributes to surface heating, rather than the unique laser-surface interaction facilitated by ultra-short pulses. To this end, the influence of fs-lasers on copper thin films as well as bulk materials, like copper foil and thicker layers, were investigated to be compared to those of the ns-laser. Due to the short collaboration time with the fs-laser setup, only a few laser parameter variations could be investigated. This is very unfortunate since the fs-laser had a much broader parameter space for successful

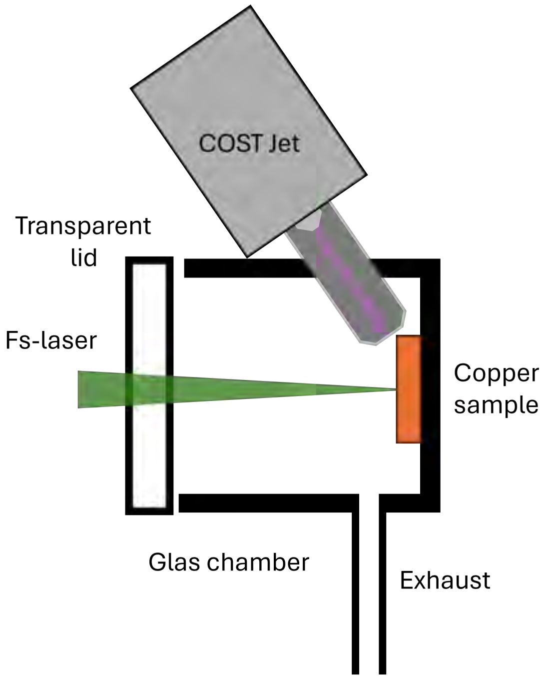

Figure 4.40: Schematic of the portable glass chamber for the fs-laser treatment.

surface structuring. Additionally, a chemical composition analysis after a combined laser-plasma treatment of the bulk materials was conducted.

fs-Laser Setup

As the fs-laser was located at the photonics and ultrafast lasers chair of C. Saraceno, a portable reactor had to be designed in which the laser treatment could be conducted in a controlled atmosphere.

Fig. 4.40 depicts the schematic of the portable glass chamber used to get a controllable atmosphere. The chamber was sealed with a transparent lid through which the laser could be focused on the sample. The exhaust was connected to a long pipe, which reduced the backflow of air into the system. The COST jet could be mounted on the side of the glass chamber at an angle of roughly 30°. Due to construction constraints, it was not possible to align the COST jet at the 45° angle of the ns-laser setup. The entry was sealed with a 3D-printed adapter and clay. The COST jet and the fs-laser were aligned onto the same spot on the copper sample.

The fs-laser (TruMicro 2000 from Trumpf) had a maximum power of 18 W with an initial wavelength of 1030 nm, a repetition rate of up to 400 kHz, a pulse duration of 300 fs and a pulse energy of 45 µJ (at 400 kHz). To achieve a comparable wavelength to the previous measurements, the laser was frequency-doubled to 530 nm, which resulted in a maximum power of 7 W. Preliminary measurements revealed that a beam diameter of 600 µm yielded the best results for surface structuring. The beam diameter was measured by a beam profiler, which calculated the half-width ($1/e$) of the Gaussian beam. Laser energy and repetition rate could be tuned independently. For surface structuring, successful laser powers were between 4 and 5 W. From these laser parameters, a laser fluence of 18 mJ/cm^2 can be calculated, which is much lower than the 3.5 J/cm^2 of the ns-laser. Unfortunately, the lid caused some problems with the laser-surface interaction. No surface structures could be observed while the lid was on. Here, either the absorption or scattering of the laser light was too high, so that even an increase in the laser power could not compensate for it. Another option could be that the lid shifted the focal point of the laser, resulting in a deviation from the optimal 600 nm beam diameter. Due to time constraints of the collaboration, no working laser parameters were found, so that the lid had to be removed. Therefore, only the gas shielding of the COST jet effluent could provide protection from the ambient atmosphere during the treatment.

fs-Laser Surface Structuring

Fs-laser surface structuring was investigated on three different samples. copper thin films of 10 nm thickness, thicker copper layers of 100 nm, and copper foil. Copper thin films and the copper foil can directly be compared to the previously studied ns-laser-induced surface structures. For the 100 nm copper layers, the previously employed ns-laser proved unreliable in surface structuring. Therefore, no successful laser parameters were found for thicker copper layers and measurements were conducted for 10 nm layers.

Besides a comparison to the ns-laser results, these measurements can also be used to compare the foil to thicker films to rule out possible effects of the different materials on the treatment. The foil was not electropolished as the optimal conditions for that process were not yet refined during the collaboration.

To investigate the generated LIPSS, SEM images were taken and analyzed using the Gwyddion software, as explained in the Bulk Material Surface Structuring chapter. It allowed to conduct a 2D Fast-Fourier-Transformation (2D-FFT), which highlights the periodicity of periodic structures in a 2D image. The resulting phase space plots the intensity of recurring periodic structures, where their distance from the origin represents their periodicity Λ and their angle to the x- or y-axis indicates their orientation in real space. With $d = \frac{1}{\Lambda}$, the mean distance between these structures can be calculated.

Fig. 4.41 (a) shows the SEM image of the fs-laser-induced LIPSS patterns on a 10 nm copper film using a laser power of 4.1 W, an irradiation time of 10 s, a frequency of 200 kHz and a beam diameter of 600 µm. The LIPSS pattern is well-defined but appears quite different from the LIPSS observed for the ns-laser. Instead of the sharp "wave"-like pattern, the LIPSS for fs-lasers are more "roundish" and seem to protrude from the surface. Fig. 4.41 (b) depicts the 2D-FFT with the red areas indicating the LIPSS pattern in Fourier space. The radial distance from the origin of these structures gives a periodicity of 1.7 µm^{-1} which corresponds to a mean pattern distance of 588 nm. This is slightly larger than the wavelength of the laser at 532 nm. Possible errors are the rather "blurry" distribution in Fourier space, which hints at an inhomogeneous pattern spacing, facilitated by surface irregularities. Another reason might be the laser alignment. As shown in [91], the LIPSS periodicity depends on the incident angle of the laser, with angles greater than

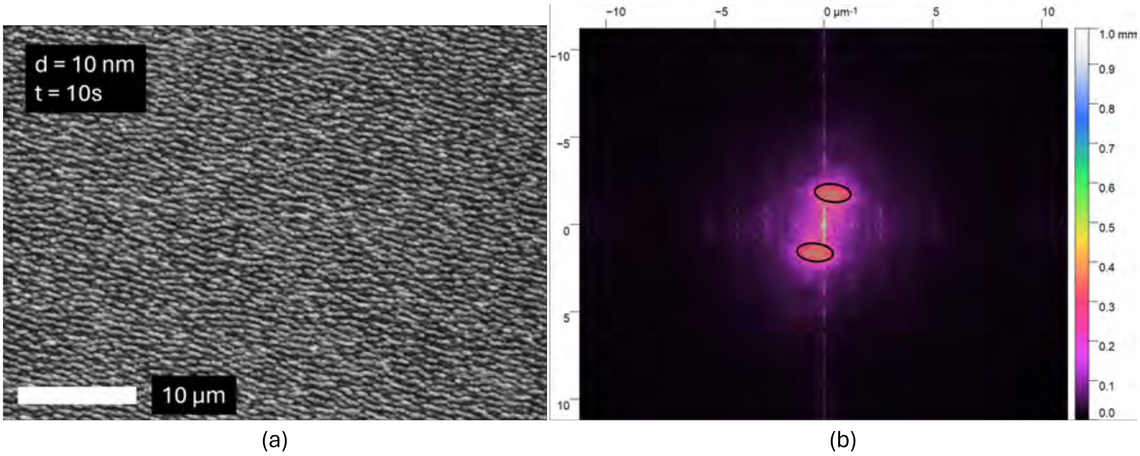

Figure 4.41: (a) SEM image of 10 nm copper film structured by the fs-laser using a laser power of 4.1 W, irradiation time of 10 s, frequency of 200 kHz and a beam diameter of 600 µm. (b) 2D-FFT of the SEM image. Red area indicates the most prominent periodic pattern with a periodicity of 1.7 μm^{-1} resulting in a LIPSS pattern length of 588 nm.

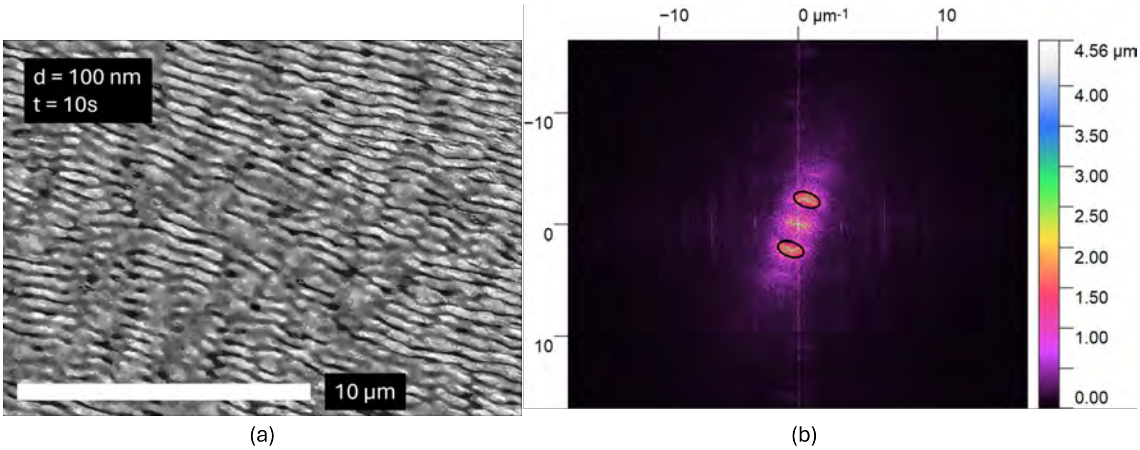

Figure 4.42: (a) SEM image of 100 nm copper film structured by the fs-laser using a laser power of 5.1 W, irradiation time of 10 s, frequency of 400 kHz and a beam diameter of 600 µm. (b) 2D-FFT of the SEM image. Red area indicates the most prominent periodic pattern with a periodicity of 3.3 μm^{-1} resulting in a LIPSS pattern length of 304 nm.

90° leading to a lower periodicity and, therefore, a longer pattern spacing. Taking these errors into account, the structures can still be considered LIPSS of the LSFL type-I due to their pattern distance being close to the laser wavelength.

In Fig. 4.42 an SEM image of the fs-laser-induced LIPSS patterns on a 10 nm copper film using a laser power of 5.0 W with an irradiation time of 10 s, a frequency of 400 kHz, and a beam diameter of 600 µm are depicted. The LIPSS patterns are clearly visible but seem to “melt” into each other, which could indicate that the laser power was set a bit too high. Nevertheless, the exhibited structure resembles that observed for the 10 nm layer fs-laser. The 2D-FFT image shown in Fig. 4.42 (b) depicts clear periodic structures at a periodicity of 3.3 μm^{-1}, which equates to a pattern distance of 304 nm. This pattern distance is significantly shorter than the laser wavelength and the LIPSS observed on the thin films. The LIPSS here appear to be HSFL of the type-II, which can be significantly shorter than the laser wavelength, as predicted by the Sipe theory.

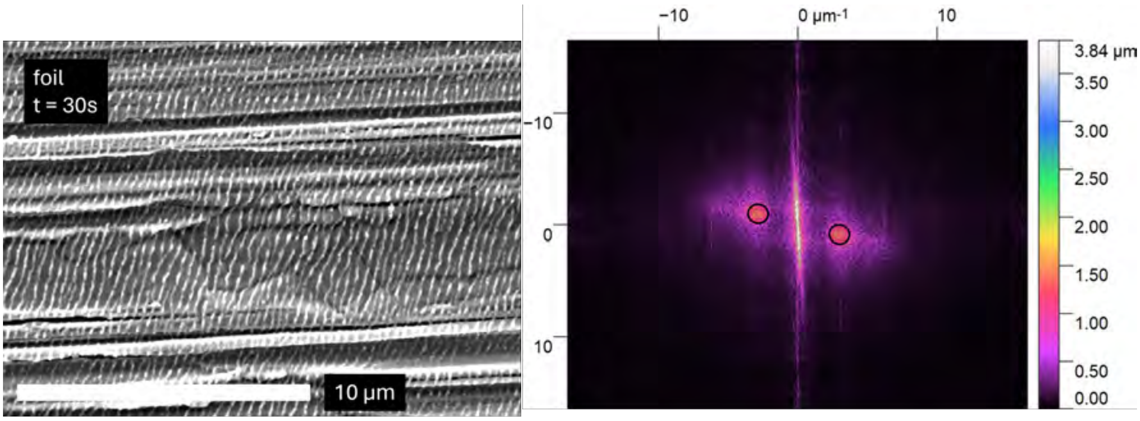

(a) (b)

Figure 4.43: (a) SEM image of the copper foil structured by the fs-laser using a laser power of 5.1 W, irradiation time of 30 s, frequency of 400 kHz and a beam diameter of 600 µm. (b) 2D-FFT of the SEM image. Red area indicates the most prominent periodic pattern with a periodicity of 2.5 μm^{-1} resulting in a LIPSS pattern length of 406 nm.

Fig. 4.43 (a) shows a SEM image of the LIPSS pattern produced by a fs-laser irradiation on the copper foil for a laser power of 5.0 W, irradiation time of 30 s, frequency of 400 kHz and a beam diameter of 600 µm. The appearance of the produced LIPSS differs from that of the structures generated on the copper films. Here, the LIPSS seem to protrude from the foil's surface. The original surface structure appears to be largely intact. The irradiation time was also longer than for the thin film. The different shape of the LIPSS could hint at a different formation mechanism when fs-lasers are involved. While the ns-laser mostly restructures the surface by an interference-driven absorption variation on the surface, fs-lasers are able to produce patterns by laser oxidation, generating an ordered oxide structure [142, 143]. The 2D-FFT depicted in 4.43 (b) is quite noisy but shows a clear intensity maximum at the red areas. The noise in Fourier space is most likely caused by the high surface roughness of the copper foil. The LIPSS pattern spacing of 406 nm is again much smaller than the laser wavelength. This may hint again at HSFL-II, but it may also be a feature of the different formation mechanism, especially since the pattern spacing is different from that of even the HSLF-II patterned 100 nm copper layer.

To summarize, the surface structuring with the fs-laser has a significantly larger parameter space for successful surface structuring compared to the ns-laser, making its application considerably easier. However, the generated structures are much more heterogeneous than the mostly uniform LIPSS patterns observed for the ns-laser. The LIPSS patterns generated with the fs-laser differ in periodicity, pattern, and possibly formation mechanism. This is no surprise, considering the much broader parameter space of laser power, frequency, and treatment time for successful LIPSS formation. Especially for the copper foil, a controlled atmosphere could significantly influence the generated structures. It was speculated that they are formed from the oxidation of the surface. When a helium atmosphere is employed, this mechanism may be significantly slower or even impossible, as the oxygen concentration is substantially reduced. Nevertheless, extended studies may reveal more predictable and comparable structuring of the bulk materials with the fs-lasers.

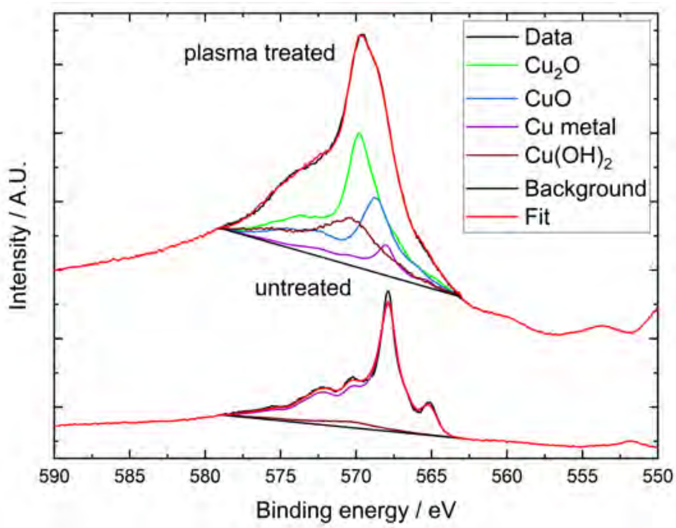

Figure 4.44: XPS CuLMM Auger spectra of the Cu foil for an untreated sample (bottom) and a combined laser-plasma treatment of 30 s (top).

Chemical Composition Analysis of Bulk Materials for a fs-Laser Treatment

To investigate the influence of a combined laser-plasma treatment using the fs-laser, the initial surface composition of the copper foil must be known. Furthermore, a comparison to the 10 nm copper thin layers is needed to investigate if the copper deposition has an impact on the initial surface composition. Assuming the compositions do differ, analysis of the thicker 100 nm copper layers can rule out an influence of the copper deposition method. Instead, the thickness of the copper layer may play a more important role.

The samples were treated in accordance to the method used for the thin films. However, as seen in the preliminary measurement for LIPSS generation, the laser irradiation time was significantly higher with fs-pulses compared to ns-pulses. To increase the copper oxide amount, longer treatment times are more favorable. Therefore a maximum treatment time of 30 s was used with 15 s as a midpoint. All samples were treated by a fs-laser with a power of 5.1 W at a frequency of 400 kHz and a beam diameter of 600 µm.

Due to the interference of the laser with the lid of the portable chamber, which prevented LIPSS structuring, the lid was removed. The results presented here are therefore only shielded by the gas flow of the COST jet effluent and not in a controlled atmosphere.

Fig. 4.44 compares the Cu Auger spectra of the untreated foil with a combined laser-plasma treatment of 30 s. The fitting of the different copper oxides was done in a manner analogous to the thin layers. The Auger spectrum of the untreated foil at the bottom of Fig. 4.44 resembles mostly the metallic copper Auger reference spectrum. Therefore, a high amount of metallic copper is present in the foil. The upper Auger spectrum is an example of how the surface composition changes after a 30 s treatment. The spectrum of the treated sample contains a mix of the reference spectra for metallic copper, Cu_2O $Cu(OH)_2$ and CuO. Compared to the untreated case, the amount of metallic copper is considerably reduced. Instead, mostly CuO_2 and CuO are visible. The treatment oxidizes the surface of the bulk material and is capable of producing CuO, as observed for the thin

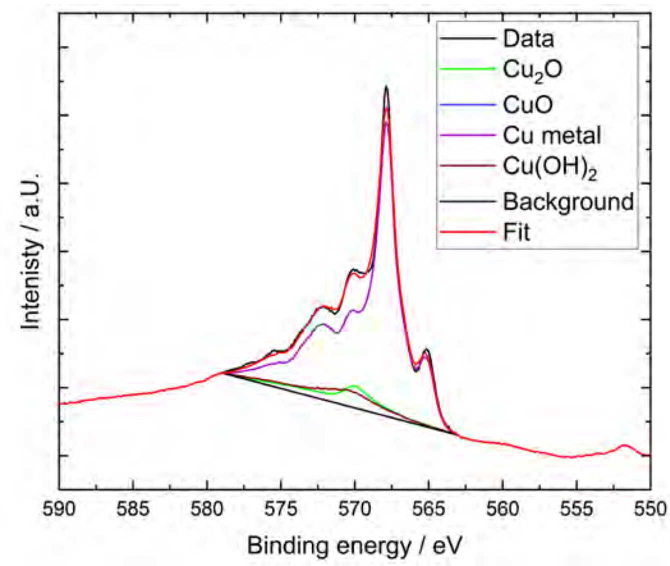

Figure 4.45: XPS CuLMM Auger spectra of a untreated 100 nm copper layer on silicon wafer.

layers.

The untreated Auger spectrum differs considerably to the thin layers, which had a concentration of roughly 40% Cu_2O even in the untreated case. Copper oxide is mostly a result of the oxidation of the sample surface in air. For the thin layer samples, the copper layer is almost completely oxidized, leading to a high CuO_2 ratio. This is partly due to surface oxidation, but could also result from oxygen that is bound to the silicon wafer prior to the HIPIMS deposition. For bulk copper, on the other hand, only the thin surface layer is oxidized, leaving a high volume of metallic copper underneath. As the XPS has an observation depth higher than the oxide layer, it is able to detect the metallic copper underneath the oxide layer. That is not possible for the thin layers, as most of the layer is oxidized here, leaving no metallic copper. The small amount of metallic copper in the upper Auger spectrum for the treated sample indicates that the reactive species of the plasma penetrate at least as deep as the detection depth of the XPS.

Another reason for the difference in the surface composition between untreated foil and thin layers could be that they generally possess different chemical compositions. To investigate this possibility XPS measurements of 100 nm copper layers were performed. These represent a bulk material but are synthesized with the HiPIMS chamber, also used for the thin layer deposition. They should therefore share a similar chemical composition.

Fig. 4.45 shows the untreated copper Auger spectrum of the 100 nm layer. It contains a high amount of metallic copper as observed in the foil. The initial chemical surface composition therefore appears not to differ between the synthesized layers and the copper foil, but rather depends solely on the layer thickness. This indicates that the high Cu_2O concentration in the thin layers is an effect of the oxide layer ratio to the copper layer thickness. The high amount of metallic copper in the untreated samples also provides an opportunity to investigate the formation of the different copper oxides in more detail.

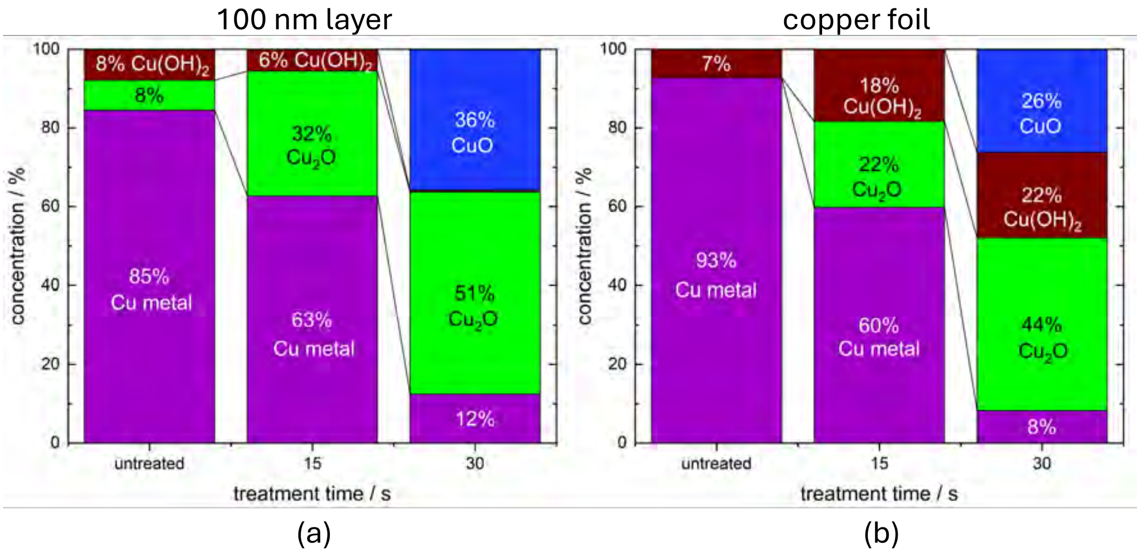

Figure 4.46: Concentration of the copper oxides CuO and Cu2O, the hydroxide Cu(OH)2 and metallic Cu depending on combined laser-plasma treatment time for (a) 100 nm copper layer on silicon or (b) copper foil.

Fig. 4.46 shows the concentration of the different copper species in dependence on the combined laser-plasma treatment time for (a) the 100 nm copper layer and (b) the copper foil. Both start out with a high amount of metallic copper of 85% and 93%. Additionally, both also contain a small amount of $Cu(OH)_2$ of 7-8%. This is most likely due to the fitting procedure as described for the thin layers. As the reference spectra do not fit perfectly to the measured data, a small shift in the binding energy leads to a compensation of the left flank of the spectrum through an increase in the $Cu(OH)_2$ concentration. The 100 nm layer also contains 8% of CuO_2, not observed in the foil. Surprisingly, the foil does not contain any copper oxides, although it is known from the thin layers that most of the top oxide layer should be CuO_2. Its absence in the foil is most likely due to an uncertainty in the fitting, as described in the XPS analysis chapter. It could therefore be assumed that it is mostly Cu_2O, rather than $Cu(OH)_2$. Additionally, it is challenging to distinguish between different oxide species at concentrations below 5%, which may be the case for the foil. Even the 8% of the 100 nm layer is only slightly above this threshold. Nevertheless, the main takeaway from the untreated samples is that the bulk copper materials contain a high amount of metallic copper, with only small contributions from the oxide layer.

After a combined laser-plasma treatment time of 15 s for both the 100 nm layer as well as the foil, the concentration of metallic copper is greatly reduced and mostly converted to Cu_2O. For the foil, the $Cu(OH)_2$ concentration increased too, which could be an overestimation. The ratio of metallic to oxidized species increased regardless. Remarkably, no CuO is present yet. Compared to the ns-laser thin film treatment, an increase in CuO was expected. For the ns-laser treatment, 5 s already produced a concentration approx. 20%.

After a treatment time of 30 s, the amount of metallic copper is greatly reduced to 12% and 8%, respectively. For the 100 nm samples, the concentration of CuO_2 increases to 51%, which is close to the 44% of the foil and comparable to the amount that was measured for the treated thin layers of approx. 40%. In the case of the foil, the concentration of CuO_2 is reduced due to the higher amount of $Cu(OH)_2$. It should be noted that the concentration of $Cu(OH)_2$ did not increase much from the 15 s treatment to the 30 s, indicating that the plasma treatment may, in fact, not produce $Cu(OH)_2$. Instead, it is a product of the fitting routine, as was explained for the thin layers. CuO can be observed in the sample with a concentration of 36% for the deposited layer or 26% for the foil. The concentration for the 100 nm layer is higher than for the foil, which is a result of the foil's higher $Cu(OH)_2$ content.

The two bulk materials exhibit very similar behavior under the fs-laser-plasma treatment. They differ slightly in their $Cu(OH)_2$ content, which increases for the foil with increasing treatment time, while remaining constant for the 100 nm layer before disappearing after 30 s of treatment. However, its detection might introduce uncertainty into the fitting routine. Both materials produce no CuO within the first 15 s of treatment and mostly oxidize the metallic copper to Cu_2O. After a treatment of 30 s, the bulk materials contain a comparable amount of CuO. It should be noted that producing CuO in bulk materials takes longer than in thin layers. There, CuO was already visible in the spectra after a 5 s treatment. This may indicate that CuO is produced by further oxidizing Cu_2O, as hypothesized for the thin layers, rather than being directly produced from metallic copper. The increased time for the production of CuO is therefore linked to the low amount of Cu_2O in the untreated bulk materials. First, metallic copper oxidizes to Cu_2O, and then Cu_2O gets converted to CuO. Longer treatment times might therefore be able to increase the CuO content further.

Under the fs-laser irradiation, the bulk materials proved to be much more resilient to the energy input of the laser and did not suffer from ablation. The possible treatment time is not as limited as for the ns-laser thin film treatment. Furthermore, the treatment of the bulk materials could not be conducted in a controlled atmosphere as described in the fs-laser setup. Nevertheless, the treatment proved to be very consistent. This highlights the copper foil as a potential scale-up for the copper thin layers without compromising a reliable tuning of the surface composition.

4.4.1 Summary and Concluding Remarks

To provide a more durable material for further investigations under catalytic conditions, copper bulk materials were investigated. To exclude the influence of the layer deposition by the HiPIMS chamber on the chemical surface composition, 100 nm layers were compared to a copper foil. Both were investigated for their behavior under laser structuring and chemical composition before and after the combined laser-plasma treatment.

SEM images were taken to demonstrate that successful LIPPS structuring on bulk materials can be achieved using the fs-laser. The observed surface structures were analyzed using 2D-FFT. The resulting periodic surface structures were examined in terms of their periodicity. It was observed that the generated surface structures were indeed LIPSS. However, their periodicity varied for the different copper samples. For the thin layers, most LSFL were observed, matching the structures for the ns-laser treatment. Bulk materials, on the other hand, produced HSFL recognizable at their periodicity below the laser wavelength. In general, the fs-laser seemed to have a much broader parameter space for successful LIPSS formation. Ultimately, further measurements will determine whether a broader parameter study on fs-lasers would enable more control over the resulting laser-induced structures.

The chemical composition of the two bulk materials 100 nm copper layers and the foil, were compared to the thin layer samples. Using XPS measurements, it was found that the bulk materials contained a higher amount of metallic copper compared to the thin layers. This was attributed to their thickness. The thin oxide layer covering the samples constitutes only a small fraction of the bulk materials, while the thin layers were almost completely oxidized. Furthermore, the bulk materials were very comparable in their initial surface composition, which rules out the effects of the synthesis method on the chemical composition. After a plasma treatment of 15 s, the bulk materials exhibited an increase in Cu_2O. Notably, no CuO is produced for shorter treatment times, as was the case for the thin layers. Only after a treatment time of 30 s CuO is produced. It was concluded that CuO is produced by further oxidation by Cu_2O. Therefore, no CuO is present after 15 s as Cu_2O had to be produced first. These findings align well with the mechanisms proposed by Gusakov *et al.*. It should also be noted that the treatment with the fs-laser was very resilient to atmospheric conditions, as all experiments had to be conducted in ambient atmosphere. It was able to produce clear results for the CuO concentration increase after treatment times of 30 s.

5 Conclusion and Outlook

This study presented a novel approach to catalyst synthesis by combining irradiation from a laser and reactive species from a COST jet. To prove the concept, the study looked into copper as an example catalyst system for the CO_2-RR. Of special interest was the generation and control of the copper oxide concentration, which has been shown to have beneficial effects on catalyst performance. Answers to the initial research questions are given below to conclude the most important findings of this study.

Does the COST jet produce reactive molecular oxygen species in sufficient densities to facilitate the formation process of Cu(II) copper oxides as proposed by Gusakov *et al.*? What is ultimately the flux that reaches a sample?
Based on the study by Gusakov *et al.* the most important reactive species for the oxidation of copper were identified. Atomic oxygen is the main oxidative agent, but high densities at a copper surface also facilitate "counter" oxidation reactions which reduce the Cu(II)-species CuO back to Cu_2O or even metallic copper. Gusakov concluded that molecular oxygen species are needed to prevent these "counter" oxidation reactions. Atomic oxygen was already studied extensively in previous works. Therefore, this study concentrated on the density of reactive molecular oxygen species. It was discovered that the density of $O_2(a^1\Delta_g)$ in the effluent is in the same order of magnitude as atomic oxygen at a distance of 8 mm in front of a surface for a helium and 0.5% oxygen admixture. For atomic oxygen a flux of $\Gamma_{O_2(a^1\Delta_g)} = 2.1 \cdot 10^{19}\,m^{-2}s^{-1}$ was measured, while the $O_2(a^1\Delta_g)$ flux resulted in $\Gamma_O = 6.6 \cdot 10^{19}\,m^{-2}s^{-1}$. The reactions proposed by Gusakov *et al.* are therefore a likely mechanism for the CuO formation for the chosen parameters. $O_2(b^1\Sigma_g^+)$ on the other hand is quickly quenched outside the plasma and therefore does not contribute strongly to the proposed reactions by Gusakov *et al.*.

How do the different species interact with each other, and what are the optimal plasma parameters?
Investigated were $O_2(a^1\Delta_g)$, $O_2(b^1\Sigma_g^+)$, and ozone by optical emission and absorption spectroscopy. For their optical detection, a gas flow cell was necessary. The more complicated effluent geometry prompted a comparison with two simulations: a pseudo-1D plug-flow simulation and a 2D-fluid simulation. This work focused on highlighting the interdependency of these species, with ozone serving as the primary quencher. Its density must be known to obtain a realistic estimate for the two excited molecular oxygen species. A comparison between simulations and experiment revealed that the models overestimate the ozone density produced inside the jet, as well as in the effluent, which could be confirmed for multiple species. This led to a small deviation from the experimentally

measured densities for $O_2(b^1\Sigma_g^+)$ and $O_2(a^1\Delta_g)$. Further research should be conducted to obtain a more accurate estimate of important rate coefficients, such as those for surface reactions. From the experimental side, a more optimized flow cell might ease the modeling of the gas flow dynamics and reduce computation time. Especially lower volumes would greatly help the comparison to simulations. This must, of course, be considered in relation to emission intensity, as a lower volume also reduces the signal-to-noise ratio.

To reach a high CuO concentration in a sample, a high atomic oxygen density is necessary. The chosen admixture of 0.5% oxygen is beneficial, as it provided the highest amount of atomic oxygen. However, its density has to be equal to reactive molecular species. The decay rate of the different species in the effluent differs. Therefore, the distance to a sample is key. A smaller jet-to-surface distance gives a higher comparable atomic oxygen density. In contrast, the chosen distance of 5-8 mm gave a comparable density of atomic oxygen with $O_2(a^1\Delta_g)$, making it a good choice to facilitate the mechanism proposed by Gusakov *et al.*.

Which laser parameters are able to successfully induce nanoscale surface structures on copper, and which structures can be utilized best for specific applications?
To investigate laser surface structuring, multiple samples with different surface types were analyzed using SEM imaging. A threshold laser fluence of 3.5 J/cm^2 had to be exceeded for laser surface structuring to occur on copper. Depending on the chosen sample type, thin films or bulk materials, different surface structures could be induced.

PLIDS were investigated on thin films, and their size followed the linear thin-film hydrodynamic dewetting theory (TFH), providing a control mechanism for the nanoparticle size through the layer thickness. Nanoparticles of 20 nm diameter could be observed. However, even thinner layers than those employed in this study could be used to produce smaller particles.

LIPSS were produced on copper foil using a ns-laser. Generally, their generation required comparable laser energies to the PLID structuring. 2D-FFT revealed that the induced periodic structures had a periodicity matching the laser wavelength of approx. 560 nm. Another critical aspect for successful surface structuring was the surface roughness. Surface roughness had to be within the range of the laser wavelength. LIPSS could be produced on an unpolished surface. However, the produced structures were dominated by the initial surface morphology.

A fs-laser provided a further tool for laser structuring. It demonstrated high reliability in generating LIPSS due to its larger parameter space. The fs-laser required a significantly lower laser fluence to generate laser-induced surface structures of 18 mJ/cm^2. Furthermore, the fs-laser enabled the generation of HSFL, which offer the possibility to create structures below the laser wavelength, which is typically the limiting factor for the scale of the LIPSS structures.

What influence does the simultaneous plasma treatment have on the formation of laser-induced surface structures?
The influence of a gas flow on the PLIDS formation was studied using SEM imaging. It was discovered that the additional cooling provided by a continuous helium flow disrupted PLIDS formation. This effect could be compensated with a higher laser energy, though.

Do the laser-induced structures influence the chemical composition of the surface?
XPS measurements were conducted on samples with different treatment types, which showed that the laser alone provided no significant contribution to changing the surface composition under a controlled atmosphere. The induced nano-scale surface structures are therefore independent of the surface composition change. However, the laser may still contribute to a change in the surface composition. The laser irradiation heats the surface, which may facilitate the formation of copper oxides due to the excess energy.

Which copper oxides can be produced by the combined laser and plasma treatment and can their concentration be controlled?
The laser-plasma treatment was investigated to study its effects on the surface composition. Multiple samples were treated with the combination of laser and plasma under a controlled atmosphere. The initial surface composition for copper thin layers showed a high amount of Cu_2O, due to an oxide layer formed in contact with the ambient atmosphere, which left only a small amount of metallic copper. After varying treatment times of 5-10 s with the combined treatment, the copper layers exhibit an increasing amount of CuO. By varying the treatment time, it is therefore possible to change the ratio between Cu_2O and CuO from the initially high percentage of Cu_2O to up to 90% CuO. The hypothesis was made that CuO is produced by further oxidizing Cu_2O as suggested by Gusakov *et al.* [28]. This was supported by the investigation of copper bulk materials. Here, CuO was only observed after the treatment had already produced Cu_2O in the samples.

Can the findings be transferred to bulk materials?
Thin films provide an accessible system for investigation, but are generally unsuited for applications. Bulk materials are therefore more desirable. To this end, copper foils were investigated. The initial surface composition revealed a considerably higher concentration of metallic copper, which was attributed to the ratio between the oxide layer thickness formed in contact with the atmosphere and the penetration depth of the XPS analysis into the material. For thin layers, a high fraction is oxidized, resulting in a higher Cu_2O concentration. In bulk materials, on the other hand, the oxide layer constitutes only a small fraction of the XPS device's penetration depth. However, under the combined laser-plasma treatment with the fs-laser, the concentration of the copper oxides increased. It was discovered that firstly, metallic oxygen gets oxidized to Cu_2O. After the formation of Cu_2O, it can be further oxidized by the plasma species to CuO. Longer treatment times, therefore, lead to a higher CuO content. The synthesis technique could be applied to bulk materials, ensuring both surface structuring and control over surface stoichiometry. Additionally, the surface modification of bulk materials has proven to be quite resilient

under atmospheric conditions, which may make the process more accessible.

5.0.1 Future Measurements

Although stoichiometric changes can be observed in the synthesized surfaces, further investigation is still required. This study was not yet able to measure the changes in the catalytic performance of copper and how the synthesis process can be tuned to optimize selectivity and efficiency. Future measurements could investigate gas chromatography (GC) to determine the product composition of a CO_2-RR. This would enable the investigation of which surface structures and stoichiometries facilitate more efficient and selective copper surfaces.

Another important aspect of improving the setup is the synthesis time. Currently with the 20 Hz ns-laser takes about 3 h to treat an area of 1 cm × 1 cm. A considerable improvement could be a laser with a faster repetition rate that allows scaling up the scan velocity. Another limiting factor is the COST jet. The plasma power is restricted to approx. 1-3 W. An APPJ with a capillary as described by *Winzer et al.* [144] could considerably increase the plasma power to produce higher species densities. It can also be operated with a wider and more confined effluent, reducing the influence of ambient atmosphere on the treatment through reduced quenching of reactive species.

To optimize reactive species densities, a general understanding of the oxidation mechanisms of copper is needed. Here, a simulation of the copper oxide formation is required. It could help identify how deeply the oxides penetrate into the sample and predict the species ratio of atomic oxygen and molecular oxygen needed to facilitate the formation of specific oxide ratios.

The combination of laser and plasma can also be extended to other materials in catalysis, such as silver (Ag). It can also be used in the CO_2-RR to produce CO. Similar to copper, a change in surface structure and stoichiometry could improve the catalytic performance by producing AgO. The proximity to the copper case regarding the plasma species facilitates an easy transition. Another example is titanium. Titanium nitride (TiN) nanoparticles are of high interest in photocatalysis. The laser-plasma treatment is able to produce nanoparticles via PLIDS and could contribute to the nitridation of titanium through reactive nitrogen species produced by the COST jet. These examples should illustrate the system's potential flexibility.

Acknowledgments

Abschließend möchte ich allen Personen von Herzen danken, die mich in der Zeit als Doktorand und beim Verfassen meiner Dissertation begleitet und unterstützt haben:

- Prof. Dr. Judith Golda, für die Möglichkeit, meine Dissertation in ihrer Arbeitsgruppe *Plasma Interface Physics* durchführen zu können. Ich bedanke mich herzlichst für die tolle Betreuung und die unterstützenden Gespräche, die immer für ein sehr motivierendes Arbeitsumfeld gesorgt haben.
- Prof. Dr. Achim von Keudell, für die Übernahme des Zweitgutachtens meiner Dissertation, sowie seiner herausragenden Vorlesungen während meines Studiums.
- Dr. Marc Böke für seine Unterstützung und seine Anregungen während unserer wöchentlichen Meetings, sowie für die Korrektur dieser Arbeit.
- Dr. Marina Prenzel für ihre Expertise und Zusammenarbeit beim XPS und dass sie immer ein offenes Ohr für mich hatte.
- Lennart Kulik, Robin Minke und Jannis Kaufmann, die ich in ihren Bachelor bzw. Master Abschlussarbeiten begleiten durfte. Es war mir eine große Freude mit euch im Labor zusammen zu arbeiten und ich hoffe ihr habt in dieser Zeit genauso viel lernen können wie ich.
- Meinen Freunden David Steuer, Alexander Schicke, Steffen Schüttler und Henrik van Impel, mit denen ich so einige unvergessliche Momente teilen durfte. Ich danke euch für die gemeinsame Zeit und hoffe, dass wir unsere Freundschaft auch über die Zeit am Lehrstuhl hinaus erhalten werden.
- Meiner Büronachbarin Pia, für die immer freundliche Arbeitsatmosphäre.
- Allen Mitarbeitern des Lehrstuhls *Experimental Physik II* und der Arbeitsgruppe *Plasma Interface Physics*, für die herausragende Zusammenarbeit und Stimmung. Insbesondere Alicia Gonzales, für die Beratung in bürokratischen Angelegenheiten und das Ausbügeln so mancher Unachtsamkeiten meinerseits.
- Meiner Familie und meinen Freunden, für die Unterstützung während meines gesamten Studiums und darüber hinaus. Vielen Dank für die schöne gemeinsame Zeit und die benötigte Ablenkung an stressigen Tagen.
- Nadine Walle, für ihre Liebe und emotionale Unterstützung. Ich liebe dich sehr!

Bibliography

[1] G. Centi, E. A. Quadrelli, and S. Perathoner. “Catalysis for CO2 conversion: a key technology for rapid introduction of renewable energy in the value chain of chemical industries”. In: *Energy & Environmental Science* 6.6 (2013), p. 1711. ISSN: 1754-5692, 1754-5706. DOI: 10.1039/c3ee00056g.

[2] A. Bogaerts, X. Tu, J. C. Whitehead, et al. “The 2020 plasma catalysis roadmap”. In: *Journal of Physics D: Applied Physics* 53.44 (Oct. 28, 2020), p. 443001. ISSN: 0022-3727, 1361-6463. DOI: 10.1088/1361-6463/ab9048.

[3] S. Chu, Y. Cui, and N. Liu. “The path towards sustainable energy”. In: *Nature Materials* 16.1 (Jan. 2017), pp. 16–22. ISSN: 1476-1122, 1476-4660. DOI: 10.1038/nmat4834.

[4] W. Zhang, C. Huang, Q. Xiao, et al. “Atypical Oxygen-Bearing Copper Boosts Ethylene Selectivity toward Electrocatalytic CO_2 Reduction”. In: *Journal of the American Chemical Society* 142.26 (July 1, 2020), pp. 11417–11427. ISSN: 0002-7863, 1520-5126. DOI: 10.1021/jacs.0c01562.

[5] Z. W. Seh, J. Kibsgaard, C. F. Dickens, et al. “Combining theory and experiment in electrocatalysis: Insights into materials design”. In: *Science* 355.6321 (Jan. 13, 2017), eaad4998. ISSN: 0036-8075, 1095-9203. DOI: 10.1126/science.aad4998.

[6] R. M. Arán-Ais, D. Gao, and B. Roldan Cuenya. “Structure- and Electrolyte-Sensitivity in CO_2 Electroreduction”. In: *Accounts of Chemical Research* 51.11 (Nov. 20, 2018), pp. 2906–2917. ISSN: 0001-4842, 1520-4898. DOI: 10.1021/acs.accounts.8b00360.

[7] Y. Hori, K. Kikuchi, and S. Suzuki. “Production of CO and CH4 in electrochemical reduction of CO2 at metal electrodes in aqueous hydrogencarbonate solution”. In: *Chemistry Letters* 14.11 (Nov. 5, 1985), pp. 1695–1698. ISSN: 0366-7022, 1348-0715. DOI: 10.1246/cl.1985.1695.

[8] M. Gattrell, N. Gupta, and A. Co. “A review of the aqueous electrochemical reduction of CO2 to hydrocarbons at copper”. In: *Journal of Electroanalytical Chemistry* 594.1 (Aug. 2006), pp. 1–19. ISSN: 15726657. DOI: 10.1016/j.jelechem.2006.05.013.

[9] D. Gao, R. M. Arán-Ais, H. S. Jeon, et al. “Rational catalyst and electrolyte design for CO2 electroreduction towards multicarbon products”. In: *Nature Catalysis* 2.3 (Mar. 4, 2019), pp. 198–210. ISSN: 2520-1158. DOI: 10.1038/s41929-019-0235-5.

[10] M. R. Singh, E. L. Clark, and A. T. Bell. “Thermodynamic and achievable efficiencies for solar-driven electrochemical reduction of carbon dioxide to transportation fuels”. In: *Proceedings of the National Academy of Sciences* 112.45 (Nov. 10, 2015). ISSN: 0027-8424, 1091-6490. DOI: 10.1073/pnas.1519212112.

[11] P. De Luna, R. Quintero-Bermudez, C.-T. Dinh, et al. “Catalyst electro-redeposition controls morphology and oxidation state for selective carbon dioxide reduction”. In: *Nature Catalysis* 1.2 (Jan. 15, 2018), pp. 103–110. ISSN: 2520-1158. DOI: 10.1038/s41929-017-0018-9.

[12] X. Lu, M. Laroussi, and V. Puech. “On atmospheric-pressure non-equilibrium plasma jets and plasma bullets”. In: *Plasma Sources Science and Technology* 21.3 (June 1, 2012), p. 034005. ISSN: 0963-0252, 1361-6595. DOI: 10.1088/0963-0252/21/3/034005.

[13] J. Winter, R. Brandenburg, and K.-D. Weltmann. “Atmospheric pressure plasma jets: an overview of devices and new directions”. In: *Plasma Sources Science and Technology* 24.6 (Oct. 8, 2015), p. 064001. ISSN: 0963-0252, 1361-6595. DOI: 10.1088/0963-0252/24/6/064001.

[14] E. Robert, V. Sarron, D. Riès, et al. “Characterization of pulsed atmospheric-pressure plasma streams (PAPS) generated by a plasma gun”. In: *Plasma Sources Science and Technology* 21.3 (June 1, 2012), p. 034017. ISSN: 0963-0252, 1361-6595. DOI: 10.1088/0963-0252/21/3/034017.

[15] A. Sobota, O. Guaitella, G. B. Sretenović, et al. “Electric field measurements in a kHz-driven He jet—the influence of the gas flow speed”. In: *Plasma Sources Science and Technology* 25.6 (Nov. 18, 2016), p. 065026. ISSN: 1361-6595. DOI: 10.1088/0963-0252/25/6/065026.

[16] J. Golda, J. Held, B. Redeker, et al. “Concepts and characteristics of the ‘COST Reference Microplasma Jet’”. In: *Journal of Physics D: Applied Physics* 49.8 (Mar. 2, 2016), p. 084003. ISSN: 0022-3727, 1361-6463. DOI: 10.1088/0022-3727/49/8/084003.

[17] S. Reuter, T. Von Woedtke, and K.-D. Weltmann. “The kINPen—a review on physics and chemistry of the atmospheric pressure plasma jet and its applications”. In: *Journal of Physics D: Applied Physics* 51.23 (June 13, 2018), p. 233001. ISSN: 0022-3727, 1361-6463. DOI: 10.1088/1361-6463/aab3ad.

[18] J. Waskoenig, K. Niemi, N. Knake, et al. “Atomic oxygen formation in a radio-frequency driven micro-atmospheric pressure plasma jet”. In: *Plasma Sources Science and Technology* 19.4 (Aug. 1, 2010), p. 045018. ISSN: 0963-0252, 1361-6595. DOI: 10.1088/0963-0252/19/4/045018.

[19] P. Preissing, I. Korolov, J. Schulze, et al. “Three-dimensional density distributions of NO in the effluent of the COST reference microplasma jet operated in He/N_2/O_2”. In: *Plasma Sources Science and Technology* 29.12 (Dec. 1, 2020), p. 125001. ISSN: 0963-0252, 1361-6595. DOI: 10.1088/1361-6595/abbd86.

[20] L. Bischoff, G. Hübner, I. Korolov, et al. “Experimental and computational investigations of electron dynamics in micro atmospheric pressure radio-frequency plasma jets operated in He/N_2 mixtures”. In: *Plasma Sources Science and Technology* 27.12 (Dec. 28, 2018), p. 125009. ISSN: 1361-6595. DOI: 10.1088/1361-6595/aaf35d.

[21] D. Maletić, N. Puač, S. Lazović, et al. “Detection of atomic oxygen and nitrogen created in a radio-frequency-driven micro-scale atmospheric pressure plasma jet using mass spectrometry”. In: *Plasma Physics and Controlled Fusion* 54.12 (Dec. 1, 2012), p. 124046. ISSN: 0741-3335, 1361-6587. DOI: 10.1088/0741-3335/54/12/124046.

[22] Y. Liu, I. Korolov, J. Trieschmann, et al. “Micro atmospheric pressure plasma jets excited in He/O_2 by voltage waveform tailoring: a study based on a numerical hybrid model and experiments”. In: *Plasma Sources Science and Technology* 30.6 (June 1, 2021), p. 064001. ISSN: 0963-0252, 1361-6595. DOI: 10.1088/1361-6595/abd0e0.

[23] I. Korolov, D. Steuer, L. Bischoff, et al. “Atomic oxygen generation in atmospheric pressure RF plasma jets driven by tailored voltage waveforms in mixtures of He and O_2”. In: *Journal of Physics D: Applied Physics* 54.12 (Mar. 25, 2021), p. 125203. ISSN: 0022-3727, 1361-6463. DOI: 10.1088/1361-6463/abd20e.

[24] J. Golda, J. Held, and V. S.-v. D. Gathen. "Comparison of electron heating and energy loss mechanisms in an RF plasma jet operated in argon and helium". In: *Plasma Sources Science and Technology* 29.2 (Feb. 14, 2020), p. 025014. ISSN: 1361-6595. DOI: 10.1088/1361-6595/ab6c81.

[25] M. Vass, D. Schulenberg, Z. Donkó, et al. "A new 2D fluid-MC hybrid approach for simulating nonequilibrium atmospheric pressure plasmas: density distribution of atomic oxygen in radio-frequency plasma jets in He/O $_2$ mixtures". In: *Plasma Sources Science and Technology* 33.1 (Jan. 1, 2024), p. 015012. ISSN: 0963-0252, 1361-6595. DOI: 10.1088/1361-6595/ad1f37.

[26] M. Klich, S. Wilczek, Z. Donkó, et al. "Simulation and modeling of radio-frequency atmospheric pressure plasmas in the non-neutral regime". In: *Plasma Sources Science and Technology* 31.4 (Apr. 1, 2022), p. 045003. ISSN: 0963-0252, 1361-6595. DOI: 10.1088/1361-6595/ac5cd3.

[27] Y. He, P. Preissing, D. Steuer, et al. "Zero-dimensional and pseudo-one-dimensional models of atmospheric-pressure plasma jets in binary and ternary mixtures of oxygen and nitrogen with helium background". In: *Plasma Sources Science and Technology* 30.10 (Oct. 1, 2021), p. 105017. ISSN: 0963-0252, 1361-6595. DOI: 10.1088/1361-6595/ac278d.

[28] A. G. Gusakov, A. G. Voropayev, M. L. Zheludkevich, et al. "Studies of the interaction of copper with atomic and molecular oxygen". In: *Physical Chemistry Chemical Physics* 1.23 (Jan. 1, 1999), pp. 5311–5314. ISSN: 1463-9084. DOI: 10.1039/A905829J.

[29] D. Gao, I. Zegkinoglou, N. J. Divins, et al. "Plasma-Activated Copper Nanocube Catalysts for Efficient Carbon Dioxide Electroreduction to Hydrocarbons and Alcohols". In: *ACS Nano* 11.5 (May 23, 2017), pp. 4825–4831. ISSN: 1936-0851, 1936-086X. DOI: 10.1021/acsnano.7b01257.

[30] D. Gao, F. Scholten, and B. Roldan Cuenya. "Improved CO $_2$ Electroreduction Performance on Plasma-Activated Cu Catalysts via Electrolyte Design: Halide Effect". In: *ACS Catalysis* 7.8 (Aug. 4, 2017), pp. 5112–5120. ISSN: 2155-5435, 2155-5435. DOI: 10.1021/acscatal.7b01416.

[31] H. Mistry, A. S. Varela, C. S. Bonifacio, et al. "Highly selective plasma-activated copper catalysts for carbon dioxide reduction to ethylene". In: *Nature Communications* 7.1 (June 30, 2016), p. 12123. ISSN: 2041-1723. DOI: 10.1038/ncomms12123.

[32] J. P. Booth, A. Chatterjee, O. Guaitella, et al. "Quenching of O $_2$ (b ^{1}Sigma $_g$ $^+$) by O(^{3} P) atoms. Effect of gas temperature". In: *Plasma Sources Science and Technology* 31.6 (June 1, 2022), p. 065012. ISSN: 0963-0252, 1361-6595. DOI: 10.1088/1361-6595/ac7749.

[33] A. A. Ionin, I. V. Kochetov, A. P. Napartovich, et al. "Physics and engineering of singlet delta oxygen production in low-temperature plasma". In: *Journal of Physics D: Applied Physics* 40.2 (Jan. 21, 2007), R25–R61. ISSN: 0022-3727, 1361-6463. DOI: 10.1088/0022-3727/40/2/R01.

[34] J. S. Sousa, G. Bauville, B. Lacour, et al. "O 2 (a Delta 1 g) production at atmospheric pressure by microdischarge". In: *Applied Physics Letters* 93.1 (July 7, 2008), p. 011502. ISSN: 0003-6951, 1077-3118. DOI: 10.1063/1.2957032.

[35] J. S. Sousa, K. Niemi, L. J. Cox, et al. "Cold atmospheric pressure plasma jets as sources of singlet delta oxygen for biomedical applications". In: *Journal of Applied Physics* 109.12 (June 15, 2011), p. 123302. ISSN: 0021-8979, 1089-7550. DOI: 10.1063/1.3601347.

[36] C. S. Le Duff, M. J. Lawrence, and P. Rodriguez. “Role of the Adsorbed Oxygen Species in the Selective Electrochemical Reduction of CO_2 to Alcohols and Carbonyls on Copper Electrodes”. In: *Angewandte Chemie* 129.42 (Oct. 9, 2017), pp. 13099–13104. ISSN: 00448249. DOI: 10.1002/ange.201706463.

[37] Y. Zhou, F. Che, M. Liu, et al. “Dopant-induced electron localization drives CO2 reduction to C2 hydrocarbons”. In: *Nature Chemistry* 10.9 (Sept. 2018), pp. 974–980. ISSN: 1755-4330, 1755-4349. DOI: 10.1038/s41557-018-0092-x.

[38] A. Eilert, F. Cavalca, F. S. Roberts, et al. “Subsurface Oxygen in Oxide-Derived Copper Electrocatalysts for Carbon Dioxide Reduction”. In: *The Journal of Physical Chemistry Letters* 8.1 (Jan. 5, 2017), pp. 285–290. ISSN: 1948-7185, 1948-7185. DOI: 10.1021/acs.jpclett.6b02273.

[39] A. D. Handoko, C. W. Ong, Y. Huang, et al. “Mechanistic Insights into the Selective Electroreduction of Carbon Dioxide to Ethylene on Cu_2O-Derived Copper Catalysts”. In: *The Journal of Physical Chemistry C* 120.36 (Sept. 15, 2016), pp. 20058–20067. ISSN: 1932-7447, 1932-7455. DOI: 10.1021/acs.jpcc.6b07128.

[40] D. Ren, Y. Deng, A. D. Handoko, et al. “Selective Electrochemical Reduction of Carbon Dioxide to Ethylene and Ethanol on Copper(I) Oxide Catalysts”. In: *ACS Catalysis* 5.5 (May 1, 2015), pp. 2814–2821. ISSN: 2155-5435, 2155-5435. DOI: 10.1021/cs502128q.

[41] W. Zhang, Y. Hu, L. Ma, et al. “Progress and Perspective of Electrocatalytic CO_2 Reduction for Renewable Carbonaceous Fuels and Chemicals”. In: *Advanced Science* 5.1 (Jan. 2018), p. 1700275. ISSN: 21983844. DOI: 10.1002/advs.201700275.

[42] S. Y. Lee, H. Jung, N.-K. Kim, et al. “Mixed Copper States in Anodized Cu Electrocatalyst for Stable and Selective Ethylene Production from CO_2 Reduction”. In: *Journal of the American Chemical Society* 140.28 (July 18, 2018), pp. 8681–8689. ISSN: 0002-7863, 1520-5126. DOI: 10.1021/jacs.8b02173.

[43] H. Jung, S. Y. Lee, C. W. Lee, et al. “Electrochemical Fragmentation of Cu_2O Nanoparticles Enhancing Selective C–C Coupling from CO_2 Reduction Reaction”. In: *Journal of the American Chemical Society* 141.11 (Mar. 20, 2019), pp. 4624–4633. ISSN: 0002-7863, 1520-5126. DOI: 10.1021/jacs.8b11237.

[44] R. Reske, H. Mistry, F. Behafarid, et al. “Particle Size Effects in the Catalytic Electroreduction of CO_2 on Cu Nanoparticles”. In: *Journal of the American Chemical Society* 136.19 (May 14, 2014), pp. 6978–6986. ISSN: 0002-7863, 1520-5126. DOI: 10.1021/ja500328k.

[45] O. A. Baturina, Q. Lu, M. A. Padilla, et al. “CO_2 Electroreduction to Hydrocarbons on Carbon-Supported Cu Nanoparticles”. In: *ACS Catalysis* 4.10 (Oct. 3, 2014), pp. 3682–3695. ISSN: 2155-5435, 2155-5435. DOI: 10.1021/cs500537y.

[46] Y.-X. Duan, F.-L. Meng, K.-H. Liu, et al. “Amorphizing of Cu Nanoparticles toward Highly Efficient and Robust Electrocatalyst for CO_2 Reduction to Liquid Fuels with High Faradaic Efficiencies”. In: *Advanced Materials* 30.14 (Apr. 2018), p. 1706194. ISSN: 09359648. DOI: 10.1002/adma.201706194.

[47] J. E. Sipe, J. F. Young, J. S. Preston, et al. “Laser-induced periodic surface structure. I. Theory”. In: *Physical Review B* 27.2 (Jan. 15, 1983), pp. 1141–1154. ISSN: 0163-1829. DOI: 10.1103/PhysRevB.27.1141.

[48] J. Trice, D. Thomas, C. Favazza, et al. “Pulsed-laser-induced dewetting in nanoscopic metal films: Theory and experiments”. In: *Physical Review B* 75.23 (June 22, 2007), p. 235439. DOI: 10.1103/PhysRevB.75.235439.

[49] C. Favazza, R. Kalyanaraman, and R. Sureshkumar. “Robust nanopatterning by laser-induced dewetting of metal nanofilms”. In: *Nanotechnology* 17.16 (Aug. 28, 2006), pp. 4229–4234. ISSN: 0957-4484, 1361-6528. DOI: 10.1088/0957-4484/17/16/038.

[50] Y. Wu, J. D. Fowlkes, P. D. Rack, et al. “On the Breakup of Patterned Nanoscale Copper Rings into Droplets via Pulsed-Laser-Induced Dewetting: Competing Liquid-Phase Instability and Transport Mechanisms”. In: *Langmuir* 26.14 (July 20, 2010), pp. 11972–11979. ISSN: 0743-7463, 1520-5827. DOI: 10.1021/la1013818.

[51] J. D. Fowlkes, L. Kondic, J. Diez, et al. “Self-Assembly versus Directed Assembly of Nanoparticles via Pulsed Laser Induced Dewetting of Patterned Metal Films”. In: *Nano Letters* 11.6 (June 8, 2011), pp. 2478–2485. ISSN: 1530-6984, 1530-6992. DOI: 10.1021/nl200921c.

[52] W. J. Durand, A. A. Peterson, F. Studt, et al. “Structure effects on the energetics of the electrochemical reduction of CO2 by copper surfaces”. In: *Surface Science* 605.15 (Aug. 2011), pp. 1354–1359. ISSN: 00396028. DOI: 10.1016/j.susc.2011.04.028.

[53] J. Golda, J. Held, B. Redeker, et al. “Concepts and characteristics of the ’COST Reference Microplasma Jet’”. In: *Journal of Physics D* 49 (2016), p. 084003.

[54] D. Steuer, I. Korolov, S. Chur, et al. “2D spatially resolved O atom density profiles in an atmospheric pressure plasma jet: from the active plasma volume to the effluent”. In: *Journal of Physics D: Applied Physics* 54.35 (Sept. 2, 2021), p. 355204. ISSN: 0022-3727, 1361-6463. DOI: 10.1088/1361-6463/ac09b9.

[55] S. Chur, L. Kulik, V. Schulz-von Der Gathen, et al. “Self-Organizing Sub-um Surface Structures Stimulated by Microplasma Generated Reactive Species and Short-Pulsed Laser Irradiation”. In: *ACS Omega* 9.27 (July 9, 2024), pp. 29234–29243. ISSN: 2470-1343, 2470-1343. DOI: 10.1021/acsomega.3c10033.

[56] J. Pawlat, P. Terebun, M. Kwiatkowski, et al. “RF atmospheric plasma jet surface treatment of paper”. In: *Journal of Physics D: Applied Physics* 49.37 (Sept. 21, 2016), p. 374001. ISSN: 0022-3727, 1361-6463. DOI: 10.1088/0022-3727/49/37/374001.

[57] D. Shaw, A. West, J. Bredin, et al. “Mechanisms behind surface modification of polypropylene film using an atmospheric-pressure plasma jet”. In: *Plasma Sources Science and Technology* 25.6 (Oct. 27, 2016), p. 065018. ISSN: 1361-6595. DOI: 10.1088/0963-0252/25/6/065018.

[58] T. Ichiki, R. Taura, and Y. Horiike. “Localized and ultrahigh-rate etching of silicon wafers using atmospheric-pressure microplasma jets”. In: *Journal of Applied Physics* 95.1 (Jan. 1, 2004), pp. 35–39. ISSN: 0021-8979, 1089-7550. DOI: 10.1063/1.1630375.

[59] J. Benedikt, V. Raballand, A. Yanguas-Gil, et al. “Thin film deposition by means of atmospheric pressure microplasma jet”. In: *Plasma Physics and Controlled Fusion* 49.12 (Dec. 1, 2007), B419–B427. ISSN: 0741-3335, 1361-6587. DOI: 10.1088/0741-3335/49/12B/S39.

[60] A. J. L. Michael A. Liebermann. *Principles of Plasma Discharges and Materials Processing*. 2nd. WILEY, 2005. ISBN: 978-0-471-72001-0.

[61] P. Fauchais and A. Vardelle. “Thermal plasmas”. In: *IEEE Transactions on Plasma Science* 25.6 (Dec. 1997), pp. 1258–1280. ISSN: 1939-9375. DOI: 10.1109/27.650901.

[62] O. V. Penkov. “A review of recent applications of atmospheric pressure plasma jets for materials processing”. In: *Journal of Coatings Technology and Research* 12 (2015). ISSN: 1547-0091.

[63] D. Graves. “Low temperature plasma biomedicine: A tutorial review)”. In: *Physics of Plasmas* 21 (2014), p. 080901.

[64] K.-D. Weltmann and T. Woedtke. “Plasma medicine - Current state of research and medical application”. In: *Plasma Physics and Controlled Fusion* 59 (Jan. 2017), p. 014031. DOI: 10.1088/0741-3335/59/1/014031.

[65] N. Bibinov, N. Knake, H. Bahre, et al. “Spectroscopic characterization of an atmospheric pressure μ-jet plasma source”. In: *Journal of Physics D: Applied Physics* 44.34 (Aug. 31, 2011), p. 345204. ISSN: 0022-3727, 1361-6463. DOI: 10.1088/0022-3727/44/34/345204.

[66] P. Viegas, E. Slikboer, Z. Bonaventura, et al. “Physics of plasma jets and interaction with surfaces: review on modelling and experiments”. In: *Plasma Sources Science and Technology* 31.5 (May 1, 2022), p. 053001. ISSN: 0963-0252, 1361-6595. DOI: 10.1088/1361-6595/ac61a9.

[67] S. Kelly, J. Golda, M. M. Turner, et al. “Gas and heat dynamics of a micro-scaled atmospheric pressure plasma reference jet”. In: *Journal of Physics D: Applied Physics* 48.44 (Nov. 11, 2015), p. 444002. ISSN: 0022-3727, 1361-6463. DOI: 10.1088/0022-3727/48/44/444002.

[68] K. H. Becker, J. G. Eden, and K. H. Schoenbach. “Cluster Issue on Microplasmas”. In: *Journal of Physics D: Applied Physics* 38.11 (June 7, 2005). ISSN: 0022-3727, 1361-6463. DOI: 10.1088/0022-3727/38/11/E01.

[69] V. S.-v. d. G. A. von Keudell. “Konditionierung von metallischen Schichten durch Laser- und Plasmawechselwirkung”. lecturescript. Ruhr-Universität Bochum, Universitätsbibliothek, 2022.

[70] J. M. Meek. “A Theory of Spark Discharge”. In: *Phys. Rev.* 57 (Apr. 1940), p. 722.

[71] E. Marode. “The mechanism of spark breakdown in air at atmospheric pressure between a positive point and a plane. I. Experimental: Nature of the streamer track”. In: *Journal of Applied Physics* 46 (1975), pp. 2005–2015.

[72] T. Hemke, A. Wollny, M. Gebhardt, et al. “Spatially resolved simulation of a radio-frequency driven micro-atmospheric pressure plasma jet and its effluent”. In: *Journal of Physics D* 44 (2011), p. 285206.

[73] F. Paschen. “Ueber die zum Funkenübergang in Luft, Wasserstoff und Kohlensäure bei verschiedenen Drucken erforderliche Potentialdifferenz”. In: *Annalen der Physik* 273 (), pp. 69–96.

[74] J. Townsend. *Electricity in gases.*

[75] W. Demtröder. *Experimentalphysik 3: Atome, Moleküle und Festkörper.* Springer, 2016.

[76] B. Hampel. *Absorptionsspektroskopie im Ultravioletten und sichtbaren Spektralbereich.* Vieweg+Teubner Verlag Wiesbaden, 1962.

[77] J. Waskoenig, K. Niemi, N. Knake, et al. “Atomic oxygen formation in a radio-frequency driven micro-atmospheric pressure plasma jet”. English. In: *Plasma sources science & technology* 19.4 (Aug. 2010). ISSN: 0963-0252. DOI: 10.1088/0963-0252/19/4/045018.

[78] G. Park, H. Lee, G. Kim, et al. “Global Model of He/O2 and Ar/O2 Atmospheric Pressure Glow Discharges”. In: *Plasma Processes and Polymers* 5.6 (2008), pp. 569–576. DOI: https://doi.org/10.1002/ppap.200800019.

[79] J. Y. Jeong, J. Park, I. Henins, et al. "Reaction Chemistry in the Afterglow of an Oxygen-Helium, Atmospheric-Pressure Plasma". In: *The Journal of Physical Chemistry A* 104.34 (2000), pp. 8027–8032. DOI: 10.1021/jp0012449.

[80] D. Steuer. "Vergleichende Untersuchung von zweidimensionalen Sauerstoffverteilungen in Mikroplasmen mit optischen Methoden". masterthesis. Ruhr-Universität Bochum, Universitätsbibliothek, 2020.

[81] K. Schofield. "Evaluated Chemical Kinetic Rate Constants for Various Gas Phase Reactions". In: *Journal of Physical and Chemical Reference Data* 2.1 (Jan. 1, 1973), pp. 25–84. ISSN: 0047-2689, 1529-7845. DOI: 10.1063/1.3253112.

[82] F. Kaufman and F. Del Greco. "Fast reactions of OH radicals". In: *Symposium (International) on Combustion* 9.1 (Jan. 1963), pp. 659–668. ISSN: 00820784. DOI: 10.1016/S0082-0784(63)80074-0.

[83] W. Koechner. *Solid-state laser engineering*. Sixth revised and updated edition. Springer series in optical sciences 1. New York, NY: Springer, 2006. 747 pp. ISBN: 9781441921178 9780387290942.

[84] R. Paschotta. "Flat-top Beams - an encyclopedia article". In: *RP Photonics Encyclopedia*. RP Photonics AG, 2011. DOI: 10.61835/6ku.

[85] S. S. Harilal, J. R. Freeman, P. K. Diwakar, et al. "Femtosecond Laser Ablation: Fundamentals and Applications". In: *Laser-Induced Breakdown Spectroscopy: Theory and Applications*. Ed. by S. Musazzi and U. Perini. Berlin, Heidelberg: Springer, 2014, pp. 143–166. ISBN: 9783642450853. DOI: 10.1007/978-3-642-45085-3_6.

[86] M. V. Shugaev, C. Wu, O. Armbruster, et al. "Fundamentals of ultrafast laser–material interaction". In: *MRS Bulletin* 41.12 (Dec. 2016), pp. 960–968. ISSN: 0883-7694, 1938-1425. DOI: 10.1557/mrs.2016.274.

[87] K. Jakubczak, ed. *Lasers: Applications in Science and Industry*. IntechOpen, 2011. 1 p. ISBN: 9789533077550 9789535149309.

[88] J. Bonse, M. Munz, and H. Sturm. "Structure formation on the surface of indium phosphide irradiated by femtosecond laser pulses". In: *Journal of Applied Physics* 97.1 (Jan. 1, 2005), p. 013538. ISSN: 0021-8979, 1089-7550. DOI: 10.1063/1.1827919.

[89] J. Bonse, S. Hohm, S. V. Kirner, et al. "Laser-Induced Periodic Surface Structures— A Scientific Evergreen". In: *IEEE Journal of Selected Topics in Quantum Electronics* 23.3 (May 2017), p. 7581030. ISSN: 1077-260X, 1558-4542. DOI: 10.1109/JSTQE.2016.2614183.

[90] S. Höhm. "Dynamik der Erzeugung und Mechanismen der Entstehung von periodischen Oberflächenstrukturen im Nanometerbereich (LIPSS) durch die Bestrahlung von Festkörpern mit Femtosekunden-Laserpulsen". In: (Dec. 8, 2014).

[91] R. Labenski. "Konditionierung von metallischen Schichten durch Laser- und Plasmawechselwirkung". bachelorthesis. Ruhr-Universität Bochum, Universitätsbibliothek, 2021.

[92] W. Zhou, R. Apkarian, Z. L. Wang, et al. "Fundamentals of Scanning Electron Microscopy (SEM)". In: *Scanning Microscopy for Nanotechnology: Techniques and Applications*. Ed. by W. Zhou and Z. L. Wang. New York, NY: Springer New York, 2007, pp. 1–40. ISBN: 978-0-387-39620-0. DOI: 10.1007/978-0-387-39620-0_1.

[93] M. Prenzel. "Control of aluminium oxide deposition by variable biasing". doctoralthesis. Ruhr-Universität Bochum, Universitätsbibliothek, 2013.

[94] T. L. Barr. *Modern ESCA: The Principles and Practice of X-Ray Photoelectron Spectroscopy*. 1st ed. CRC Press, Nov. 25, 2020. ISBN: 9781003069041. DOI: 10.1201/9781003069041.

[95] D. R. Baer and A. G. Shard. "Role of consistent terminology in XPS reproducibility". In: *Journal of Vacuum Science & Technology A* 38.3 (May 1, 2020), p. 031203. ISSN: 0734-2101, 1520-8559. DOI: 10.1116/6.0000016.

[96] M. C. Biesinger. "Advanced analysis of copper X-ray photoelectron spectra: Advanced analysis of copper X-ray photoelectron spectra". In: *Surface and Interface Analysis* 49.13 (Dec. 2017), pp. 1325–1334. ISSN: 01422421. DOI: 10.1002/sia.6239.

[97] S. Thomas, P. M. A. Sherwood, N. Singh, et al. "Superconductivity and electronic structure of Bi-based compounds". In: *Physical Review B* 39.10 (Apr. 1, 1989), pp. 6640–6651. ISSN: 0163-1829. DOI: 10.1103/PhysRevB.39.6640.

[98] M. P. Seah and W. A. Dench. "Quantitative electron spectroscopy of surfaces: A standard data base for electron inelastic mean free paths in solids". In: *Surface and Interface Analysis* 1.1 (Feb. 1979), pp. 2–11. ISSN: 0142-2421, 1096-9918. DOI: 10.1002/sia.740010103.

[99] J. Held. *mimurrayy/COST-power-monitor: v1.2.1*. Apr. 10, 2023. DOI: 10.5281/ZENODO.7812494.

[100] B. Niermann, M. Böke, N. Sadeghi, et al. "Space resolved density measurements of argon and helium metastable atoms in radio-frequency generated He-Ar micro-plasmas". In: *The European Physical Journal D* 60.3 (Dec. 1, 2010), pp. 489–495. ISSN: 1434-6079. DOI: 10.1140/epjd/e2010-00166-8.

[101] V. Schulz-von Der Gathen, V. Buck, T. Gans, et al. "Optical Diagnostics of Micro Discharge Jets". In: *Contributions to Plasma Physics* 47.7 (Nov. 2007), pp. 510–519. ISSN: 0863-1042, 1521-3986. DOI: 10.1002/ctpp.200710066.

[102] J. Winter, M. Dünnbier, A. Schmidt-Bleker, et al. "Aspects of UV-absorption spectroscopy on ozone in effluents of plasma jets operated in air". In: *Journal of Physics D: Applied Physics* 45.38 (Sept. 26, 2012), p. 385201. ISSN: 0022-3727, 1361-6463. DOI: 10.1088/0022-3727/45/38/385201.

[103] E. C. Y. Inn and Y. Tanaka. "Absorption Coefficient of Ozone in the Ultraviolet and Visible Regions". In: *Journal of the Optical Society of America* 43.10 (Oct. 1, 1953), p. 870. ISSN: 0030-3941. DOI: 10.1364/JOSA.43.000870.

[104] Y. Inoue and R. Ono. "Measurement of singlet delta oxygen in an atmospheric-pressure helium–oxygen plasma jet". In: *Journal of Physics D: Applied Physics* 50.21 (June 1, 2017), p. 214001. ISSN: 0022-3727, 1361-6463. DOI: 10.1088/1361-6463/aa6c53.

[105] D. S. Stafford and M. J. Kushner. "O 2 (Delta 1) production in He/O2 mixtures in flowing low pressure plasmas". In: *Journal of Applied Physics* 96.5 (Sept. 1, 2004), pp. 2451–2465. ISSN: 0021-8979, 1089-7550. DOI: 10.1063/1.1768615.

[106] C. Maszl, W. Breilmann, J. Benedikt, et al. "Origin of the energetic ions at the substrate generated during high power pulsed magnetron sputtering of titanium". In: *Journal of Physics D: Applied Physics* 47.22 (June 4, 2014), p. 224002. ISSN: 0022-3727, 1361-6463. DOI: 10.1088/0022-3727/47/22/224002.

[107] N. Brenning, C. Huo, D. Lundin, et al. "Understanding deposition rate loss in high power impulse magnetron sputtering: I. Ionization-driven electric fields". In: *Plasma Sources Sci-*

ence and Technology 21.2 (Apr. 1, 2012), p. 025005. ISSN: 0963-0252, 1361-6595. DOI: 10.1088/0963-0252/21/2/025005.

[108] D. Krüger, K. Köhn, S. Gallian, et al. "Reconstruction of the static magnetic field of a magnetron". In: *Physics of Plasmas* 25.6 (June 1, 2018), p. 061207. ISSN: 1070-664X, 1089-7674. DOI: 10.1063/1.5024983.

[109] J. Held. "Einf¨uhrung in die Plasmaphysik II: Niedertemperaturplasmen". doctoralthesis. Ruhr-Universität Bochum, Universitätsbibliothek, 2021.

[110] G. N. Raikar, J. C. Gregory, L. C. Christl, et al. "The interaction of atomic oxygen with copper: An XPS, AES, XRD, optical transmission, and stylus profilometry study". In: *NASA. Langley Research Center, LDEF: 69 Months in Space. Part 3: Second Post-Retrieval Symposium* (Apr. 1, 1993).

[111] S. Chur, R. Minke, Y. He, et al. "Dynamics of reactive oxygen species produced by the COST microplasma jet". In: *Plasma Sources Science and Technology* 34.10 (Oct. 1, 2025), p. 105014. ISSN: 0963-0252, 1361-6595. DOI: 10.1088/1361-6595/adfd7f.

[112] C. Lazzaroni, P. Chabert, M. A. Lieberman, et al. "Analytical–numerical global model of atmospheric-pressure radio-frequency capacitive discharges". In: *Plasma Sources Science and Technology* 21.3 (June 1, 2012), p. 035013. ISSN: 0963-0252, 1361-6595. DOI: 10.1088/0963-0252/21/3/035013.

[113] D. X. Liu, P. Bruggeman, F. Iza, et al. "Global model of low-temperature atmospheric-pressure He + H $_2$ O plasmas". In: *Plasma Sources Science and Technology* 19.2 (Apr. 1, 2010), p. 025018. ISSN: 0963-0252, 1361-6595. DOI: 10.1088/0963-0252/19/2/025018.

[114] S. Schröter, A. Wijaikhum, A. R. Gibson, et al. "Chemical kinetics in an atmospheric pressure helium plasma containing humidity". In: *Physical Chemistry Chemical Physics* 20.37 (2018), pp. 24263–24286. ISSN: 1463-9076, 1463-9084. DOI: 10.1039/C8CP02473A.

[115] S. Schröter, A. R. Gibson, M. J. Kushner, et al. "Numerical study of the influence of surface reaction probabilities on reactive species in an rf atmospheric pressure plasma containing humidity". In: *Plasma Physics and Controlled Fusion* 60.1 (Jan. 1, 2018), p. 014035. ISSN: 0741-3335, 1361-6587. DOI: 10.1088/1361-6587/aa8fe9.

[116] T. Murakami, K. Niemi, T. Gans, et al. "Afterglow chemistry of atmospheric-pressure helium–oxygen plasmas with humid air impurity". In: *Plasma Sources Science and Technology* 23.2 (Feb. 28, 2014), p. 025005. ISSN: 0963-0252, 1361-6595. DOI: 10.1088/0963-0252/23/2/025005.

[117] T. Murakami, K. Niemi, T. Gans, et al. "Interacting kinetics of neutral and ionic species in an atmospheric-pressure helium–oxygen plasma with humid air impurities". In: *Plasma Sources Science and Technology* 22.4 (June 26, 2013), p. 045010. ISSN: 0963-0252, 1361-6595. DOI: 10.1088/0963-0252/22/4/045010.

[118] T. Murakami, K. Niemi, T. Gans, et al. "Chemical kinetics and reactive species in atmospheric pressure helium–oxygen plasmas with humid-air impurities". In: *Plasma Sources Science and Technology* 22.1 (Dec. 11, 2012), p. 015003. ISSN: 0963-0252, 1361-6595. DOI: 10.1088/0963-0252/22/1/015003.

[119] B. Sun, D. Liu, F. Iza, et al. "Global model of an atmospheric-pressure capacitive discharge in helium with air impurities from 100 to 10 000 ppm". In: *Plasma Sources Science and Technology* 28.3 (Mar. 8, 2019), p. 035006. ISSN: 1361-6595. DOI: 10.1088/1361-6595/aaf8e1.

[120] W. V. Gaens and A. Bogaerts. “Kinetic modelling for an atmospheric pressure argon plasma jet in humid air”. In: *Journal of Physics D: Applied Physics* 46.27 (July 10, 2013), p. 275201. ISSN: 0022-3727, 1361-6463. DOI: 10.1088/0022-3727/46/27/275201.

[121] W. V. Gaens and A. Bogaerts. “Reaction pathways of biomedically active species in an Ar plasma jet”. In: *Plasma Sources Science and Technology* 23.3 (May 22, 2014), p. 035015. ISSN: 0963-0252, 1361-6595. DOI: 10.1088/0963-0252/23/3/035015.

[122] W. V. Gaens, P. J. Bruggeman, and A. Bogaerts. “Numerical analysis of the NO and O generation mechanism in a needle-type plasma jet”. In: *New Journal of Physics* 16.6 (June 24, 2014), p. 063054. ISSN: 1367-2630. DOI: 10.1088/1367-2630/16/6/063054.

[123] M. M. Turner. “Uncertainty and error in complex plasma chemistry models”. In: *Plasma Sources Science and Technology* 24.3 (June 8, 2015), p. 035027. ISSN: 0963-0252, 1361-6595. DOI: 10.1088/0963-0252/24/3/035027.

[124] D. Liu, B. Sun, F. Iza, et al. “Main species and chemical pathways in cold atmospheric-pressure Ar + H $_2$ O plasmas”. In: *Plasma Sources Science and Technology* 26.4 (Mar. 15, 2017), p. 045009. ISSN: 1361-6595. DOI: 10.1088/1361-6595/aa5c22.

[125] A. Schmidt-Bleker, J. Winter, A. Bösel, et al. “On the plasma chemistry of a cold atmospheric argon plasma jet with shielding gas device”. In: *Plasma Sources Science and Technology* 25.1 (Feb. 1, 2016), p. 015005. ISSN: 0963-0252, 1361-6595. DOI: 10.1088/0963-0252/25/1/015005.

[126] A. Schmidt-Bleker, J. Winter, S. Iseni, et al. “Reactive species output of a plasma jet with a shielding gas device—combination of FTIR absorption spectroscopy and gas phase modelling”. In: *Journal of Physics D: Applied Physics* 47.14 (Apr. 9, 2014), p. 145201. ISSN: 0022-3727, 1361-6463. DOI: 10.1088/0022-3727/47/14/145201.

[127] Y. He, R. P. Brinkmann, E. Kemaneci, et al. “Atomic oxygen densities in He/O_2 micro-scaled atmospheric pressure plasma jets: an systematic model validation study”. In: *Plasma Sources Science and Technology(to be submitted)* (2025).

[128] Y. He, P. Preissing, D. Steuer, et al. “Zero-dimensional and pseudo-one-dimensional models of atmospheric-pressure plasma jets in binary and ternary mixtures of oxygen and nitrogen with helium background”. In: *Plasma Sources Science and Technology* 30.10 (Oct. 2021), p. 105017. DOI: 10.1088/1361-6595/ac278d.

[129] P. J. Chantry. “A simple formula for diffusion calculations involving wall reflection and low density”. In: *Journal of Applied Physics* 62.4 (Aug. 1987), pp. 1141–1148. ISSN: 0021-8979. DOI: 10.1063/1.339662.

[130] A. Tejero-del-Caz, V. Guerra, D. Gonçalves, et al. “The LisbOn KInetics Boltzmann solver”. In: *Plasma Sources Science and Technology* 28.4 (Apr. 2019), p. 043001. DOI: 10.1088/1361-6595/ab0537.

[131] M. J. Kushner. “Modeling of microdischarge devices: Pyramidal structures”. In: *Journal of Applied Physics* 95.3 (Feb. 1, 2004), pp. 846–859. ISSN: 0021-8979, 1089-7550. DOI: 10.1063/1.1636251.

[132] M. J. Kushner. “Modelling of microdischarge devices: plasma and gas dynamics”. In: *Journal of Physics D: Applied Physics* 38.11 (June 7, 2005), pp. 1633–1643. ISSN: 0022-3727, 1361-6463. DOI: 10.1088/0022-3727/38/11/001.

[133] Y. Liu, M. Vass, G. Hübner, et al. “Local enhancement of electron heating and neutral species generation in radio-frequency micro-atmospheric pressure plasma jets: the effects of

structured electrode topologies". In: *Plasma Sources Science and Technology* 32.2 (Feb. 1, 2023), p. 025012. ISSN: 0963-0252, 1361-6595. DOI: 10.1088/1361-6595/acb9b8.

[134] A. Wijaikhum, D. Schröder, S. Schröter, et al. "Absolute ozone densities in a radio-frequency driven atmospheric pressure plasma using two-beam UV-LED absorption spectroscopy and numerical simulations". In: *Plasma Sources Science and Technology* 26.11 (Oct. 20, 2017), p. 115004. ISSN: 1361-6595. DOI: 10.1088/1361-6595/aa8ebb.

[135] S. Bang, R. Snoeckx, and M. S. Cha. "Temperature-Dependent Kinetics of Ozone Production in Oxygen Discharges". In: *Plasma Chemistry and Plasma Processing* 43.6 (Nov. 2023), pp. 1453–1472. ISSN: 0272-4324, 1572-8986. DOI: 10.1007/s11090-023-10370-7.

[136] B. Harris, J. P. Dedrick, K. Niemi, et al. "Ozone production by an He+O_2 radio-frequency atmospheric pressure plasma jet driven by tailored voltage waveforms". In: *Plasma Sources Science and Technology* 33.7 (July 1, 2024), p. 075020. ISSN: 0963-0252, 1361-6595. DOI: 10.1088/1361-6595/ad6587.

[137] M. C. Biesinger, L. W. Lau, A. R. Gerson, et al. "Resolving surface chemical states in XPS analysis of first row transition metals, oxides and hydroxides: Sc, Ti, V, Cu and Zn". In: *Applied Surface Science* 257.3 (Nov. 2010), pp. 887–898. ISSN: 01694332. DOI: 10.1016/j.apsusc.2010.07.086.

[138] X. Ribas and I. Güell. In: *Pure and Applied Chemistry* 86.3 (2014), pp. 345–360. DOI: doi:10.1515/pac-2013-1104.

[139] N. Fairley, V. Fernandez, M. Richard-Plouet, et al. "Systematic and collaborative approach to problem solving using X-ray photoelectron spectroscopy". In: *Applied Surface Science Advances* 5 (Sept. 2021), p. 100112. ISSN: 26665239. DOI: 10.1016/j.apsadv.2021.100112.

[140] J. P. Espinós, J. Morales, A. Barranco, et al. "Interface Effects for Cu, CuO, and Cu $_2$ O Deposited on SiO $_2$ and ZrO $_2$. XPS Determination of the Valence State of Copper in Cu/SiO $_2$ and Cu/ZrO $_2$ Catalysts". In: *The Journal of Physical Chemistry B* 106.27 (July 1, 2002), pp. 6921–6929. ISSN: 1520-6106, 1520-5207. DOI: 10.1021/jp014618m.

[141] C.-K. Wu, M. Yin, S. O'Brien, et al. "Quantitative Analysis of Copper Oxide Nanoparticle Composition and Structure by X-ray Photoelectron Spectroscopy". In: *Chemistry of Materials* 18.25 (Dec. 1, 2006), pp. 6054–6058. ISSN: 0897-4756, 1520-5002. DOI: 10.1021/cm061596d.

[142] P. Dominic, F. Bourquard, S. Reynaud, et al. "On the Insignificant Role of the Oxidation Process on Ultrafast High-Spatial-Frequency LIPSS Formation on Tungsten". In: *Nanomaterials* 11.5 (Apr. 22, 2021), p. 1069. ISSN: 2079-4991. DOI: 10.3390/nano11051069.

[143] A. V. Dostovalov, T. J.-Y. Derrien, S. A. Lizunov, et al. "LIPSS on thin metallic films: New insights from multiplicity of laser-excited electromagnetic modes and efficiency of metal oxidation". In: *Applied Surface Science* 491 (Oct. 2019), pp. 650–658. ISSN: 01694332. DOI: 10.1016/j.apsusc.2019.05.171.

[144] T. Winzer, D. Steuer, S. Schüttler, et al. "RF-driven atmospheric-pressure capillary plasma jet in a He/O2 gas mixture: Multi-diagnostic approach to energy transport". In: *Journal of Applied Physics* 132.18 (Nov. 2022), p. 183301. ISSN: 0021-8979. DOI: 10.1063/5.0110252.

Sascha Frederik Chur

PhD Candidate - Ruhr University Bochum

Curriculum Vitae

Name	**Sascha Frederik Chur**
Date of Birth	**19.09.1995**
Place of Birth	**Hattingen**, *Germany*

Education

2021–2025	**PhD. Student**, *Physics*, Ruhr University, Bochum
2017–2021	**Master of Science**, *Physics*, Ruhr University, Bochum
2014–2017	**Bachelor of Science**, *Physics*, Ruhr University, Bochum
2014	**Abitur**, Schiller Gymnasium, Witten
2006–2014	**Secondary School**, Schiller Gymnasium, Witten
2002–2006	**Primary School**, Buchholzer Schule, Witten

Employment

2021–2025	**Research Assistant**, Plasma Interface Physics, Ruhr University Bochum
2017–2021	**Student Assistant**, *Public Relations*, Research Department Plasmas with Complex Interactions, Ruhr-University Bochum

Research Stays and Conferences

2025	**International Symposium on Plasma Chemistry**, Mineapolis, USA, Oral Presentation
2024	**International Workshop on Microplasmas**, Orléan, France, Oral Presentation
2023	**International Symposium on Plasma Chemistry**, Kyoto, Japan, Poster Presentation
2022	**Spring Meeting German Physical Society**, Heidelberg, Germany, Poster Presentation
2021	**Annual Gaseous Electronics Conference**, Online, Oral Presentation

sascha.chur@rub.de • *0000-0001-6926-3747*